T-4372

ATOMIC-SCALE STRUCTURE OF THE TIN DX CENTER AND OTHER RELATED DEFECTS IN ALUMINUM GALLIUM ARSENIDE SEMICONDUCTORS USING MÖSSBAUER SPECTROSCOPY

by

Luigi A. Greco

T-4372

A thesis submitted to the Faculty and the Board of Trustees of the Colorado School of Mines in partial fulfillment of the requirements for the degree of Doctor of Philosophy (Materials Science).

Golden, Colorado

Date 3/30/94

Signed: _____
Luigi A. Greco

Approved: _____
Prof. Don L. Williamson
Thesis Advisor

Golden, Colorado

Date 30 March 1994

_____
Prof. David L. Olson
Department Head
Materials Science Program

ABSTRACT

The DX center in III-V alloys has limited the use of these materials for electronic devices since the defect acts as an electron trap. To be able to control or eliminate the DX center, its atomic scale structure should be understood. Mössbauer spectroscopy has proven to be a valuable technique in probing the atomic-scale structure of certain atomic species. The dopant studied here is ^{119}Sn.

The thermal diffusion of Sn in $Al_xGa_{1-x}As$ using different temperatures, times, sample geometries and As_4 overpressures in evacuated and sealed fused silica ampoules was studied by x-ray diffraction (XRD), secondary ion mass spectroscopy and electrochemical capacitance versus voltage measurements. The AlGaAs surfaces decomposed into various Sn, Si, Ga and As oxides when an As_4 overpressure was introduced during annealing. However, annealing under ambient As_4 and furnace cooling eliminated surface decomposition although the Sn diffusion depth was less than that for a 0.5 atm As_4 overpressure. SiO_x and Si_xN_y RF-sputtered thin film capping layers deposited on AlGaAs were studied by XRD and Auger electron spectroscopy. For the annealed SiO_x films the AlGaAs surface was preserved, independent of the cooling technique used. Mössbauer spectroscopy was conducted on ^{119m}Sn-implanted $Al_xGa_{1-x}As$ (x=0.22 and 0.25) used for the source experiments and ^{119}Sn-doped $Al_xGa_{1-x}As$ (x=0.15, N_{Sn}~$2x10^{18}$ cm^{-3}) for the absorber experiment. The source samples were capped with 120 nm of SiO_x to preserve

the surface during the systematic study of annealing temperature versus site occupation and electrical activation via Mössbauer spectroscopy at 76 K and 4 K in the dark and in the light [to observe persistent photoconductivity (PPC) due to the DX center]. For all of the annealing conditions used the x=0.22 sample showed little evidence of PPC possibly due to compensating defects and/or radiation-induced capture. After annealing the x=0.25 sample at 1000° C for 2 hours under a Ga+Al overpressure, evidence of PPC was found via Hall measurements but no effect was seen by Mössbauer suggesting radiation-induced capture and/or non-nearest-neighbor lattice relaxation. The Ga+Al overpressure also served to decrease the loss of Sn through the SiO_x film, possibly through the removal of Ga and Al vacancies. The x=0.15 absorber showed a persistent 15-18 % change in the electrical resistance (10% change in n) between the light and dark. However, the observation of this effect was not apparent, even assuming negative-U (2 electron) behavior, in the Mössbauer measurements. This was also consistent with EXAFS results. These studies do not support the broken-bond model of Chadi and Chang, which is considered to be a widely accepted atomic-scale model of the DX center. A defect complex consisting of a substitutional $Sn_{Ga(Al)}^{+}$ site, and a $[V_{III}^{-}Al_{As}^{-2}]$ complex, which localizes 3 electrons and may not be a nearest-neighbor to the donor, was chosen for the DX center in the x=0.15 sample which supports EXAFS, recent positron annihilation and these Mössbauer studies.

TABLE OF CONTENTS

Chapter Page

LIST OF FIGURES

Page

LIST OF TABLES

Page

ACKNOWLEDGMENTS

I would like to thank my advisor, Professor Don L. Williamson, for his guidance, insight, patience and support, which allowed this project to be possible. I have always been impressed by his thoroughness and high standards in experimental research and will strive to follow his example.

Jack Kintner's assistance and expertise in the machine work required for this project was invaluable and appreciated.

I thank Orhan Öztürk and Yan Chen for their assistance in the cryogenic aspect of my experiments, Scott Jones, Stephen Glick, Martin van den Boogaard, Brenda Jacobs and Rex Rideout for their friendship and stimulating conversations.

The Mössbauer samples provided by our collaborators, Pierre Gibart and Guido Langouche, are greatly appreciated.

The AES data provided by Amy Franz, SIMS data by Sally Asher, C-V data by Jerry Olson and assistance on the Hall measurements by Tim Gessert, all at NREL, is much appreciated.

I want to thank Professors John U. Trefny, Baki Yarar and Jerome G. Morse for their support of my previous research at CSM.

Finally, I cannot thank my parents, Francesco and Lidia, enough for all the love and support that they have given me throughout my graduate career far from home.

My learning experience at CSM was tremendous and I look forward to applying the knowledge that I have acquired in my future endeavors.

This research was funded by NSF under grant number DMR-8902512.

1. Introduction

1.1 Technological importance of $Al_xGa_{1-x}As$

In 1962 Hall et al have observed coherent infrared radiation (840 nm) from forward biased p-n GaAs junctions. It was the first report of direct conversion of electrical energy to coherent radiation achieved in a solid state device. It was also the first example of a laser involving transitions between energy bands rather than localized atomic levels. Later, Kressel et al (1969) have shown that Si compensated $Al_xGa_{1-x}As$ p-n junctions also exhibited radiative emissions. These examples of early studies on III-V compounds led to the large body of research on these high-speed and optoelectronic materials.

The III-V alloys, especially $Al_xGa_{1-x}As$, are unique in that their band gap can be adjusted by varying x (1.4 eV at x=0 and 2.2 eV at x=1) without any significant change in their lattice dimensions (a=5.6533+0.0078x Å). This characteristic allows alloys, of varying x, to be matched for heterostructures or layered structures, such as solar cells. Structures such as these are also important in the fabrication of solid state lasers with adjustable wavelengths. Other important high-speed devices which can be fabricated from these alloys are field effect transistors (FET), high electron mobility transistors (HEMT) and bipolar junction transistors. The band gap of AlGaAs is also larger than Si which makes it attractive for high temperature applications. The material parameters of $Al_xGa_{1-x}As$ have been documented in an excellent review article by Adachi (1985).

1.2 The DX Center Problem

The DX center, a deep-level defect which acts as an effective electron trap, has been a major obstacle to the implementation of III-V semiconducting alloys for device applications.

When the III-V alloys are doped n-type problems arise with the position of the donor level in the energy gap. In $Al_xGa_{1-x}As$ shallow donor states are present for $x<0.22$. For $x>0.22$ deep level states begin to appear. However, under heavy doping conditions DX centers can appear for $x<0.22$ (Theis et al 1988). These states are designated as DX centers where "D" stands for the donor impurity (typical n-type donor atoms are Se, Si, Sn, and Te), and "X" for an unknown defect such as an arsenic vacancy (Lang, Logan, and Jaros 1979).

A major feature of the DX center is persistent photoconductivity (PPC) which is exhibited for temperatures below 100 K. This effect is defined as an abrupt increase in conductivity due to photoexcitation of trapped electrons to the conduction band and remains in that condition even after the illumination source is removed, provided a low temperature is maintained. PPC was first observed by Craford et al (1968) in Te and S doped $GaAs_{1-x}P_x$. This effect was later observed in Te doped $Al_xGa_{1-x}As$ by Nelson (1977). In 1977 a large lattice relaxation model was proposed to explain the PPC effect via a configuration coordinate diagram (Lang and Logan 1977). This model is based on the idea that PPC is due to deep level defects in which their electronic and vibrational states are strongly coupled. This model is the basis for future DX center mechanism studies.

The question arises: what is the exact microscopic structure of the DX center? Having the answer to this could lead to the elimination or, at least, the control of the DX center in III-V alloys. An important model for the atomic scale structure of the DX center was proposed by Chadi and Chang (1988, 1989). Using ab initio pseudopotential calculations for Si and S induced DX centers in $Al_xGa_{1-x}As$, they have found that it is a strongly localized and negatively charged defect which behaves as a negative-U center (localizes 2 electrons in its ground state; designated as DX^-). Their model also predicts that the formation of the DX center is due to a large lattice distortion caused by the group III site being displaced from the substitutional position (excited state) to an interstitial position (the ground state broken-bond configuration). That is, a distortion of a group IV donor (on a group III site) along <111> or a distortion of the Ga (or Al) atom along <111> for a group VI (on a group IV site) donor (C_{3v} symmetry). The authors have indicated that a possible method of DX center suppression is to introduce donors into interstitial positions in the material which are unlikely to undergo similar structural transformations. This would require a modification of the group-IV and -VI substitutional impurity doping. They have proposed group-III and -V interstitial dopants such as Al, Ga, and B. Further theoretical studies have shown agreement to Chadi and Chang's findings (Zhang 1991, Chadi 1992, Saito et al 1992, Biernacki 1992). In addition to the theoretical support, a large body of experimental results has been found which supports the negative-U and/or large lattice relaxation model of the DX center in III-V alloys (Mooney et al 1988 and 1989, O'Reilly 1989, Dmochowski et al 1989, Katsumoto et al

1990, Fujisawa et al 1990, Gibart et al 1990, Northrop and Mooney 1991, Roach et al 1991, Wolk et al 1991, Williamson and Gibart 1991, Dobaczewski and Kaczor 1991a, 1991b, 1991c, Su and Farmer 1991, Wang et al 1991, Fockele et al 1991, Jantsch et al 1991, Sampaio et al 1991, Mosser at al 1991, Leszczński et al 1991, Kajikama 1991, von Bardeleben et al 1992, Dobaczewski et al 1992, Mori et al 1992, Peale et al 1992, Ghosh and Kumar 1992, Wang et al 1992).

Two other explanations of the DX center's behavior have been proposed: small lattice relaxation and a positive-U ground state (localization of one electron; designated as DX^{o}). A small lattice relaxation model had been proposed before Chadi and Chang (Hjalmarson and Drummond 1986). They found, via previous experimental observations of PPC in materials such as $Al_xGa_{1-x}As$:Te with x=0.3, that PPC is linked to the isolated donor (as the Chadi and Chang model) undergoing a small lattice relaxation due to weak electron-lattice coupling as determined by capture cross-section calculations. There has been experimental evidence which support either positive-U or small lattice relaxation of the DX center (Henning and Ansems 1987, Talwar et al 1987, Li and Yu 1987, Mizuta and Kitano 1988, Alaya et al 1989, Subramanian et al 1990). Other experiments show inconclusive evidence concerning the size of the lattice relaxation or the sign of the correlation energy (-U or +U) (Yu and Li 1988, Theis et al 1989, Mooney et al 1989, Brunkov et al 1990, Baraldi et al 1991a and 1991b, Leith et al 1992).

A few reported attempts have been made to passivate the DX center. These include exposing doped $Al_xGa_{1-x}As$ to a hydrogen plasma to form hydrogen complexes with the

donor defect (Nabity et al 1987, Mastefaoui et al 1988), a theoretical study of hydrogen passivation of DX centers using the ab initio pseudopotential method by Chang, Cheong and Park (1992), plasma doping of $Al_xGa_{1-x}As$:Si via MBE (Etienne and Theiry-Mieg 1988), selectively doped $Al_xGa_{1-x}As$/GaAs heterostructures with Se (Ishikawa et al 1988), and B incorporation into GaAs:Si (Li et al 1989). It should be noted that with the hydrogen passivation technique the shallow donors are also passivated hence lowering the overall carrier concentration but at the same time increasing the mobility (Mastefaoui et al 1988).

It is currently understood that the DX center in III-V alloys is an isolated defect (Group IV donors on -III site, Group-VI donors on -V site) due to the donor atom which undergoes a large lattice relaxation (considered as a large energy difference between the thermal and optical ionization energies) upon photoionization, from an interstitial site to a substitutional one. Upon ionization of the DX center 2 electrons are released to allow the defect to be a shallow donor (d^+) which is understood as negative-U behavior (Chadi and Chang). The DX^o defect (one electron excited) is understood to be a metastable defect (Ghosh and Kumar 1992, von Bardeleben et al 1992). Current research based on a collaboration with Prof. Tim Hayes (RPI), Prof. Don L. Williamson (CSM), and Pierre Gibart (CNRS) is in progress to study the DX center's structure via EXAFS (extended x-ray fine structure) at SLAC/SSRL (Stanford Linear Accelerator Laboratory/ Stanford Synchrotron Radiation Laboratory). The EXAFS data will prove to be valuable in determining the DX center's surroundings and any lattice relaxation associated with

photoionization (Hayes et al 1989). The EXAFS data will complement the Mössbauer data discussed in this thesis.

1.3 Objectives and thesis overview

The goal of this thesis is to provide insight into the electronic and geometrical structure of the Sn DX center in $Al_xGa_{1-x}As$. This information should allow a selection of the proper theoretical model from the ones proposed in the literature.

A study of the thermal diffusion properties of Sn in $Al_xGa_{1-x}As$ will provide information that has not yet been found in the literature (past thermal diffusion studies have been done almost exclusively on GaAs). Included in this study are the effects of sample preparation, arsenic overpressure, and capping layers on the thermal diffusion properties on Sn in $Al_xGa_{1-x}As$ under a closed environment. The use of depth profiling techniques, such as capacitance-versus-voltage (C-V), secondary ion mass spectroscopy (SIMS), and Auger electron spectroscopy (AES) provide information on the thermally diffused species in $Al_xGa_{1-x}As$ and are used to optimize the conditions for future diffusion dopings. Electrical measurement techniques, such as the Hall effect, are used to obtain values for the carrier concentration, mobility and, more importantly, extent of PPC in $Al_xGa_{1-x}As$:Sn which correlates to DX center concentration.

Using the optimized conditions from the diffusion of ^{nat}Sn (natural Sn) or ^{119}Sn in $Al_xGa_{1-x}As$, ^{119m}Sn doped $Al_xGa_{1-x}As$ is used to obtain Mössbauer spectra of the DX center. From the various parameters associated with these spectra, an atomic

configuration of the Sn DX center can be obtained and therefore confirm or rule out one or more of the various theoretical models in the literature and, if necessary, propose a new atomic model consistent with the Mössbauer data, EXAFS data and other experimental results found in the literature.

The structure of the thesis is as follows:

Chapter 2 will discuss theoretical and experimental investigations into the atomic-scale structure of the DX center.

Chapter 3 will detail previous Sn ion implantation and diffusion studies on GaAs followed by an outline of the experimental procedure used to investigate Sn diffusion doping of $Al_xGa_{1-x}As$. Results from Sn solid source and SiO_x and Si_xN_y capping layers are discussed.

Chapter 4 describes the procedure for obtaining absorber and source Mössbauer spectra followed by data analysis used to obtain the structure of the DX center. An atomic scale model for the DX center is proposed.

2. Atomic Scale Structure of the DX Center in III-V Alloys

Although measurements of the electronic and optical properties of the DX center provide evidence for its behavior, that is, positive or negative-U and lattice relaxation effects, knowledge of the atomic scale structure of the DX center is required in order to understand how these effects come about. Experiments which provide a direct probe into the DX center's atomic structure, as well as theoretical investigations, are described below.

2.1 Experimental

An early experiment conducted by Narayanamurti et al (1979) using ballistic phonons, with well defined direction and polarization, generated in bulk GaAs and propagating towards a 10 μm epitaxial layer of $Al_xGa_{1-x}As$ [grown by liquid phase epitaxy (LPE) with $0.3<x<0.5$] containing 10^{18} cm^{-3} Sn or Te donors, showed that the Sn had trigonal symmetry while Te showed orthorhombic. Assuming large lattice relaxation and DX centers in the ground state, the authors have found evidence for the Sn_{Ga} exhibiting a (111) axial distortion while Te_{As} a (110) distortion.

Yu et al (1991) have used particle-induced x-ray emission (PIXE) and Rutherford backscattering (RBS) to study the lattice locations of Te and Sn DX centers in the ground state. The samples used were metal-organic chemical vapor deposition (MOCVD) grown 10 μm $Al_{0.42}Ga_{0.58}As$:Te on semi-insulating GaAs and molecular beam epitaxy (MBE)

grown 3.5 μm $Al_{0.42}Ga_{0.58}$:Sn on n^+ GaAs. The donor concentration in the Te sample was $3.6x10^{18}$ cm^{-3} and the Sn one $6x10^{18}$ cm^{-3}. Te and Sn were found to reside on an As site and Ga(Al) site, respectively. The PIXE experiment ruled out any off-center lattice relaxation of Te and Sn larger than 0.14 Å (minimum detectable displacement of the impurities). Their profiling techniques were not able to detect any displacement of the host atoms. The authors have ruled out large lattice relaxation and felt it would be worthwhile to consider a small lattice relaxation model which does not involve a large off-center displacement of the dopant atom.

Laplace-transform DLTS has been used by Dobaczewski et al (1992) to study the electron emission from DX centers in $Al_xGa_{1-x}As$ doped with Si (MBE grown, 10^{16} cm^{-3}) and Te (LPE grown, $5x10^{16}$ cm^{-3}) with $0.25<x<0.76$. They have shown that a substitutional-interstitial atom motion is responsible for DX behavior and any metastability effects. This motion was due to the $Si_{Ga(Al)}$ itself for the Si doped material and a Ga or Al motion for the Te_{As} doped one and has been attributed to ionization of the DX center. The authors have categorized this effect as a large lattice relaxation.

Several extended x-ray absorption fine structure (EXAFS) experiments have been conducted on $Al_xGa_{1-x}As$ to observe the environment surrounding the dopant atom. Kitano and Mizuta (1987 and 1988) have used this technique on 1.5 μm $Al_{0.38}Ga_{0.62}As$:Se (MOCVD grown on GaAs (001), 10^{19} cm^{-3} donors). They have observed very little change (<0.04 Å) in the position of the Se atoms, with respect to its nearest neighbors, between the ground state and the photo-ionized state. The authors

have concluded that the Se atom undergoes a small lattice relaxation. Rowe et al (1989) have studied the local structure of S in $Al_xGa_{1-x}AS$ (x=0.35,0.45) grown by LPE and MBE on semi-insulating GaAs. The dopant atoms were implanted at 100 keV and then annealed at 900°C under a flowing AsH_3 ambient. The carrier concentration was $5x10^{18}$ cm^{-3} while the local dopant concentration was 10^{19}-10^{20} cm^{-3}. The structural data were compared with identically prepared GaAs. EXAFS analysis showed that the first nearest neighbor for S is Al. A strong relaxation was observed for the S-Al bond (2.27±0.02 Å) compared to the bulk material first nearest neighbor distance (2.45 Å). Also, S appeared to be close to a substitutional site. Two of these distinct sites were proposed in GaAs:S (DX centers in GaAs are resonant with the conduction band, but can be made to appear in the gap when subjected to hydrostatic pressure) which were S_{As} (a shallow donor) and a complex formed by S_{As} with a V_{As} as a second nearest neighbor (shallow or deep acceptor). Hayes et al (1989) have conducted EXAFS experiments on GaAs:Sn and $Al_{0.3}Ga_{0.7}As$:Sn (Sn concentration=$5x10^{18}$ cm^{-3}). Measurements were conducted at 80 K in the dark in order to populate the DX center. The results have been compared with ordered $ZnSnAs_2$, where each Sn atom is surrounded by four As atoms at 2.60 Å. They have concluded that Sn has four nearest As neighbors at ≈2.58 Å. No evidence of large lattice relaxation associated with the DX center in the x=0.3 sample was found. Pant et al (1993) have performed EXAFS on $Al_xGa_{1-x}As$:Sn (x=0.11 and 0.23) and have observed that, for the x=0.11 sample, the three prominent structural peaks correspond to the neighbors of a substitutional Sn donor in a shallow donor site (2.27, 3.75 and 4.47 Å).

However, EXAFS measurements on this same sample one year later (Pant et al 1993) shows that a new structural peak has arisen at 2.81Å and that the peaks at 3.75 and 4.47 are altered (meaning that the Sn environment has changed during this time period) to positions corresponding to Sn in non-substitutional states. The x=0.23 sample is similar to x=0.11 after one year. The authors have speculated that oxidation has changed the Sn environment, accelerated by the grinding of the sample to a fine powder in order to avoid Bragg diffraction features in the data. A gimbal-mounted sample holder used to oscillate the sample was designed in order to suppress the Bragg contribution when using single crystals. Preliminary results on a single crystal sample of Sn-doped AlGaAs (x=0.23) showed that a near-neighbor lattice relaxation was not evident upon illumination.

Cargill et al (1992) have investigated the lattice strain caused by electron emission from the DX center using x-ray diffraction for Si- and Sn-doped $Al_xGa_{1-x}As$ with x=0.22 to 0.24. The AlGaAs was grown by MOCVD on (100) GaAs. Sn and Si concentration were determined by SIMS and carrier concentration by C-V. The impurity concentration ($7x10^{18}$ cm^{-3}) was larger than the carrier concentration ($5x10^{17}$ cm^{-3}) which is evidence of self-compensation. X-ray diffraction measurements were conducted at 14 K in the dark and light. The authors were concerned about DX center ionization by the x-rays. They believe that direct photoionization of the DX levels is a rare event but mainly caused by secondary electrons generated in the sample by non-radiative decay of x-ray induced excitations. The initial rate of decrease of the sample resistivity caused by the x-ray exposure (Cu Kα, 1.5405 Å) was 20% / hour, in order to limit x-ray ionization for the

cooled-in-the-dark samples, the total x-ray exposures were limited to less than 10 minutes so that x-ray ionization of the DX centers was less than 4 %. X-ray diffraction peak positions were measured with respect to the GaAs substrate peaks. Upon IR illumination the AlGaAs peaks shifted to smaller angles by an amount of the order of 10^{-4} degree. The isotropic strain (determined from the elastic constants and the d-spacing ratio of the (400) peak, $\Delta d_{400}/d_{400}$) was on the order of $\Delta a/a=10^{-5}$ (a=lattice constant). The authors stated two possible contributions to the observed lattice strain: 1) strain from filling of the conduction band states which is related to the conduction band deformation potential $a_e=dE_c/d(\ln V)$ and the bulk modulus B for AlGaAs, $[\Delta a/a]_e=-a_e\Delta N_e/3B$ where ΔN_e is the change in the carrier concentration between dark and light; 2) lattice strain caused by local bonding changes that may occur when DX centers are emptied which is denoted as $[\Delta a/a]_{DX}$. Adopting the Chadi-Chang model the authors have found $[\Delta a/a]_{DX} \sim 10^{-6}$, $[\Delta V/V]_{DX}\sim 10^{-1}$, where $[\Delta V/V]_{DX}=[\Delta V/V]_{d+}-[\Delta V/V]_{DX^-}$, $[\Delta V/V]_{d+}$= +0.22 for Sn (expansion), -0.064 for Si (compression); $[\Delta V/V]_{DX^-}$ = -0.19 for Sn and -0.22 for Si. This is derived from $3[\Delta a/a]_{DX}=[\Delta V/V]_{DX}\, x_{DX}$, where $x_{DX}=N_{DX}/N_{Ga}=0.5\Delta N_e/N_{Ga}$ (0.5 stems from the 2 electrons required for a DX^- state). Thus, the lattice expansion due to the emptying of the DX centers is attributed to the filling of the conduction band, related to the conduction band deformation potential and the bulk modulus.

Recently, Mäkinen et al (1993) have found a vacancy-related defect, observed by positron annihilation, in Sn- and Si-doped (Sn concentration $\sim 10^{18}$ cm^{-3}) MBE and metal-organic vapor phase epitaxy (MOVPE)-grown $Al_xGa_{1-x}As$ ($x\geq 0.18$). Here, vacancy-

associated positron trapping, suggesting that the defect's charge state in the ground state is either negative or neutral, was found to vanish when the samples were cooled to low temperatures (T=25 K) and then illuminated. These defects were not observed in undoped AlGaAs. The authors claim that this finding is consistent with the broken-bond model of the DX center (Chadi-Chang). That is, in the DX ground state the defect includes a vacancy created by the Sn moving to an interstitial site (leaving a vacant site sufficient for positron trapping) which is removed by the impurity moving into the substitutional site upon excitation. It was also found that upon heating the samples between 300 and 600 K positron trapping at vacancies was lost in both Si and Sn doped samples (thermal ionization of the DX center) which is reversible.

Finally, Mössbauer spectroscopy has been used on appropriate dopant atoms (Sn and Te) in GaAs and $Al_xGa_{1-x}As$ to probe the symmetry, charge state, and relaxation effects of the donor atom. Mössbauer absorber studies concerning the symmetry of donor atoms in GaAs (not under hydrostatic pressure) were conducted on LPE grown GaAs:^{125}Te (Williamson and Gibart 1981), LPE grown GaAs:^{119}Sn (Williamson 1986), and on (MOVPE) grown GaAs:^{119}Sn (Williamson et al 1987). Results of the GaAs:^{125}Te study showed that at a doping level of $1x10^{19}$ cm^{-3} Te donor and acceptor sites are identical, with the acceptor complex possessing higher symmetry than a proposed $(Te_{As}V_{Ga})^-$ complex (both are nearest neighbors). In their 2 and $3x10^{19}$ Te/cm^3 samples a Te site in addition to the acceptor and donor sites was observed. This additional site was attributed to Ga_2Te_3 microprecipitates or Te clusters. It was later suggested that this site

could also be associated with formation of Te DX centers due to the heavy doping (Williamson and Gibart 1989). From the LPE GaAs:^{119}Sn ($3.8x10^{17}<N_D-N_A<2x10^{18}$ cm^{-3}), Sn was found to occupy donor sites (Sn_{Ga}) and electrically inactive sites which match those of Sn_3As_2. Other phases may have also been present (β-Sn, SnAs, and Sn clusters). Samples which were annealed under As-rich conditions became partially compensated due to the formation of a Sn acceptor which had Mössbauer parameters consistent with a $Sn_{Ga}V_{Ga}$ complex. Three Sn species were observed in the MOVPE GaAs:^{119}Sn ($N_D-N_A<6x10^{18}$ cm^{-3}): Sn_{Ga} shallow donor, $Sn_{Ga}Sn_{As}$ and Sn_3As_2 (both electrically inactive clusters or microprecipitates). Annealing under AsH_3 created an acceptor which was again suggested to be $Sn_{Ga}V_{Ga}$. Williamson and Gibart (1991) have discussed their DX center Mössbauer absorber results on MOVPE $Al_xGa_{1-x}As$:^{119}Sn ($0\leq x\leq 1$, 10^{18}-10^{19} Sn/cm^3, 10^{16}-10^{18} n/cm^3) (Gibart et al 1988) and MOVPE grown GaAs:^{119}Sn under pressures >2.4 GPa (Gibart et al 1990). The atomic scale structure results from these studies suggest that there is a local distortion of the substitutional Sn site upon DX formation, with an upper limit on the amount of large lattice relaxation that is possible. The possibility that the local symmetry is less than cubic, has not been definitely established. The Mössbauer parameters from the pressure study on GaAs suggest that more than one electron is required to stabilize the DX center (negative-U behavior).

A displaced donor configuration (where a displaced donor relaxes into a substitutional site upon ionization) has been proposed based on Mössbauer parameters obtained from

MBE grown $Al_xGa_{1-x}As$ implanted with ^{129m}Te (source experiment) (Langouche et al 1989, Langouche 1989, Bemelmans et al 1992, Bemelmans et al 1993). PPC experiments were carried out after a 900°C rapid anneal. They have observed, for implantation doses $\geq 2x10^{14}$ cm^{-2}, a PPC effect which decayed over several minutes after the illumination was turned off. The Mössbauer data was fitted with a singlet+quadrupole resonance, which were attributed to the substitutional Te site and DX center, respectively. The fractional area of the singlet was measured as a function of time in the light and dark at 4 and 30 K. Upon illumination the singlet fraction was maximized at 10% and upon turning off the light, decayed to ~0% with time constants of 9 and 2 hours for 4 and 30 K, respectively. The decay of the singlet meant that the quadrupole resonance was increasing in area, showing that the DX centers are slowly returning to the ground state. Recent results from Wuyts et al (1992) showed that a comparative study of ^{129}I (source experiments using ^{129m}Te) Mössbauer data on Ga_2Te_3 and Te-doped GaAs gave firm evidence for $Te_{As}V_{Ga}$ complexes (Te atom quasi-substitutional on an As site with a Ga vacancy nearest neighbor) which they believe is relevant to the DX center configuration. The structure of Ga_2Te_3 is known to have the zincblende structure (as GaAs) and that one-third of the Ga sublattice positions remain vacant or two-thirds of the Te atoms are surrounded by three nearest neighbor Ga atoms and one vacancy (Te:3Ga,1V) whereas the other one-third has two Ga atoms and two vacancies as nearest neighbors (Te:2Ga,2V). Mössbauer spectroscopy was used to determine if the known Te environment in Ga_2Te_3 is similar to that found in GaAs:Te. The Te:3Ga,1V parameters

in the Ga_2Te_3 data were found to be similar to the Mössbauer parameters in one of the components in the GaAs data. This component corresponds to the $Te_{As}V_{Ga}$ defect in GaAs. This same component was found to exhibit PPC in another study (Bemelmans et al 1992).

Table 2.1 below summarizes the experimental work reviewed above.

Table 2.1. Summary of the experimental DX research reviewed. LLR=Large Lattice Relaxation, SLR=Small Lattice Relaxation.

x	Dopant	Technique	DX Model	Ref.
0	Sn, Te	Ballistic Phonons	Sn_{Ga} (111) distortion Te_{As} (110) distortion, LLR	Narayanamurti et al (1979)
0.42	Sn, Te	PIXE, RBS	$Sn_{Ga(Al)}$, Te_{As},SLR	Yu et al (1991)
0.25-0.76	Si, Te	DLTS	Group III substitutional-interstitial motion (LLR)	Dobaczewski et al (1992)
0.38	Se	EXAFS	Se_{As}, SLR	Kitano and Mizuta (1987, 1988)
0.35 0.45	S	EXAFS	S_{As}	Rowe et al (1989)
0 0.30 0.23	Sn	EXAFS	$Sn_{Ga(Al)}$, no LLR	Hayes et al (1989) Pant et al (1993) Lurio et al (1994)
0.22-0.24	Si, Sn	XRD	lattice relaxation due to conduction band filling	Cargill et al (1992)
≥0.18	Si, Sn	Positron annihilation	Si_i to $Si_{Ga(Al)}$ upon illumination	Mäkinen et al (1993)
0-1	Sn	Mössbauer	-U, local distortion of $Sn_{Ga(Al)}$	Williamson and Gibart (1991)
0.30 0.60	^{129m}Te	Mössbauer	displaced donor, $Te_{As}V_{Ga}$	Bemelmans et al (1992, 1993)

2.2 Proposed atomic-scale models

The first model for the atomic scale structure of the DX center was proposed by Lang, Logan and Jaros (1979) which consisted of a donor and anion (As) vacancy complex undergoing a large lattice relaxation upon photo-ionization. Computer calculations of the energies and wavefunctions of various native defects and chemical impurities in III-V compounds have led the authors to this model. They have also predicted differences in the DX structure between Te-doped and Sn-doped $Al_xGa_{1-x}As$: Te occupies an As site so that the TeV_{As} complex are second nearest neighbors while Sn occupies a Ga(Al) site so that the SnV_{As} complex are first nearest neighbors. The experimentally determined (DLTS and photocapacitance) energies for Te doped AlGaAs are thermal emission (E_e)=0.28±0.03 eV, thermal capture (E_c)=0.18±0.02 eV and optical emission (E_o)=0.85±0.1 eV. For Sn the energies are E_e=0.19±0.02 eV, E_c <0.1 eV and E_o=1.1±0.01 eV (Lang and Logan 1979).

Van Vechten (1985), using thermodynamics reasoning, has also proposed a donor-vacancy complex model for the DX center in AlGaAs, which differs from the Lang, Logan and Jaros model, thus: $D^+V_{III}^-Al_{As}^{-2}$, where D is a group IV or VI donor, V_{III} is a negatively charged vacancy on a group III site and Al_{As}^{-2} is an antisite defect. In this model the author claims that the $V_{III}^-Al_{As}^{-2}$ can compensate 3 D^+ and that the symmetry of this complex is consistent with experiments conducted by Narayanamurti et al (1979). The loss of n-type conductivity in the III-V alloys is an example of marginal self-compensation: the spontaneous generation of native defects to trap free carriers that have

been introduced by doping in states of lower free energy than the band edge. The author mentions that the term 'marginal' is applied to DX because this is a borderline case with compensation occurring only at low temperatures, subject to temporary reversal by photoionization. It was suggested that the energy of formation for a group V vacancy and transforming it to a V_{III}-III_V, trapping 3 electrons, is less than that to make 3 V_{III} which each trap one electron. In AlGaAs Al_{As} is favored over Ga_{As} because the Al, being more electro-negative, is expected to have shallower acceptor levels.

Yamaguchi (1986) determined the microscopic origin of the DX center in $Al_xGa_{1-x}As$ using a scattering-theoretic method calculation. The results showed that the central cell potential of donors induces the DX deep levels. The theory also predicts the x and pressure dependence of the DX center levels. It has been shown that the central cell potential of Si_{Ga}, Sn_{Ga}, and Se_{As} induces the deep levels attributed to the DX center. There was no mention of any complex involving a vacancy in the model.

An important microscopic model of the DX center in Si-doped $Al_xGa_{1-x}As$ has been proposed based on discrete variational Xα cluster calculations by Oshiyama and Ohnishi (1986). The calculated level structure showed that the antibonding A_1 state of Si shifts down into the energy gap upon distortion of the four neighboring As atoms in the case of $Al_xGa_{1-x}As$. The explanation of this model included: the symmetry of Si_{Ga} in GaAs (tetrahedral); the 3s and 3p orbitals of Si and neighboring atoms to produce a singlet A_1 and triplet T_2 states, respectively; A_1 and T_2 bonding states are in the valence band while the antibonding states are resonant with the conduction band; as AlAs mole fraction (x)

increases the band gap widens, the 12 second nearest neighbor Ga atoms around Si are replaced by Al atoms; the first nearest neighbor As atoms feel a strain field which trigger the distortion of the first nearest neighbor As around Si; bonds between the Si atoms are weakened, hence splitting between the bonding and antibonding A_1 or T_2 states decreases which causes the antibonding states to move into the gap. The authors argue that this level is the deep level of the DX center.

Another important model for the atomic structure of the DX center was proposed by Chadi and Chang (1988, 1989). Part of their model was the prediction of negative-U behavior of the DX center (localization of 2 electrons in the ground state). The authors have used ab initio pseudopotential calculations on Si and S induced DX centers in $Al_xGa_{1-x}As$. The results include: the DX center is negatively charged and highly localized, which results from a large dopant dependent lattice distortion; bond breaking, lattice relaxations, which are responsible for deep-electron trap formation by DX centers, are relevant to substitutional donors (Si on Ga site, S on As site); formation of these defects may be suppressed by the introduction of interstitial donors from group III or V; the distortion involved is a large Si movement along <111> or a large nearest neighbor Ga (or Al) movement along <111> in the case of S on an As site and hence a C_{3v} symmetry (for a negatively charged center).

Jones and Öberg (1991) have carried out local-density-functional cluster calculations on the Si^-_{Ga} defect in GaAs. They found that the Chadi-Chang model had the same energy as a simple breathing distortion of the As neighbors. In 1992, Chadi proposed that

the substitutional donors in $Al_xGa_{1-x}As$ have two distinct negatively charged DX-like deep donor states. The first state has a broken-bond atomic configuration (C_{3v} DX^- type) while the second arises from a symmetric breathing mode atomic relaxation around the impurity (tetrahedral $DX^{'-}$ state). The energies for these two configurations, determined from first-principle pseudopotential calculations, are close for Sn, S, Se and Te. Morgan (1991) has described a vacancy-interstitial model for $Al_xGa_{1-x}As$ in which the substitutional donor relaxes toward an interstitial site when they are in the ground state. That is, the donor atom moves into one of the four surrounding interstitial sites and rebinds to the new Ga and Al neighbors. This model is seen to be consistent with the Chadi-Chang one.

Yamaguchi et al (1991) have also investigated the atomistic nature of the DX center in GaAs, $Al_xGa_{1-x}As$, and AlAs/GaAs superlattices via an ab initio self-consistent pseudopotential method. They found that the most stable state for the DX is the T_d distorted atomic configuration around a substitutional donor with the neighboring bond relaxation given by a certain percentage of the effective ionic radius (7.7% for Sn_{Ga}, 0.7% for Si_{Ga}, both under 30 kbar in GaAs). The T_d distortion involves the symmetric relaxation of four first nearest neighbor bonds and twelve second neighbor bonds around a substitutional donor-impurity (i.e. T_d point symmetry is preserved). Two other distortions were investigated: D_{2d} (dislodging of four nearest neighbor As atoms so as to make two pairs of GaAs) which did not exhibit a local energy minimum and therefore would not contribute to the DX center; C_{3v} (broken bond configuration at a negatively

charged donor where one of every two Si atoms is moved away from one of its nearest neighbor As atoms along the bond axis into a three-fold coordinate interstitial position) which was not as stable as the T_d configuration. Recall that Chadi and Chang claimed that C_{3v} is stable. It was also found that a deep A_1 level (composed of atomic s states of an impurity and its neighboring atoms) attributable to the DX center is induced by a simple substitutional donor with the obtained lattice configuration (T_d) and appears in the band gap when pressures are >24 kbar in GaAs or when $x \geq 0.3$ in $Al_xGa_{1-x}As$.

Cheong and Chang (1992) investigated the structural and dynamical properties of the Si DX center in GaAs under pressure through self-consistent ab initio pseudopotential calculations. They have found the negatively charged broken-bond configuration in the ground state for the DX center in GaAs:Si above 24 kbar. Although the tetrahedrally symmetric breathing-mode distortion of the donor neighbors produces a localized state, this state is less stable and the authors had difficulty explaining a large Stokes shift, compared to the broken-bond configuration.

Saito, Oshiyama and Sugino (1993) have used large-scale supercell calculations within the local density approximation to model the Si-related DX center in GaAs. A highly efficient conjugate-gradient minimization technique was combined with norm-conserving-pseudopotential methods in order to include both short-range and medium-range lattice relaxations. The total energy calculations for several geometries were investigated for Si in GaAs: the broken-bond model $(Si_iV_{Ga})^{-1}$, the on-site model $(Si_{Ga})^{-1}$, the shallow state (D^o), the transition state $[(Si_iV_{Ga})^{-1}]^*$, and several metastable geometries involving large

lattice relaxation: $(As_{Ga}Si_{As})^{-1}$, and three $(Si_{Ga}Ga_iV_{Ga})^{-1}$ geometries. The authors have found that the Si-As bonds in the broken-bond geometry $(Si_iV_{Ga})^{-1}$ are stabilized by $sp^{2.4}$ hybridization of the Si atomic orbitals (Si is distorted from its substitutional site along $[\bar{1}\bar{1}\bar{1}]$) while the Si-As bonds in the on-site geometry $(Si_{Ga})^{-1}$, are weakened by the electrons in the gap level with localized anti-bonding character. The bond lengths for these two geometries are 2.41 and 2.53 Å, respectively. The bond length for $(Si_{Ga})^{-1}$ is similar to the length of the shallow donor (D^o) geometry. The total energy in the broken-bond geometry, $(Si_iV_{Ga})^{-1}$, is slightly lower than that in the on-site one, $(Si_{Ga})^{-1}$, supporting the broken-bond model of the DX center (similar to Chadi-Chang). Also, the broken-bond geometry was found to have the lowest energy among the geometries accompanied by large lattice relaxation. The emission barrier for the broken-bond geometry was estimated to be 0.30 eV, which is consistent with the experimental value of 0.33±0.02 eV (Mizuta et al 1985, Mooney et al 1988, Baba et al 1989). Finally, the neutral broken-bond geometry was found to be unstable and since there is no barrier between the on-site and broken-bond geometries, this suggests that the Si atom moves to the substitutional site after the DX center is photo-excited. In a later report Saito and Oshiyama (1993) have shown that the hybridization of the broken-bond configuration of the Sn DX center in GaAs to be $sp^{2.2}$ and the emission barrier to be 0.18 eV. The displacement of the Sn atom along the $[\bar{1}\bar{1}\bar{1}]$ axis is 1.29Å and 2.60 Å for the Sn-As bond length with a bond angle of 117°, which is slightly smaller than the sp^2 hybridization angle (120°). Thus the Sn atom has a dangling s-p bond in the $[\bar{1}\bar{1}\bar{1}]$ direction. The

remaining three-fold As atom moves inward by 0.13 Å along the [$\bar{1}\bar{1}\bar{1}$] axis. This inward motion allows the Ga-As bond angle (106°) to be less than the tetrahedral angle (109.5°). Total energies of several negatively charged geometries for the Sn impurity were evaluated and the authors found that the $(Sn_iV_{Ga})^{-1}$ broken-bond geometry to be the lowest in energy (same result for Si as described above). Table 2.2 below summarizes the proposed atomic scale models of the DX center discussed above.

Table 2.2. Summary of the proposed atomic scale models of the DX center reviewed ([n.]n.n.= [next] nearest neighbor).

Atomic Scale Model for DX Center	Reference
IV_{III} or VI_V + As vacancy (LLR)	Lang, Logan, and Jaros (1979)
$D^+V_{III}^-Al_{As}^{-2}$	Van Vechten (1985)
IV_{III} and VI_V related	Yamaguchi (1986)
Sn_{Ga} with 12 next n.n. Al causing strain on As n.n.	Oshiyama and Ohnishi (1986)
Broken-bond configuration in ground state, substitutional in excited state (C_{3v} symmetry)	Chadi and Chang (1988, 1989) Morgan (1991) Saito, Oshiyama and Sugino (1993) Saito and Oshiyama (1993)
LLR is breathing distortion of As n.n. of Si_{Ga}	Jones and Öberg (1991)
T_d symmetry (4 n.n. and 12 n.n.n. relax around substitutional impurity)	Yamaguchi et al (1991)
-U, broken-bond for Si in x=0 for P>24 kbar	Cheong and Chang (1992)

3. Sn Doping of GaAs and $Al_xGa_{1-x}As$

3.1 Background

3.1.1 Ion implantation

Doping by ion implantation is a primary step in the fabrication of compound semiconductor devices and integrated circuits. It also has numerous advantages over thermal diffusion, the important of these being: good dopant profile control, excellent reproducibility, high throughput, doping levels well above the solid solubility limits, and allows the use of simple masking methods (oxides, nitrides and photoresists). However, ion implantation suffers from several disadvantages: creation of radiation damage which requires high temperature annealing to restore the crystal lattice and move the implanted ions onto electrically active sites (residual damage may be present after annealing), production of very thick doped layers (> 5 μm) is not possible, diffusion during annealing or channeling during implantation can alter the expected dopant depth profile (lateral straggling is a fundamental limit to the downsizing of device dimensions). Two of these disadvantages can be overcome by using rapid thermal annealing techniques which can provide electrical activation of the doping species while minimizing diffusion effects (Allsop 1988, Pearton 1988, Gill 1988). N-type ion implantation dopant species are preferred over p-type because of the factor of ten higher carrier mobilities in GaAs (Pearton 1988).

Most of the work on ion implantation doping of the III-V compounds has focused on

dopant species such as Si, Sn, Te, Cd, and Ge: Shim et al (1987) [Sn], Adachi (1988) [Si], Ramsteiner et al (1988) [Si], Campbell et al (1989) [Si], Shim and Itoh (1989) [Si, Sn], Pearton et al (1989) [Sn, Te, Cd] Lee et al (1990) [Si], Moore et al (1990) [Si], Moore and Deitrich (1990) [Si], Allen et al (1991) [Si, Sn, Ge], Vanasupa et al (1991) [Si], Palmetshofer et al (1991) [Si], Haynes and Holland (1991) [Si, Sn], Wei et al (1992) [Si], Cho et al (1992) [Si], Thompson et al (1992) [Sn], Fujii et al (1992) [Se], Moriya et al (1993) [Cd], Shibata et al (1993) [Sn]. The previous work on the Sn implantation doping of III-V semiconductors is discussed below.

Shim et al (1987) have implanted liquid encapsulated Czochralski (LEC) grown GaAs (100) with 150 keV Sn^+ to doses of $5x10^{14}$, $1x10^{15}$ and $3x10^{15}$ cm^{-2} at room temperature at an angle of 8° with respect to the <100> axis to avoid channeling. Si films, 300 nm thick, were used as annealing caps. No diffusion of Si into the GaAs was detected by SIMS after an anneal at 900°C for 15 min. SiO_2 films were deposited on the back of the samples. These were annealed at 850°C for 15 min in flowing N_2 gas. The Si and SiO_2 films were removed using an organic etchant and HF, respectively. Radiation damage, residual defects, and lattice location and distribution of Sn were characterized by channeling RBS combined with PIXE and TEM. Electrical measurements were done by differential Hall measurements. Using aligned RBS, the as-implanted projected range of Sn was found to be 40 nm, which was in good agreement with the Lindhard-Scharff-Schiøtt (LSS) theory (40.7 nm). TEM showed that the density and sizes of dislocations, residing in the (100) plane, increased with increasing implant

dose. Black spots were also found and attributed to Sn precipitates which pinned the dislocations. The precipitate density in the $3x10^{15}$ Sn/cm^2 dose was 7 and 100 times higher than those in the $1x10^{15}$ and $5x10^{14}$ cm^{-2} implant cases. From their RBS data, significant diffusion occurred after 850°C and 15 min for the $3x10^{15}$ cm^{-2} dose but the peak in concentration remained under 100 nm (i.e., an increase in the tail of the distribution) with values of 10^{20} cm^{-3} for the $5x10^{14}$ and $1x10^{15}$ cm^{-2} doses and $3.3x10^{20}$ cm^{-3} for the $3x10^{15}$ cm^{-2} dose. They also found, by RBS aligned profiles, that in the annealed sample the implanted Sn remained in the interstitial sites distributed within the implanted layer while the diffused Sn from the implanted layer are in the substitutional sites of the substrate (the unimplanted region). The peak substitutional Sn concentrations were $6x10^{19}$-$1x10^{20}$ cm^{-3}. The Hall carrier concentration varied from $4x10^{17}$ cm^{-3} near the surface to $2x10^{18}$ cm^{-3} approximately 250 nm deep, with the Hall mobility remaining at 1500 cm^2/V-s in all the samples after the anneal for all doses. Table 3.1 below summarizes the relation between dose and substitutional fraction, electrical activation ratio and substitutional impurity activation ratio (sheet carrier conc./dose). It was found that only 2.85 ±0.15 % of the Sn in the substitutional sites activated as donors after annealing.

In a later paper by Shim and Itoh (1989), using the same conditions as above, they have found that using a 150 keV Sn^+ dose of $1x10^{14}$ cm^{-2} (lower than the previous study) provided a higher activation ratio of 12%, a peak carrier concentration of 10^{18} cm^{-3}, Hall mobility of 2140 cm^2/V-s (at 10^{18} cm^{-3}), compensation ratio of 2.6 (N_A+N_D/n) and an impurity ionization ratio of 13% (ionized impurity conc. / predicted peak impurity conc.

Table 3.1 Sn implantation into GaAs results from Shim et al (1987)

Implanted Dose (Sn/cm^{-2})	Substitutional Fraction (Sn_{Ga} , Sn_{As}) (%)	Activation Ratio (%)	Substitutional Impurity Activation Ratio (%)
$5x10^{14}$	88	2.6	3.0
$1x10^{15}$	64	1.8	2.8
$3x10^{15}$	35	1.1	2.7

from the LSS range parameters). The ionized impurity concentration was obtained from the compensation ratio using the relation $n=N_D^+-N_A^-$. The depth profiles of carrier concentration and mobility were determined by means of Hall measurements with successive anodic oxidation and stripping.

Pearton et al (1989) have studied the relationship between electrical activity, dopant solubility and diffusivity, as a function of the substrate temperature during 100 keV Sn implantation (7° tilt, 15° rotation relative to (110) flat) into LEC grown GaAs. Implant doses ranged from $5x10^{12}$ cm^{-2} to $5x10^{15}$ cm^{-2}, a temperature range of -196 to 400°C followed by either transient (950°C, 5 s) or furnace (450-900°C, 20 min) annealing. In both annealing methods the implanted layer was protected with an undoped GaAs wafer (proximity cap). The furnace anneals used a flowing As-H_2 ambient and the transient anneals, flowing forming gas (90% N_2:10% H_2). From their electrical measurements

(differential Hall probe), the authors stated that no electrical activity was found after 650°C furnace annealing for any of the doses investigated, and activation percentages of only 10% for 10^{15} cm^{-2} dose implants annealed at 750°C and above. However, the authors show data which corresponds to an activation of ~ 70% (sheet carrier conc./Sn dose=$7x10^{12}/10^{13}$) for a room temperature implant and 850°C and 20 min anneal. They do not discuss this result. Depth profiles (SIMS and C-V) showed that there was little diffusion and no loss of Sn after annealing at 850°C and 20 min with a dose of 10^{15} cm^{-2} (activation of 10%). As a function of implant temperature, a thick amorphous layer was formed at -196°C (dose=$10^{15}cm^{-2}$) having an ion range distribution closely resembling the LSS prediction. At room temperature, a thinner amorphous layer was formed due to self-annealing. Implantation at 200 or 400°C prevented amorphization of the GaAs lattice although RBS indicated the presence of dislocations in the end-of-range region. Diffusional broadening and/or partial channeling was found at 200 and 400°C and was attributed to the increased mobility of vacancies and interstitials assisting the Sn motion. After subsequent rapid annealing, all of the Sn in the tail region of the distribution was electrically active while less than 10% of the Sn in the high concentration near-surface region was active. The fact that the mobile form of Sn, presumed not to be complexed with lattice defects or be in a precipitated form, is electrically activated is evidence linking the interaction of implanted species with point defects (such as V_{As}, V_{Ga}, Ga_{As}, As_{Ga}) as a controlling factor in activation. Approximately 40% of the Sn is in substitutional sites after furnace annealing and 70% after rapid thermal annealing (based

on 100 keV Sn, $1x10^{15}$ cm^{-2}, room temperature implant). Except for the implant performed at -196°C, rapid annealing gave higher solubilities than furnace annealing, and also less diffusion of the Sn for all implant temperatures. There is a discrepancy in the results for the percent Sn on substitutional sites between these authors and Shim et al (1987) for the 10^{15} cm^{-2} dose. Similar sample growth and implantation methods were used by both, with different implantation energies (150 keV [Shim et al] and 100 keV [Pearton et al]). Both, however, used different surface capping methods: Shim et al used 300 nm Si film caps while Pearton et al used GaAs proximity caps. Pearton et al used a rapid anneal (950°C x 5 s) whereas the others did not. For the furnace anneals, Shim et al obtained 64% Sn on Ga and As sites while the other group obtained 40% (they did not specify if this included the As sites as well, but acknowledged that Sn is amphoteric). The results from the rapid anneal by Pearton et al (70%) is close to 64% obtained by the others. According to an earlier study by Shim et al (1986) their Si film caps did not contain any Ga or As after a 950°C x 15 min anneal according to RBS and therefore was below $2x10^{18}$ cm^{-3} (the RBS detection limit). Lower concentrations than this may still be significant in terms of the creation of V_{Ga} and V_{As} in the sample which may explain why there was larger incorporation of Sn on substitutional sites (at least for furnace anneals) for Shim et al (1987).

The diffusion behavior of Sn-implanted GaAs has been investigated by Allen et al (1991). LEC grown GaAs (semi-insulating or Si or Te doped) and horizontal-Bridgman-grown GaAs (Si or Zn doped) were implanted with ^{118}Sn at 185 keV (a projected range

of 44 nm). Ion doses ranged from $1x10^{13}$ to $5x10^{15}$ cm^{-2}. The implanted substrates were capped with 90 nm of Si_3N_4 by plasma-enhanced chemical vapor deposition (PECVD). Post-irradiation anneals were done at different times from 5 min to 10 h and at temperatures ranging from 700 to 1000°C in an open-tube furnace under flowing forming gas. After stripping the caps, dopant depth profiles were analyzed using SIMS. Carrier profiles were obtained by either electrochemical C-V profiling or by stripping Hall (van der Pauw) measurements using dilute H_2O_2:NH_4OH:H_2O as an etchant. From their profiling data and using the Fermi level model (the position of the Fermi level determines the diffusivity), with the assumption that the dopant diffuses via $(V_{Ga})^{-m}$, where -m is the charge state of the vacancy, the authors have found the best fit to the data to be $D=8x10^2cm^2/s(n/n_i)^2exp(-4.1eV/kT)$, where n and n_i are the electron and intrinsic concentration, respectively. The $(n/n_i)^2$ term describes that diffusion is via $(V_{Ga})^{-2}$, which held true for all doses and anneal times.

Dose rate effects on damage formation in Sn implanted GaAs was studied by Haynes and Holland (1991) using 360 keV $^{120}Sn^+$ at 300 K and undoped or n-doped (100) GaAs. To minimize channeling the samples were tilted 7° with respect to the beam direction. The projected ranges (using TRIM) were 100 nm. Ion induced damage was determined by ion channeling spectra along the <100> direction with 2 MeV He^+ and a 160° scattering angle at room temperature. Using a dose of $3x10^{13}$ Sn/cm^2 produced a damage dose rate effect obeying the power-law $N_d\alpha 0.2J^m$=displacements/cm^2, where N_d is the integrated total damage (scattering centers/cm^2) determined from ion channeling

experiments, α is a factor not defined in the article, and J (in $\mu A/cm^2$) is the average dose rate.

Thompson et al (1992) have used a very low energy (1 keV) focused Sn ion beam to dope MBE GaAs during growth. The Sn ion beam consisted of 60 % Sn^{++} and 40% Sn^{+} from a Sn liquid metal ion source (LMIS). The acceleration potential used was 1 kV thus producing 60% 2 keV Sn^{++} and 40% 1 keV Sn^{+} beams. The sample was isolated from ground during growth such that it could be raised to a high voltage. The ion landing energies were varied from 50 to 500 eV by changing the high voltage on the sample from 950 to 500 V (with respect to the 1 keV Sn beam). The GaAs was grown at a rate of 1 μm/hr at temperatures between 590 and 615°C. Three dimensional patterns could be produced in the doping concentration as the GaAs was grown via beam rastering. The bulk GaAs had carrier concentrations from 10^{14} to $8x10^{16}$ cm^{-3}. The focused ion beam was 70 μm in spot size at 50 eV and 1 nA beam current. From electrochemical C-V and SIMS profiling it was observed that as the incident ion energy is increased fewer conducting electrons were produced as a fraction of the total number of Sn atoms in the sample. The authors attribute this to either compensating acceptors caused by implantation damage or a lower activation level for the Sn donor. Above 150 eV ion energies the carrier concentration dropped rapidly. Hall measurements show mobility versus carrier concentration ranging from 10^5 cm^2/V-s at 10^{14} cm^{-3} to 10^4 cm^2/V-s at 10^{17} cm^{-3} (for 50-160 eV). Thus, focused ion beam methods allow the growth of high quality GaAs. Finally, 4 K photoluminescence showed negligible effects due to

implantation damage (50 eV ions). Narrow peak linewidths corresponded to good quality Sn-containing layers. A large peak due to a carbon (possibly from the growth process) on an arsenic site was detected. A small peak due to Sn acceptors was seen.

Shibata et al (1993) investigated the influence of UV laser irradiation on the implantation damage, residual defects and redistribution of implanted atoms in Sn^+ implanted GaAs using RBS, SIMS and Raman scattering. Using a triple implantation method at three different energies: 120, 220, and 400 keV a flat profile, about 80 nm thick, could be produced, based on the LSS theory. The implantation dose was controlled so as to realize Sn concentrations in the flat profile region corresponding to 10^{17}, 10^{18}, 10^{19}, 10^{20} and 10^{21} cm^{-3}. The UV laser irradiations were performed in air using an ArF excimer laser (pulse width= 20 ns, λ=193 nm) at several energy densities from 200 to 1400 mJ/cm^2. From RBS the total thickness of the disordered layer implanted at a dose corresponding to 10^{21} cm^{-3} Sn was 250 nm (3 times LSS theory). Disorder appeared for doses corresponding to 10^{19} cm^{-3} or higher. With increasing laser energy density, ordering and disappearance of the damage layer were observed. For 300 and 400 mJ/cm^2, residual disorder was found in the vicinity of the interface between the disordered layer and the single crystal layers suggesting that ordering of the damage proceeds in the direction from surface into bulk. The RBS data also suggested Sn segregation after laser irradiation, arising from "zone-refining" in the laser-melt region. Enhanced segregation was found for higher energy densities but saturated $\geq$800 mJ/cm^2 which was interpreted as redistribution from interstitial to substitutional sites. The ratio of scattering yield from

Sn in their aligned RBS spectrum to that in their random spectrum was estimated to be ~54% in the 1200 mJ/cm^2 irradiated sample. Using this and the minimum yield for GaAs (χ_{min}=0.04) the authors estimated that approximately half of the Sn should be on substitutional sites. The segregated layer had a Sn concentration of 1.1x10^{22} cm^{-3}, an order of magnitude larger than the initial concentration in the as-implanted samples, with a thickness of ~10 nm. Their SIMS data show a dramatic increase in the Sn concentration at the surface region after laser irradiation suggesting strong Sn segregation, which also showed to be 10 nm thick. Raman scattering parameters showed the average size of an undamaged region in the sample to be 4.5 nm in the as-implanted sample (10^{21} Sn/cm^3) and increased steeply with increased laser energy density.

3.1.2 Thermal diffusion

Conventional methods for doping III-V compounds include doping during growth by MOCVD, MBE, LPE or, as just discussed, by high energy ion implantation after growth followed by rapid thermal annealing to remove damage and electrically activate the implanted species. An alternative method for the doping of III-V compounds is by thermal diffusion. Certain key dopants have been used when applying this technique: donors- Si, Se, Sn (Goldstein and Keller 1961, Fane and Goss 1963, von Muench 1966, Yamazaki et al 1975, Tuck and Badawi 1978, Baliga and Ghandhi 1979, Nissim et al 1980, Arnold et al 1984, Guido et al 1988, Pavesi et al 1992); acceptors- Zn, Cd (Goldstein 1960, von Muench 1966).

The most common method for preparing samples, as described by several of the above authors, is to thermally diffuse the dopant in a closed environment, i.e. in a sealed fused silica ampoule which is initially evacuated. The ampoule would typically contain GaAs (or $Al_xGa_{1-x}As$), elemental As, and the dopant. Incorporation of the dopant into GaAs is via the vapor phase, so high temperatures (800-1200°C) are typically required. Arsenic is used to provide an overpressure at the diffusing temperature, which serves as a possible diffusion enhancing mechanism for the dopant via column III vacancies and to prevent the surface of the sample from decomposing at the higher temperatures. This decomposition has been observed as surface erosion due to a loss of As and formation of V_{As} (von Muench 1966, Yamazaki et al 1975, Tuck and Badawi 1978, Baliga and Ghandhi 1979, Arnold et al 1984). A variation on this sample preparation technique was to use SiO_2 or Si_3N_4 capping layers (which may be doped or not) to preserve the GaAs surface and provide a diffusion doping source (von Muench 1966, Yamazaki 1975, Baliga and Ghandhi 1979, Nissim et al 1980, Arnold et al 1984, Guido et al 1988, Carriere et al 1990, Allen et al 1991, Seaward 1992) .

A discussion concerning vapor pressures over GaAs is provided by Arthur (1967). Using mass spectrometric and weight loss measurements in the temperature range 627-927°C he determined the As_2/As_4 vapor pressure ratio over GaAs. It was found that $P(As_2)>P(As_4)$ for the temperature range studied. Both of these pressures approached 1 atm at the melting point of GaAs. For temperatures below 680°C, $P(Ga)>P(As_2)>P(As_4)$. Cohen (1991) and Tan et al (1991) also showed that in equilibrium the dominant As

vapor species are As_2 and As_4 over GaAs. It is therefore clear that when elemental As is added in the ampoule its vapor exists as a mixture of As_2 and As_4.

It has been suggested that when capping layers, such as silicon oxide or silicon nitride, are deposited on GaAs they act as efficient barriers to the out-diffusion of As and therefore provide an As-rich environment at the capping layer-GaAs/AlGaAs interface without any As overpressure (Cho et al 1992, Tan et al 1991, Katayama et al 1991).

Tan et al (1991) also gave a thorough discussion concerning the point defects and diffusion mechanisms in GaAs-based materials. There are six intrinsic point defects which are associated with GaAs: V_{Ga} (acceptor), V_{As} (donor), I_{Ga}, I_{As} (both deep donors), Ga_{As} (double acceptor) and As_{Ga} (deep donor). Any of these can be paired to form complexes, but only the single point defects are important to impurity diffusion. Tan et al have shown that when considering the four defects (I_{Ga}, I_{As}, V_{Ga}, V_{As}) that as As_2 (or As_4) pressure increases over GaAs, the concentration of I_{As} and V_{Ga} increases while that of V_{As} and I_{Ga} decreases. In the case of $Al_xGa_{1-x}As$, V_{Al} also increases (Olmsted and Houde-Walter 1992). Using Sn as a n-type dopant in GaAs, it is found to predominantly sit on the Ga sublattice to form Sn^+_{Ga} donors when under an As overpressure (causing an excess of V_{Ga} by which Sn diffuses). Although, if there is an excessive Sn population in GaAs, compensation may occur with $(Sn_{As}2V_{Ga})^-$ (Panish 1973, Ho et al 1991), Sn^-_{As} or $(Sn_{Ga}V_{Ga})^-$ (Hurle 1979) species possible. Deppe et al (1987) have concluded from their TEM and carrier concentration measurements for Se (n-type) doped $Al_xGa_{1-x}As$: GaAs superlattices the Ga-Al (group-III) interdiffusion occurs through the interaction

between the Se^{+}_{As} impurity and native defects (most likely V_{Ga}) associated with As-rich conditions. Cohen (1991) showed that interdiffusion and self-diffusion in GaAs may be controlled by either the vacancy or interstitialcy mechanism, and that it is possible to switch between the two by changing the Fermi level or As pressure. The boundary between the two mechanisms was $P(As_4)$=1 atm, $E_F=E_i$ (mid-gap energy in intrinsic material) with $D(I_{Ga})$ for < 1 atm As and $D(V_{Ga})$ for > 1 atm As, where D is the diffusion coefficient. Presented below are results from the thermal diffusion of Sn in GaAs under a closed environment (*no data were found for $Al_xGa_{1-x}As$*). It is assumed that the use of the term 'quartz' in the references reviewed below refers to the amorphous phase of SiO_2 (fused silica)

Goldstein (1960) and Goldstein and Keller (1961) have thermally diffused radioactive ^{113}Sn (evaporated on the GaAs surfaces) into GaAs by sealing samples in evacuated quartz ampoules with an As overpressure (pressure not specified) to avoid decomposition of the GaAs surface. Temperatures and times ranged from 1069-1215°C and $2.6x10^5$-$6.0x10^5$ seconds. The diffusion constants were calculated from semi-log plots to give a behavior consistent with $D=D_0exp(-E/kT)$ with $D_0=6x10^{-4}$ cm^2/s and E=2.5±0.1 eV. They have concluded that given the donor property of Sn in GaAs that Sn diffused via V_{Ga}. Depth profiles were obtained by precision lapping and measuring the specific activity in each lapped section with a Geiger counter. The $\sqrt{(Dt)}$ depth at 1201 ($2.59x10^5$ s), 1140 ($3.29x10^5$ s), and 1069°C ($6.03x10^5$ s) were 7.5, 5.7, and 4.2 μm, respectively.

Fane and Goss (1963) sandwiched GaAs between 2 quartz flats, to prevent surface

decomposition, in sealed, evacuated ($P=10^{-5}$ Torr) ampoules along with As and diffusant. In some cases natural Sn was deposited on the quartz flats by thermal evaporation while a radioactive $^{113}SnCl_2$-HCl solution was used to electroplate 50-100 $\mu g/cm^2$ of ^{113}Sn on GaAs. Good polished surfaces were retained during diffusion at temperatures up to 1150°C. The variation in diffusion depth with As pressure was investigated at 1100°C and 16 hours. They have found an increase in diffusion depth by a factor of 2 in the range 0.1-1.0 atm As, saturating at pressures above 1.0 atm at a maximum depth of approximately 15 μm. Surface concentrations were from 10^{20}-10^{21} cm^{-3}. The depth profiling technique was similar to that used by Goldstein (1960).

Von Muench (1966) has used a pyrolytic deposition technique for depositing Sn doped SiO_2 layers on Zn-doped ($p=2.5x10^{17}$ cm^{-3}) GaAs. These doped layers were then used as solid sources for diffusion at 1000°C. The samples were then subjected to a selective etching technique yielding eight steps of different oxide thickness on each wafer. The oxide thickness was determined for each step using interference microscopy. The diffusion runs were carried out in evacuated quartz ampoules with an amount of As added corresponding to the equilibrium As pressure of GaAs at the diffusion temperature. The junction depth was determined for each step by bevelling and staining techniques. Junction depth versus thickness data of the Sn doped oxide layer were obtained for 1, 4, and 8 hour runs at 1000°C. It was found that for oxide depths >1000 Å there is little change in the junction depth (infinite source condition). These depths ranged from 1 μm for a 1 hour run with a 3000 Å oxide layer to approximately 3 μm with an 8 hour run

with a 4700 Å oxide layer.

Yamazaki et al (1975) have also used Sn doped SiO_2 layers as solid diffusion sources for Cd-doped ($p=1.5x10^{17}$ cm^{-3}) GaAs. The oxides were prepared by thermal decomposition of ethylorthosilicate with tetramethyltin (TMT) or tetraethyltin (TET). The oxide thickness was 0.7 μm. The diffusions were carried out at 800-1100°C in sealed quartz ampoules with As. Depth profiling was obtained by a successive step etch technique combined with van der Pauw measurements. The profiles fitted complementary error functions. The maximum carrier concentration obtained was $7x10^{18}$ cm^{-3} for TMT and $1\text{-}2x10^{18}$ cm^{-3} for TET (TMT provided a higher Sn concentration in the oxide). It was found that in the range of high Sn concentration, the amount of electrically active Sn was <0.1 x (total diffused Sn). At the maximum depth most of the Sn became activated (≈4 μm). For 1000°C diffusion the depth increased with increasing As_4 pressure from 0.1-1 atm saturating above 1 atm. For T<900°C the depth was almost independent of As pressure. For As pressures ≥1 atm and using the TMT source to prepare the Sn-doped oxide, the diffusion depth varied from 1 μm at 800°C to 4 μm at 1000°C (4 hour run). The diffusion coefficient for the TET source, under 1 atm As, was given by $D=1.0x10^{-5}exp(-2.0eV/kT)$ cm^2/s.

Tuck and Badawi (1978) have conducted a series of experiments in which radioactive ^{113}Sn was diffused into 3 types of GaAs: undoped with $n=2x10^{16}$ cm^{-3}, Sn-doped with $n=2.4x10^{18}$ cm^{-3}, and Te-doped with n ranging from $10^{17}\text{-}10^{18}$ cm^{-3}. The radioactive ^{113}Sn was applied as a Sn powder + alcohol mixture, leaving microgram amounts of Sn

on the sample. These samples were sealed in evacuated quartz ampoules (10^{-6} Torr) along with a bare GaAs wafer, and in most cases some As was added. Diffusions were carried out over a temperature range of 850-1100°C and with times between 1.5-88 hours. Carrier concentration profiles were obtained via C-V measurements. Samples prepared under 0.7 atm of As vapor gave good reproducible results with very little mass loss in GaAs. The diffusion profiles for the undoped samples were fitted reasonably well using complementary error function curves. For 1100°C and 2 hours the Sn concentration profile showed a $\sqrt{(Dt)}$ depth of approximately 1.4 μm with the behavior $D=3.5\exp(-3.3eV/kT)$ cm^2/s. The solubility of Sn in this case was approximately 10^{19} cm^{-3} with an electron density of $3.4x10^{18}$ cm^{-3}. For diffusion into Sn-doped samples the Sn concentration: electron density ratio was approximately the same as in the undoped samples. The diffusion coefficient for these was $D=7.6x10^{-8}\exp(-1.2eV/kT)$ and the $\sqrt{(Dt)}$ depth was approximately 1.4 μm for 1100°C and 2 hours. For diffusion into the Te doped samples a determination of D_o and E could not be done because of the large variation in the electron densities of the samples used, although D varied from $4.2x10^{-14}$ cm^2/s at 900°C for 20 hours ($\sqrt{(Dt)}$ depth of 0.55 μm) to $4.7x10^{-12}$ cm^2/s at 1100°C for 1.5 hours ($\sqrt{(Dt)}$ depth of 1.6 μm). The Sn solubility was approximately 10^{19} cm^{-3}. Radio-tracer experiments on the non-radioactive Sn-doped sample showed that there was an exchange between the two types of Sn (isoconcentration diffusion). Table 3.2 below summarizes the Sn diffusion data discussed above. A determination of the diffusion depth ($\sqrt{(Dt)}$) at 1000°C for 12 hours is given.

Discrepancies between the different depth values is possibly due to the different conditions, such as initial doping of the GaAs and differences in As pressures. Also, the wide range of activation energies and diffusivities may be due to intrinsic defects present in GaAs before thermal diffusion doping (i.e. interstitials, vacancies and antisites) which can create a complex defect system with Sn.

Table 3.2 Summary of the Sn diffusion data from the literature

$D_o(cm^2/s)$	E(eV)	D(1000°C)	√(Dt) (μm)	Reference
$6x10^{-4}$	2.5	$7.9x10^{-14}$	0.6	Goldstein and Keller (1961)
$1x10^{-5}$	2.0	$1.2x10^{-13}$	0.7	Yamazaki et al (1975)
3.5	3.3	$3.2x10^{-13}$	1.2	Tuck and Badawi (1978)
$7.6x10^{-8}$	1.2	$1.4x10^{-12}$	2.5	Tuck and Badawi (1978)

3.2. Experimental Procedures

Described below are the experimental techniques used to produce Sn-doped III-V materials via thermal diffusion and thin film SiO_x and Si_xN_y capping layers to protect the III-V surface during thermal processing. Characterization techniques used in this study include Auger electron spectroscopy (AES), secondary ion mass spectroscopy (SIMS),

electrochemical capacitance-versus-voltage (C-V) for depth profiling; x-ray diffraction (XRD) for compositional and structural analysis.

3.2.1 Sample preparation

In this study the undoped and Si-doped GaAs wafers (polished) used were purchased from Crystal Specialties and were grown by the vertical and horizontal Bridgman methods, respectively. These were cleaned with methanol and then deionized water.

The undoped $Al_xGa_{1-x}As$ (x=0.32) material was provided by Pierre Gibart at CNRS. This was grown by MOVPE on semi-insulating GaAs substrates.

Arsenic (As) powder (purchased from Alfa, 325 mesh = 45 μm, 99.9999% pure) was used to provide an overpressure during some of the diffusion experiments. To obtain the appropriate overpressure, a certain amount of As is weighed out to provide a pressure according to the ideal gas law: $PV=nRT=wRT/MW_{As}$. Here, w is the weight of elemental As, MW_{As}=74.92 g/mol, R=82.06 cm^3/atm-mol, V=volume of the ampoule, T is in degrees Kelvin. Assuming that the As vapor exists as all As_4 then the equation used is $P_{As4}V=1/4(w_{As}RT/MW_{As})$.

The natural Sn [^{nat}Sn, 8.6 % ^{119}Sn abundance] (99.998%) in the Sn metal source and evaporated film source diffusion runs was purchased from JMC Puratronics. For the $SnCl_2$ solution plating method the Sn^{nat} (99.9999%) was obtained from A.D. Makay, Inc.

The fused silica tubing (19x17 mm and 14x16 mm [O.D. x I.D.]) used in producing the ampoules was purchased from Wale apparatus, Inc. and Desert Glassworks, Inc.

In the ^{nat}Sn diffusion runs three different methods of producing the Sn source were investigated. The first was inserting a solid piece of Sn foil (3.0x3.0x0.1 mm^3) into the ampoule along with the sample plus any As powder. The second method was to thermally evaporate some of the Sn foil on either GaAs or fused silica plates. The Sn film (approximately 200 nm measured via thickness monitor) was then placed in contact with the $Al_{0.32}Ga_{0.68}As$ sample in a sandwich configuration (proximity cap method) and kept this way during the thermal diffusion. The different sandwich configurations are shown in Figure 3.1.

In addition to the thermal evaporation of Sn, the plating of Sn from a $SnCl_2$+2NaOH solution onto n-type GaAs:Si was used. The sandwich configuration for this is shown in the Figure 3.1 b. The plating method stemmed from the fact that a ^{119m}Sn metal diffusion source may be required and that this is readily available only in a $^{119m}SnCl_2$ solution form. The apparatus used in plating Sn onto conducting GaAs:Si consisted of a positively biased graphite electrode with respect to the GaAs:Si piece. Both were immersed in a small beaker containing the $SnCl_2$+2NaOH solution. The use of NaOH in the electrolyte solution helped alleviate the problem of non-uniform plating on the GaAs and provided better adhesion (Eriksson et al 1992). The solution was prepared from a measured amount of solid ^{nat}Sn dissolved in hot HCl (37%), which is then evaporated to leave a white powder ($SnCl_2$). A measured amount of NaOH was added to provide a solution of ions with the ratio Sn^{2+}:$2Na^{+}$. A portion of this concentrated solution was then diluted with deionized water. This was used as the plating electrolyte.

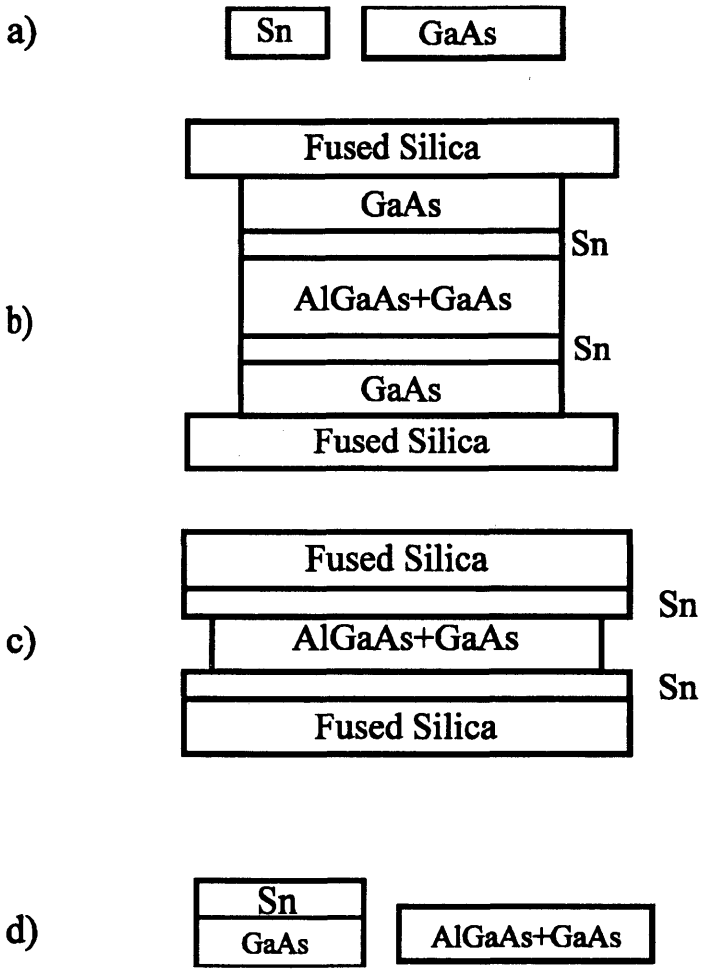

Figure 3.1 The different sandwich arrangements used in the thermal diffusion of Sn from an evaporated Sn metal source (or plated source). The samples labeled as AlGaAs+GaAs were GaAs substrates with a layer of MOVPE-grown AlGaAs in contact with the Sn. The GaAs pieces are replaced with GaAs:Si plated with Sn in the plated source method (b). Silica wool was placed inside the ampoule, against the fused silica plates, to provide mechanical stability during handling.

During plating the solution was kept at room temperature and agitated with a magnetic stirrer and provided uniform plating. Two methods were used to estimate the amount of Sn plated on the GaAs: 1) Faraday's law of electrolysis and 2) weighing the sample before and after plating using an analytical balance (±0.1 mg). Faraday's law of electrolysis is given as $x=(MW)_{Sn}/[zF\rho A]\int I\, dt$, where $(MW)_{Sn}$ is the molecular weight of Sn, z= charge transfer per molecule (+2 in the case of Sn), F=Faraday constant=96485.3 C/mol, ρ=density of Sn (7.3 g/cm^3), A=area of plating, I=electric current in the electrolyte, dt=change in time, x=thickness of plated region. To obtain the amount of current due to the Sn^{2+} ions, the total current is divided by 2 due to the presence of the $2Na^+$ ions (this assumes that the electrolyte solution is concentrated enough such that there is a negligible change in the Sn^{2+}:$2Na^+$ ratio). Using a constant current eliminates the integral. Inserting values specific to Sn, the relation simplifies to $x=8.52x10^{-5}It/A$ (x in cm, I in amps, t in sec, A in cm^2). This can be converted to the weight of Sn plated by $m=\rho xA$.

3.2.2 Closed environment diffusion technique

The technique of evacuated and sealed fused silica ampoules has been adopted from the literature (as described in section 2.1) and applied in previous studies at CSM (Williamson 1986) as well as this thesis. Inner and outer fused silica tubing were used to provide a well-defined volume in which the sample resided. This is shown in Figure 3.2. The tubing was cut to required lengths with an aluminum oxide cutting wheel,

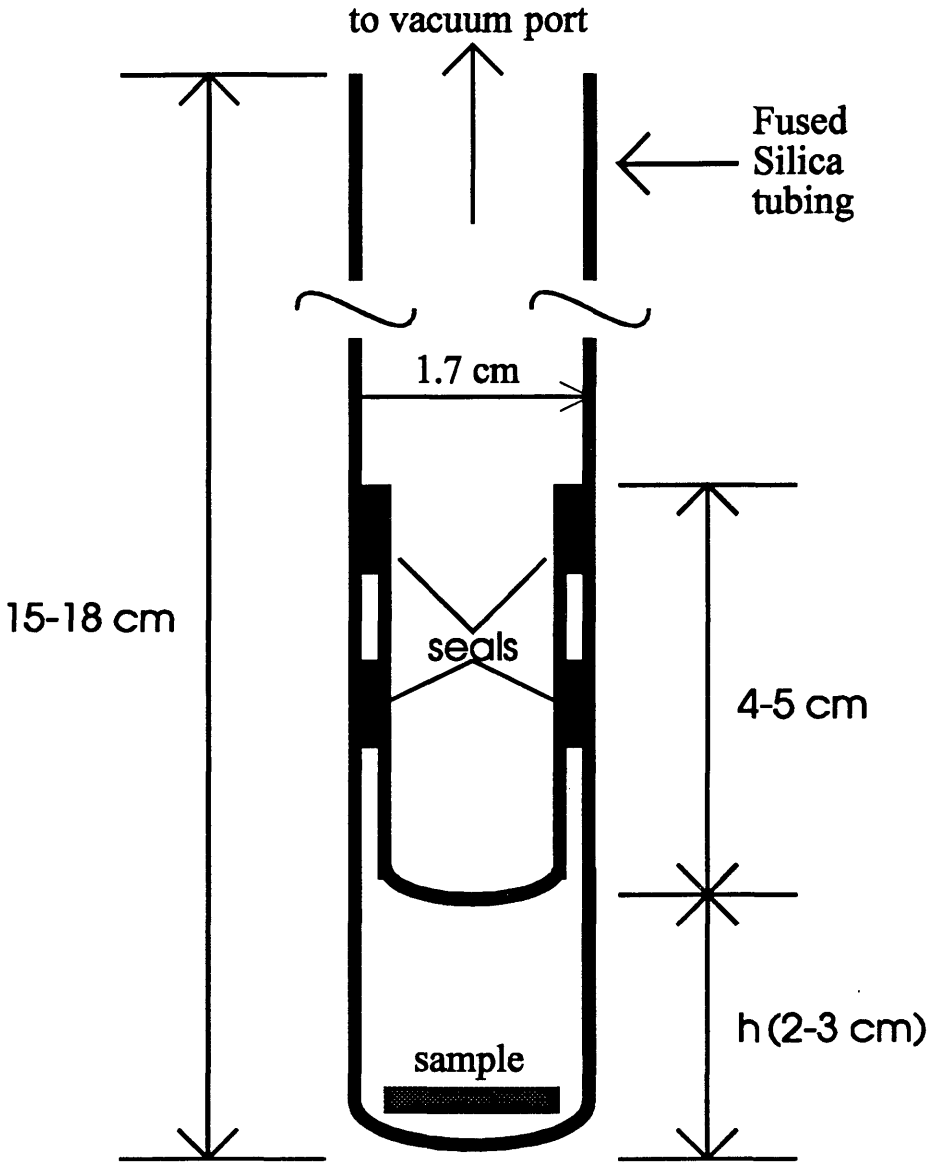

Figure 3.2 Diagram of the fused silica ampoule design used in the thermal diffusion studies. The ampoules were positioned horizontally during the diffusions.

cleaned with soap and water, rinsed with deionized water, then dried with kim-wipes. All sealing and glass lathe operations were done with an oxygen-hydrogen flame (T_{mp}(fused silica)=1610°C). One end of each tube was sealed by rotating it in the lathe (~ 60 rpm) and applying a constant flame in a 1 cm wide region from the end. When the fused silica was sufficiently soft (flame still applied) a fused silica rod was used to "grab and pull" a soft edge axially away from the tube until a closure was made using the rotation of the lathe. This technique required some practice. Upon cooling the tubes, the sample was then inserted into the larger tube and the inner tube was placed within to provide the desired volume. This was then placed back onto the lathe (not rotating) to hold it horizontally while a tack was made. This tack secured the inner tube to the outer one by pushing the inner tube against the outer tube with a fused silica rod while applying the flame where the contact was made. The flame was removed when the two walls fused together (seen by a decrease in the intensity of the softened region). The tack was made far enough away so that the sample was not affected by the heat. Upon cooling of the tack, the ampoule was then inserted into the vacuum system. The first vacuum seal was made by applying the flame at the tack and allowing the vacuum to collapse the outer tube against the inner one and to be fused together. This was followed around the circumference of the tube. This seal was cooled with water so that the sample and the o-ring seal on the vacuum port did not overheat. The second vacuum seal was made at the upper edge of the inner tube, using care that the flame did not remain in one position for a long period of time since the outer seal could collapse excessively into the vacuum

and produce a large leak. After cooling a visual inspection of the seals were made to insure complete closure. Two vacuum systems were used for evacuating the ampoules. Early experiments used a diffusion pump-based system, the later ones a turbo pump system. Both systems were able to pump down to the mid 10^{-6} Torr range, at which pressure the seals were made. The pressure did rise slightly during the sealing process due to the outgassing of the fused silica (possibly oxygen desorption). Because of the low thermal expansion coefficient and thermal conductivity of fused silica, quenching the hot seals with water was possible without any local mechanical stresses induced and assures that the sample will not be affected by the heat of the torch if the seals are sufficiently far away (> 3 cm), respectively. The samples were removed by using a hammer and steel punch to break the end of the ampoule in a controlled manner while the other end was butted against a rigid support. Only a slight amount of force was usually required to accomplish this.

The thermal diffusions were carried out in a programmable 3-zone tube furnace purchased from Mellen Co., Inc. It is capable of temperatures as high as 1500°C and provides a flat temperature zone (±1°C, T≥400°C) of approximately 20 cm in length. The overall length of the furnace is 36" (91.4 cm) with a 2" diameter (5.08 cm) bore-hole. Within the bore-hole is a mullite tube in which an alumina "D"-tube is inserted on which the sealed ampoules rest. Including the 3 type-R thermocouples (Pt-13%Pt+Rh), which measure the temperature of the brick-work surrounding the bore-hole, is a 36" long type-R thermocouple, enclosed in an alumina sheath, used to calibrate and measure temperatures

inside the mullite tube (also used to monitor the ampoule temperature). This thermocouple was also used to insert and remove the ampoules from the furnace. The calibration equation, determined from the temperatures according to the zone-2 controller and the actual temperature, was determined to be $T_{Z2}=1.00732T_{mullite}-15.9089$, for $T_{mullite}> 200°C$.

3.2.3 Silicon oxide and silicon nitride capping layers

As was mentioned in section 2.1, the use of capping layers such as SiO_2 and Si_3N_4 can provide added protection against decomposition (e.g. As evaporation) of the AlGaAs layer during high temperature heat treatments. It has been suggested that treating the GaAs or $Al_xGa_{1-x}As$ surface before capping layer deposition may improve the activation efficiency of ion implanted dopants. This has been investigated by Cho et al (1992) on Si-implanted GaAs (using a dose of $1.5x10^{13}$ cm^{-2} at 60 keV then $3.5x10^{12}$ cm^{-2} at 380 keV). They have found that the air-grown native oxide layer on GaAs, approximately 1.5 -3 nm thick, contains carbon contamination, which is an acceptor dopant. It was not stated what was the origin of the carbon (possibly from the adsorption and dissociation of CO_2 on the GaAs surface). The surface oxides which can form are Ga_2O_3, As_2O_3, As_2O_5, and $GaAsO_4$ (Thurmond et al 1980). Cho et al have tried six different surface treatments prior to a 75 nm PECVD Si_3N_4 cappping layer deposition: no treatment, (1:10) $NH_4OH:H_2O$ for 60 s, O_2 (oxygen) plasma-NH_4OH, (1:10) $HCl:H_2O$ for 60 s, O_2 plasma, and (1:10) $NH_4OH:H_2O$ then O_2 plasma. The O_2 plasma treatments were in a

commercially built asher unit with 100 W RF power under 500 mT of O_2 with a temperature of 100°C for 5 minutes. Using ellipsometry and angle resolved photoelectron spectroscopy to determine the oxide thickness and x-ray photoelectron spectroscopy to determine its composition they have found that the O_2 plasma treated samples had an oxide thickness of 2.5 nm with no carbon contamination with a composition of Ga_2O_3, As_2O_3, As_2O_5, As, while the NH_4OH treated samples had a thinner oxide (1 nm) with a composition of Ga_2O_3, As_2O_3, As, and C. Ohmic-contact-resistance investigations showed that the GaAs was well behaved for several samples treated with the O_2 plasma (0.08± 0.03 Ω-mm) while the NH_4OH treated ones varied from 0 to 0.2 Ω-mm. This was attributed to less residue found on the GaAs surface after O_2 plasma treatment. The oxides are important for the activation of the implanted Si in GaAs. The As oxides are unstable with the presence of GaAs and decompose according to the reaction As_2O_3+ $2GaAs \rightarrow Ga_2O_3 + 4As$. With elemental As confined at the Si_3N_4-GaAs interface there is increased probability of the implanted Si being incorporated onto a group-III (Ga) site via $V_{Ga}+Si \rightarrow Si_{Ga}$. Activation efficiencies of 22.5 and 30.5% were found for the (1:10) $NH_4OH:H_2O$ and O_2 plasma treatments, respectively, to a depth of < 0.2 μm in GaAs. Cho et al have concluded from this work that O_2 plasma treatment of GaAs prior to Si_3N_4 capping improves the activation efficiency of implanted Si, removing the carbon contamination, and improving the ohmic contact resistance.

The work by Cho et al has been applied to this study using RF sputtered silicon nitride and silicon oxide capping layers. Two treatments have been investigated: (1:10

$NH_4OH:H_2O$ for 2 min in ultrasound and O_2 plasma. The silicon oxide depositions and the O_2 plasma generation were conducted in a diffusion-pumped vacuum system while the silicon nitride depositions used a turbo pumped system, both using a 2" clamped-target RF magnetron. The Si targets used were 99.999% pure, purchased from Cerac Inc. and the sputtering gases were at least 99.995% pure (Ar, O_2, N_2). A stainless steel cylindrical electrode (approximately 6 cm tall and 1 cm in diameter), which replaced a target in the magnetron, was constructed to prevent the O_2 plasma from being concentrated on the target surface region by the static magnetic field in the magnetron and allowing it to create a denser plasma near the sample (15 cm above target plane). The sample was clamped in a rotating holder which was held at ground potential. The plasma conditions were 50 mTorr of O_2, with an RF power of 100 W for a time of 10 minutes. The capping layer sputtering conditions are given in Table 3.2. The silicon nitride sputtering parameters were taken from Carriere et al (1990) who used an $Ar:N_2$ ratio of 1:1 and 300 K (or ambient) substrate temperature. The film thicknesses were measured via step-edge profilometry.

3.2.4. X-ray diffraction

The x-ray diffraction data obtained from the samples in this study were useful in identifying extraneous phases that were present after annealing. The system used was manufactured by Rigaku with a computer controlled $2\Theta/\Theta$ diffractometer using a Cu K_α x-ray source (λ=0.15405 nm). The samples were mounted on a glass slide with double-

stick tape. The glass produces an amorphous peak in the data at $2\Theta \approx 17.4$ degrees.

3.2.5 Dopant depth profiling

To profile the capping layers and diffused Sn in the III-V alloys versus depth, three techniques (conducted at NREL) were investigated: SIMS, AES, and CV. SIMS and AES

Table 3.3. RF sputtering conditions for the silicon nitride and silicon oxide capping layers on $Al_xGa_{1-x}As$. The samples were rotated to provide a capping layer on both sides.

PARAMETER	SILICON OXIDE	SILICON NITRIDE
P_{BASE} (Torr)	6×10^{-5}	2×10^{-6}
P_{Ar} (mTorr)	3.0	3.0
PO_2 / PN_2 (mTorr)	1.0 / 0.0	0.0 / 3.0
RF POWER (W)	50	100
THICKNESS (nm)	~120	~120
SUBSTRATE TEMPERATURE	Ambient	Ambient
SUBSTRATE-TARGET DISTANCE (cm)	15	15
DEPOSITION TIME (min)	100	60

can be used for measuring the total concentration of a dopant (electrically active and inactive). SIMS possesses a higher sensitivity compared to AES (~ 1 atomic %). Both

techniques require the sputter removal of material (using a Cs^+ ion beam for SIMS and Ar^+ for AES). C-V is useful for profiling the electrically active dopant species in a sample via electrochemically etching the sample in an electrolyte (e.g. NaOH) as the capacitance and voltage are recorded (Blood 1986).

3.2.6 Ohmic contact formation

To obtain the electronic transport properties of the non-radioactive Sn-doped samples, ohmic contacts need to be formed on the doped samples. For square or rectangular samples the contact geometry should be such that they are placed as close as possible to the corners (or edges) of the sample and that they are as small as possible. These requirements insure accurate Hall effect measurements (Creek 1992).

The contact material used was In-2% Sn. The approximate dimensions of the contacts were 1mm x 1mm x 200 μm. These were pressed into the sample corners to break through any oxide layer and allow alloying. The samples were then placed on a Kanthal heating strip situated in a small mechanically pumped bell jar vacuum system. The system was first pumped down to approximately 30 mTorr and then back-filled to 100 mTorr with N_2-5% H_2 forming gas. A high current power supply was used to heat the stage to a temperature of approximately 450°C (measured with a type-J thermocouple mechanically attached to the heater) for 5 minutes. The current was then shut off allowing a maximum cooling rate to be achieved under 100 mTorr of forming gas. Fine gold or #40 copper wire was then carefully soldered to the contacts. Resistance versus

temperature measurements in the light and dark were done in the same cryostat used for the low temperature Mössbauer measurements.

3.3 Results

3.3.1 Thermally diffused Sn samples

XRD, SIMS, and electrochemical C-V measurements were used to characterize thermally diffused Sn into $Al_{0.32}Ga_{0.68}As$. Table 3.4 summarizes the measurements used and their corresponding figures.

A carrier profile via C-V proved difficult because of the uneven etching produced by the apparatus due to the apparent presence of dislocations and pits in the samples. The carrier concentrations given are for the near-surface region of the samples (before any substantial amount of etching has started). The surface roughness after etching was approximately $\pm$ 20 μm. According to the XRD data, for samples annealed with respect to geometries B, C, and D1, decomposition in the possible forms of Sn_xAs_y, SnO_y, As_xO_y, Ga_xO_y, and SiO_2 were discovered on the various surfaces involved during the anneals (shown by the XRD peaks not labeled as the III-V (200) and (400) peaks or otherwise labeled). In the case of geometries C and D2, a large amount of a white deposit was found on the AlGaAs surface. XRD analysis on this material alone showed it was SiO_2. The possible sources for this was from the ampoule itself or less likely from the out-diffusion of Si from the GaAs:Si+Sn plating material combining with any oxygen

Table 3.4 Summary of the parameters used in the Sn diffusion study.

Geometry From Figure 3.1	Temp. (°C)	Time (hrs)	PAs_4 (atm)	XRD	SIMS	n_{CV} (cm^{-3}) surface
A	800	12	0.5	-	-	$7x10^{18}$
B	1000	12	1.0	Fig. 3.3	-	-
C	1000	12	0.5	-	Fig. 3.6	-
D1	1000	12	2.0	Fig 3.4	-	-
D2	1000	21 (FC)*	1.0	-	-	-
D3	1000	21 (FC)*	ambient	Fig. 3.5	Fig. 3.7	$8x10^{17}$

* FC=furnace cooled, otherwise removed from furnace at the temperature given.

inside the ampoule. This oxygen may have desorbed from the ampoule itself when using temperatures at 1000°C. However, in the case of geometry D3, using the ambient As_4 vapor developed from the III-V surfaces and a slow furnace cool-down caused very little or no surface decomposition, keeping the surfaces specular. Figure 3.5(b) shows the GaAs:Si+Sn plating peaks with β-Sn (metallic) and no oxide peaks. It is possible that the introduction of the fine As powder (~5 μm size) into the ampoule may also introduce As oxides due to the O_2 absorption of the powder. Larger pieces of metallic As may alleviate this problem. It is not known if this will reduce the roughness that it may cause to the sample surface if it is not in the sandwich geometry (which kept the surfaces

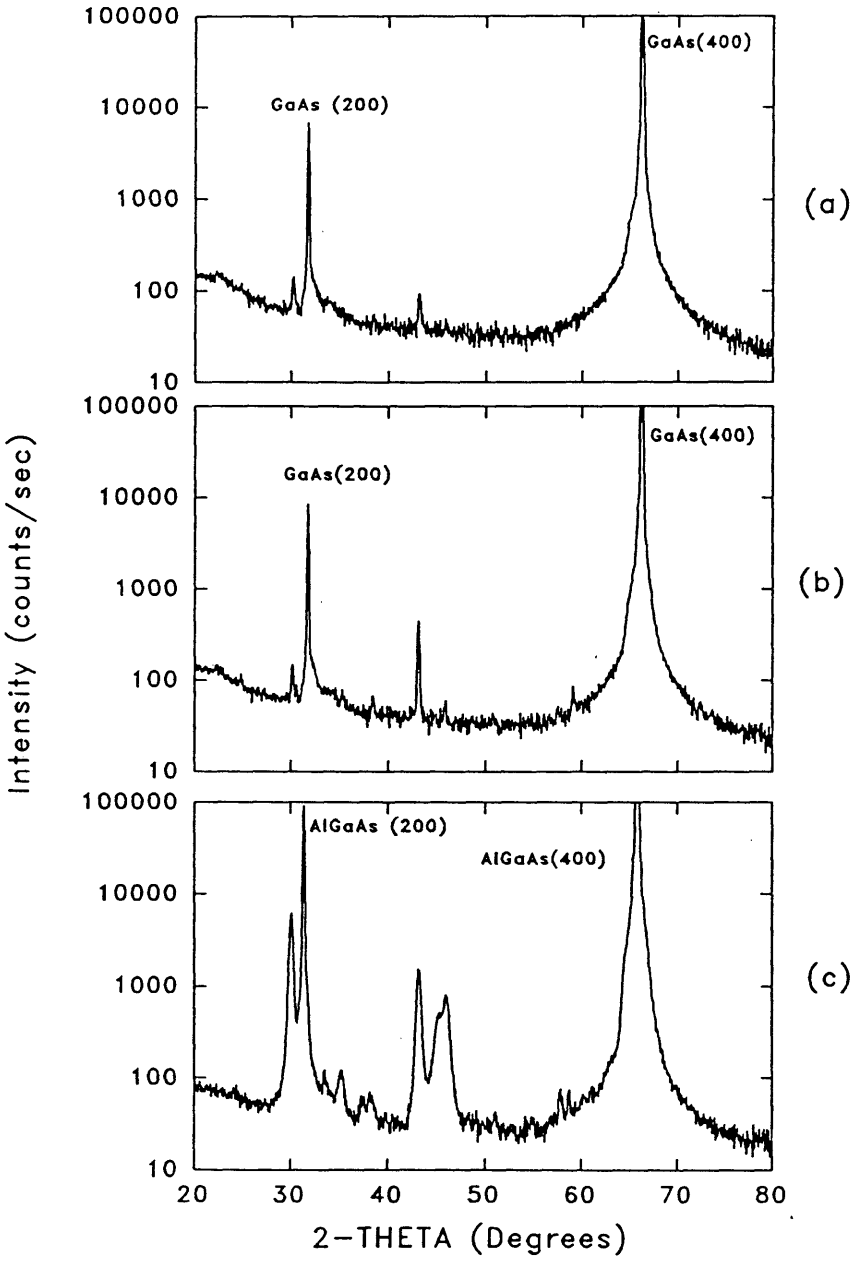

Figure 3.3 XRD data for geometry B: (a) GaAs:Si+Sn plating in contact with AlGaAs, (b) GaAs:Si+Sn in contact with SiO_2 plate, (c) AlGaAs surface.

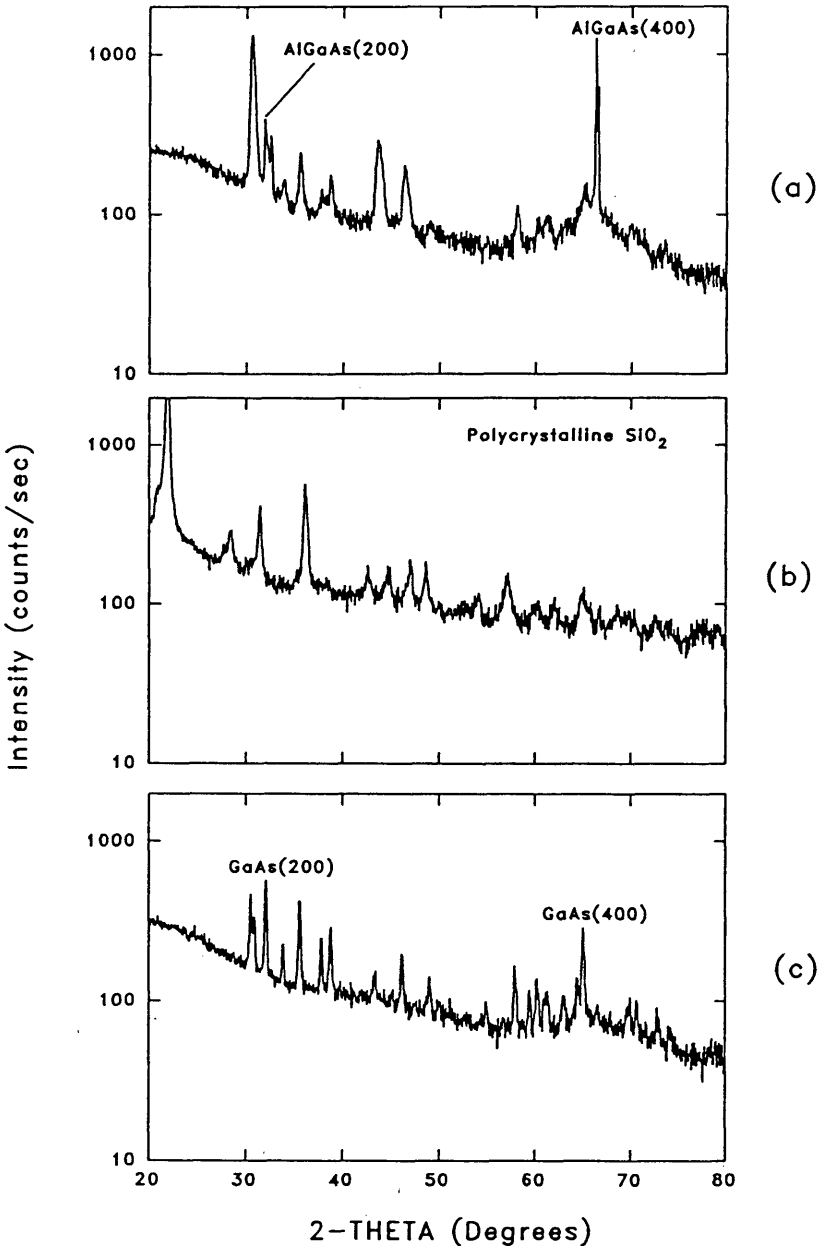

Figure 3.4 XRD data for geometry D1: (a) AlGaAs with white deposit, (b) white deposit only (SiO_2), (c) GaAs:Si+Sn surface.

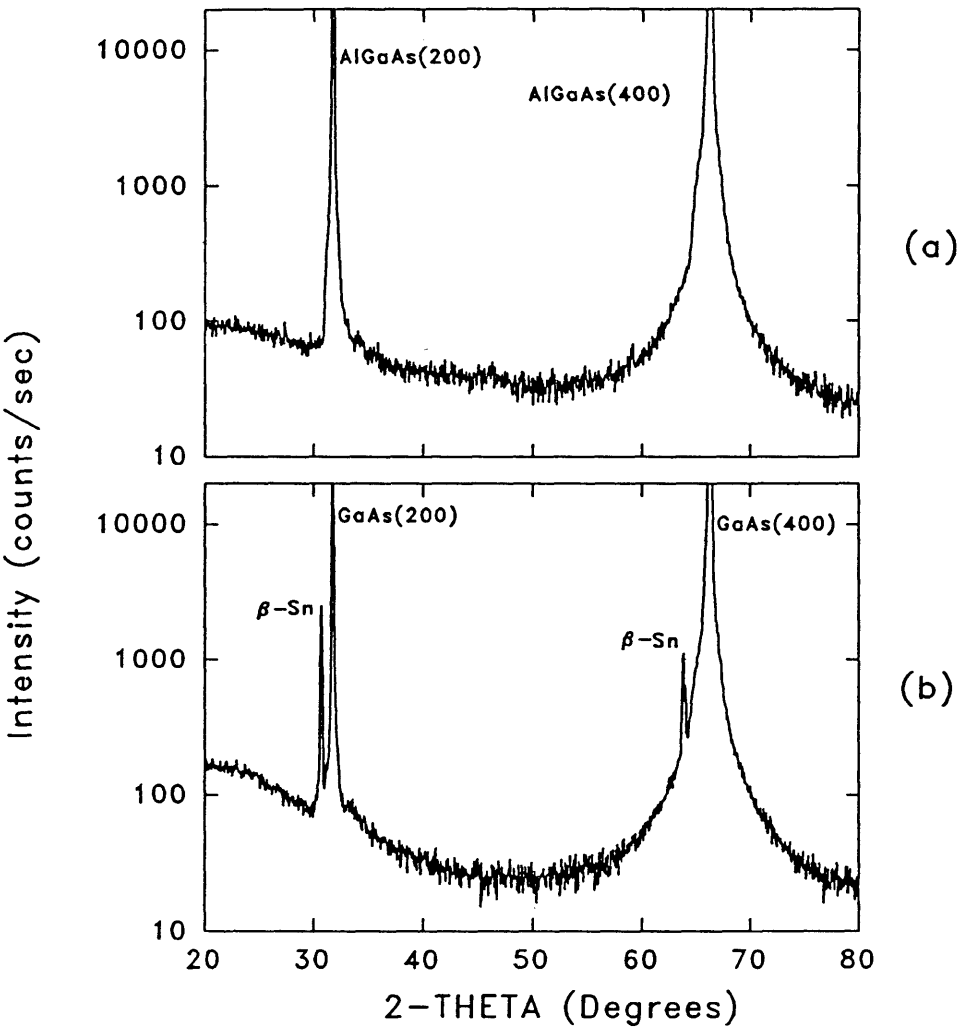

Figure 3.5 XRD data for geometry D3: (a) AlGaAs surface, (b) GaAs:Si+Sn surface showing β-Sn peaks.

somewhat specular, but discolored). The same discoloration was found for geometry D3 but XRD shows no peaks other than those for AlGaAs. To preserve the physical surface characteristics the whole system (ampoule+sample) should be kept in thermal equilibrium when cooling an exposed III-V surface (i.e. slow furnace cooling) to minimize surface roughness, since the volatile As_4 vapor from the sample will condense on the ampoule walls which are cooler ($\leq$ 600 °C). However, possible decomposition of the surface may occur, as shown from the XRD data, when using a large As overpressure, independent of the cooling rate used, such as geometry D2.

The SIMS data (Figures 3.6 and 3.7) show that not only has Sn diffused into the samples, but also Si, C, and O. The Si and O may have evolved from the ampoule walls and/or the SiO_2 sandwiching plates. The carbon was possibly incorporated into the $Al_{0.32}Ga_{0.68}As$ layer during MOVPE growth and/or by adsorption of CO_2/CO on the surface. Si, O and C can cause doping of the semiconductor: Si (n-type on III site), C (p-type on V site), O (p-type on III site). Using the sandwich geometry and $P(As_4)$=0.5 atm (Figure 3.6) the SIMS data shows diffusion of these elements to approximately 10 μm in depth, in contrast to the approximate 0.5 μm depth found using exposed surfaces and $P(As_4)$=ambient (Figure 3.7). This suggests that the use of a large As overpressure $\geq$0.5 atm enhances the diffusion of Sn (as well as Si, C, and O) into the AlGaAs through the assumed creation of and diffusion by column III vacancies (V_{Al} and V_{Ga}) (Tan et al 1991, Goldstein 1960, Goldstein and Keller 1961).

Finally, for geometry D3, comparing the surface concentration of Sn (SIMS) to the

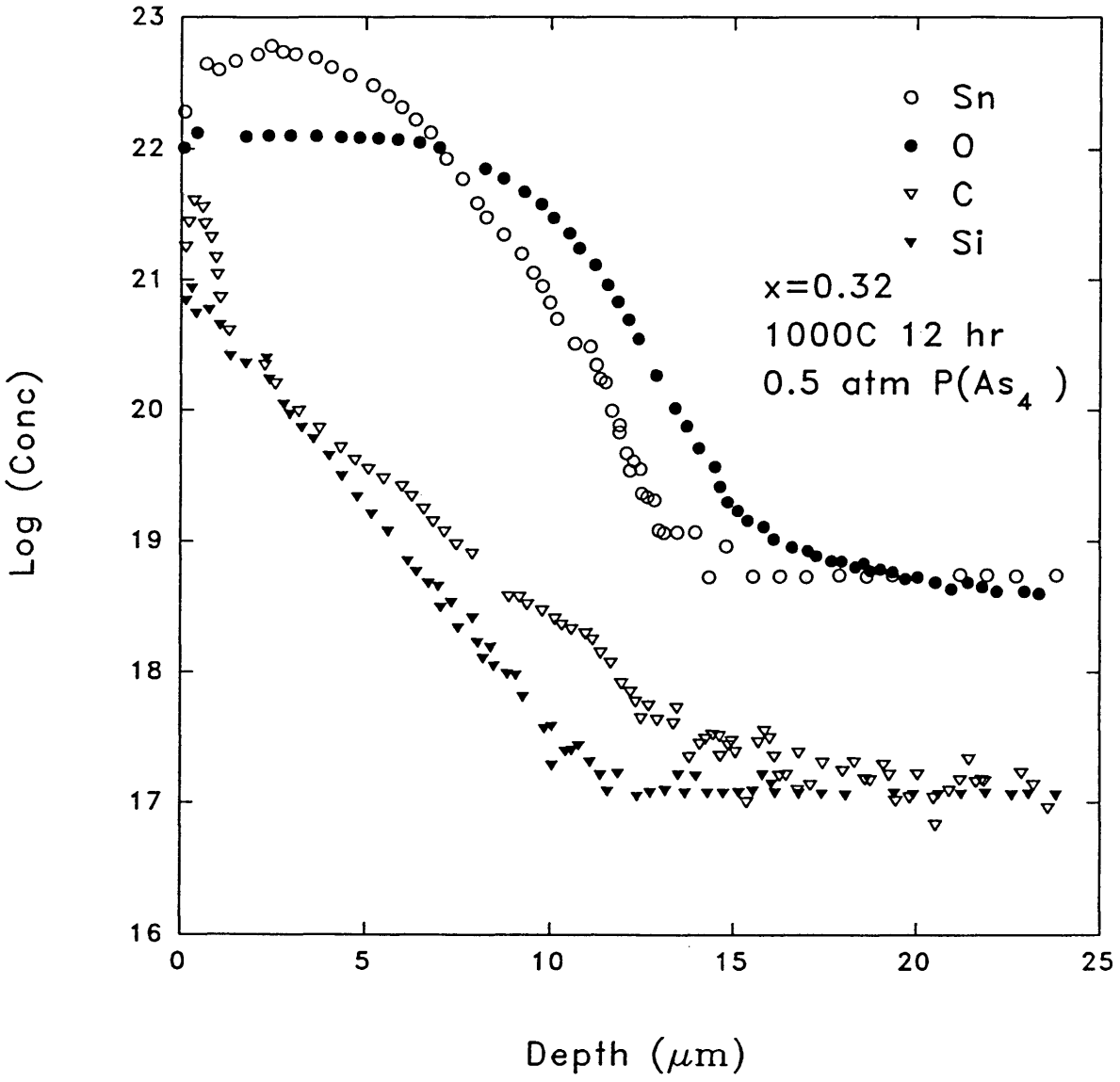

Figure 3.6 SIMS data for geometry C.

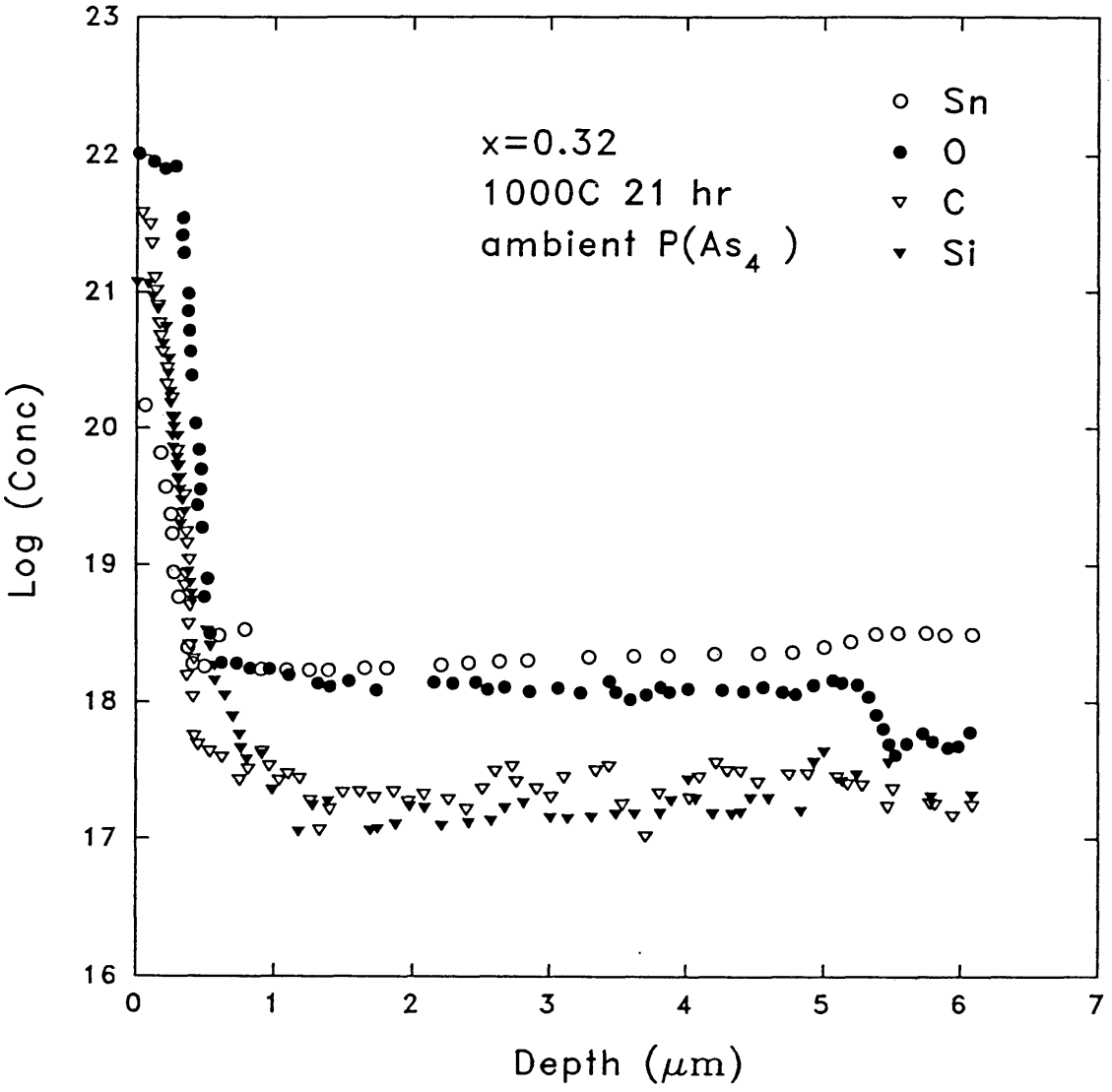

Figure 3.7 SIMS data for geometry D3.

surface carrier concentration (C-V) gives an electrical activation ratio of $n_{C\text{-}V}/N_{Sn}=8x10^{17}$ $cm^{-3}/2x10^{20}$ cm^{-3} =0.004 (0.4% activation). Higher activation is possible (i.e. lower compensation) at deeper depths, however, the CV measurement was not reliable due to non-uniform etching.

3.3.2 SiO_x and Si_xN_y capping layers

SiO_x and Si_xN_y capping layers were investigated to determine a method of reducing decomposition of the AlGaAs during thermal processing. Reactive RF-sputtering of these films using different pre-sputtering treatments was used. The conditions and treatments were discussed earlier (sec. 3.2.3).

X-ray diffraction (CSM) and AES profiling (NREL) were used to characterize the sputtered films. Differences due to the different pre-anneal treatments could not be observed in these measurements. Representative data from this study are shown in Figures 3.8 - 3.10. Figure 3.8(a,b) shows the XRD results for the SiO_x film deposited on $Al_{0.32}Ga_{0.68}As$, subjected to the O_2 plasma treatment. In both the pre- and post-anneal (850°C, 12 hrs) cases, the films are amorphous (broad peak at ~ 2θ=17°). This peak may also contain the effect of the glass slide on which the samples were mounted. The only other peaks present are due to the AlGaAs substrate ($2\theta_{200}$~32°, $2\theta_{400}$~66.3°). The same effect was observed for the Si_xN_y films which were not subjected to any pre-anneal treatment (Figure 3.8(c,d)). The lack of extraneous peaks suggests that decomposition of the sample surface has been minimized, independent of the cooling rate or lack of thermal

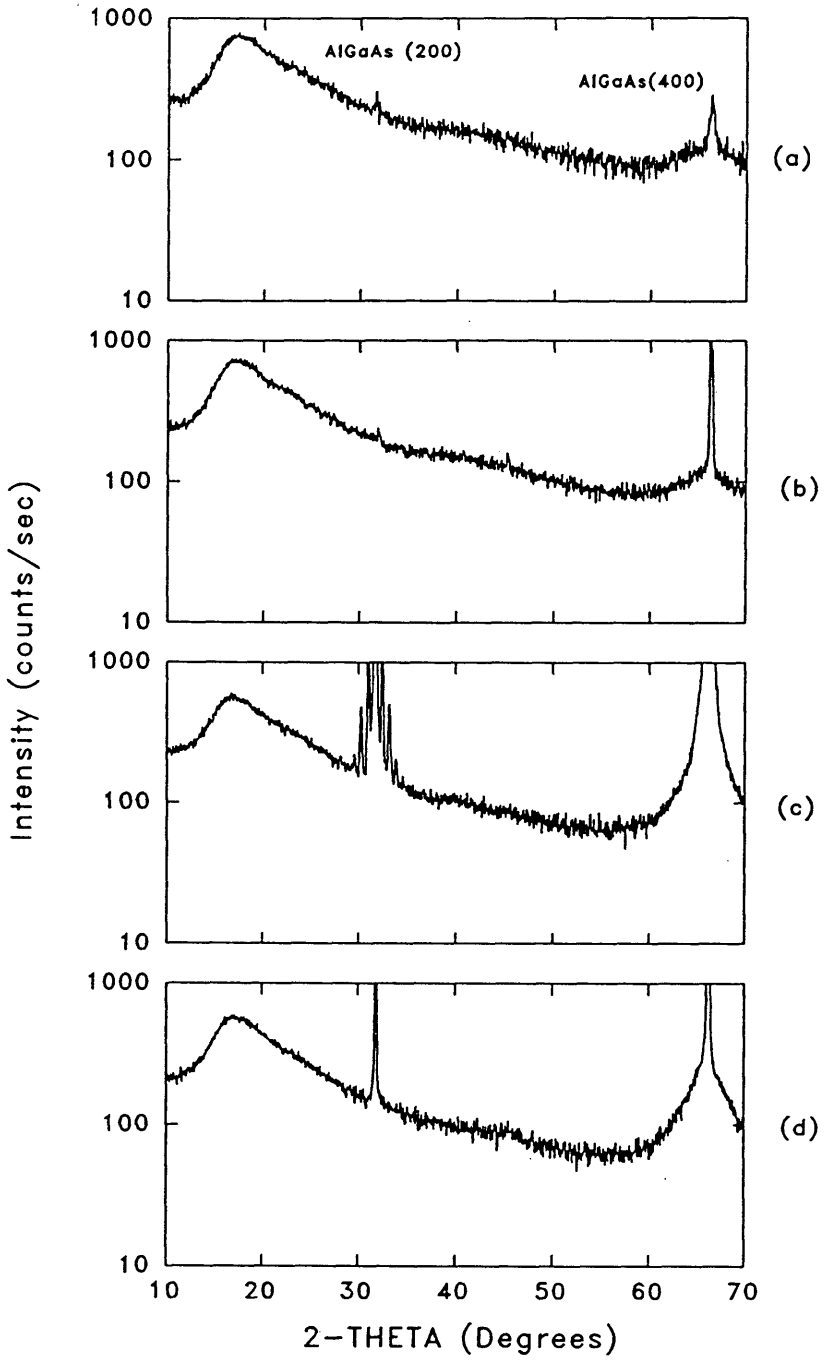

Figure 3.8 XRD results for the SiO_x capping layer (a) pre-anneal, (b) post-anneal; and the Si_xN_y capping layer (c) pre-anneal, (d) post-anneal.

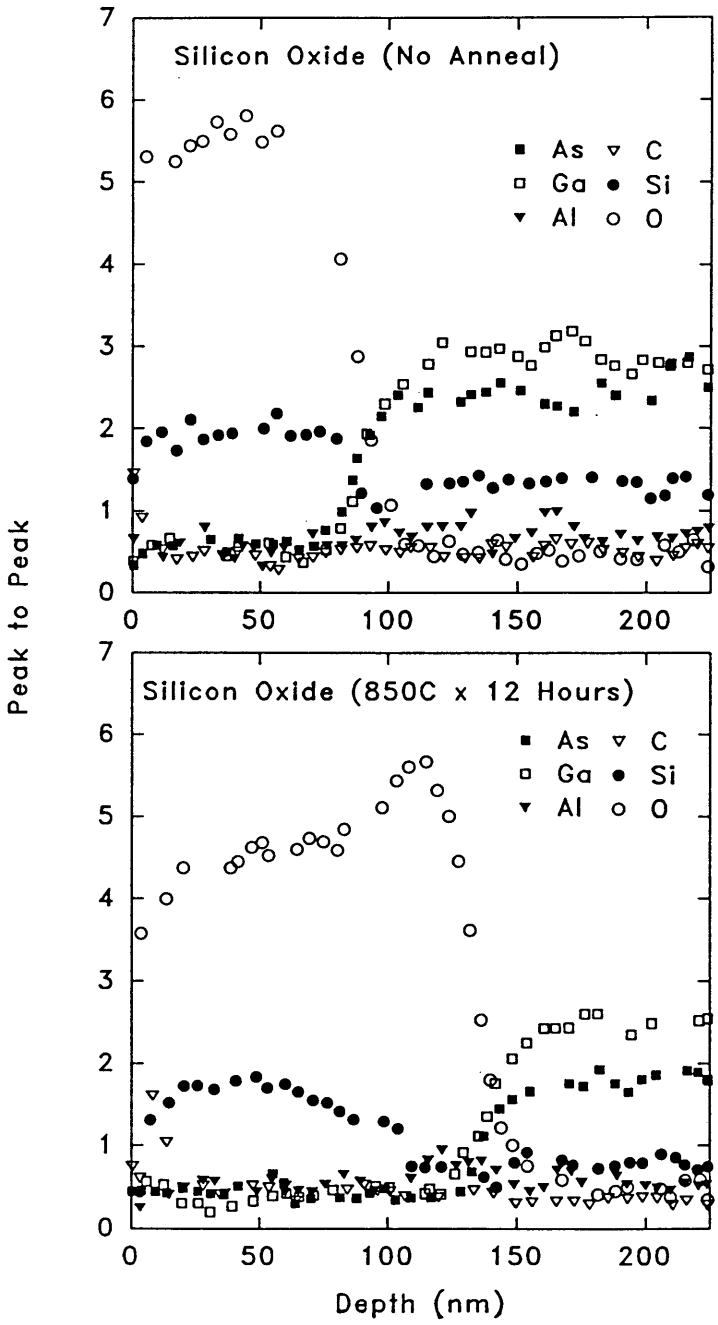

Figure 3.9 AES depth profiling data for the SiO_x capping layer: (a) pre-anneal, (b) post-anneal.

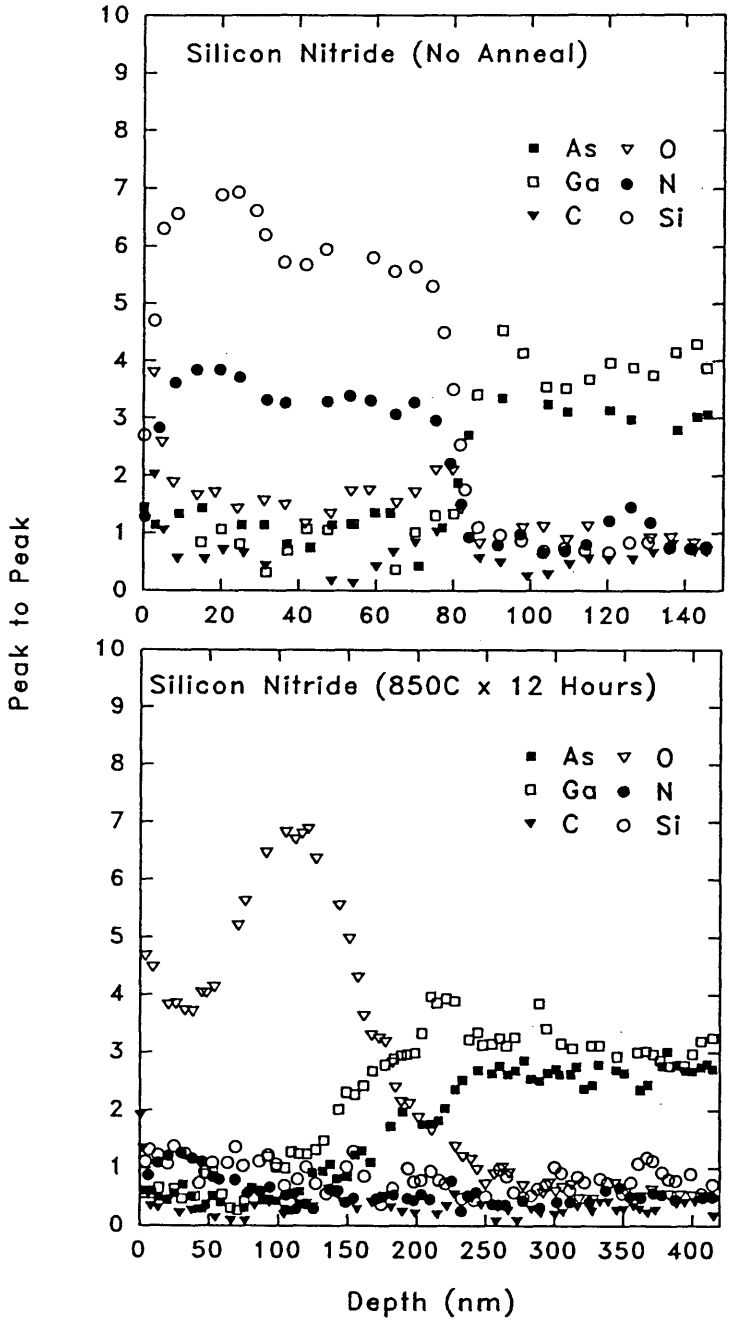

Figure 3.10 AES depth profiling data for the Si_xN_y capping layer: (a) pre-anneal, (b) post-anneal.

equilibrium in the ampoule. This is in contrast to what was observed in the XRD data from non-capped layers described in sec. 3.3.1.

Changes in the AlGaAs (h00) intensities between Figure 3.8(a) and (b) was attributed to alignment of the sample while the satellite peaks about the (200) reflection was attributed to a superlattice present in the sample. This was verified by small angle XRD (2Θ=1 to 10°). The first order and higher order peaks were found to be separated by $\Delta 2\Theta \sim$ 0.7°. The d-spacing of the superlattice can be written as $\sim\lambda(\Delta n)/2(\Delta\Theta)$ (small angle approximation). For Δn (difference in the reflection order) =1 and $\Delta\Theta$=0.35° (0.0061 rad) and λ=1.5405 Å (Cu Kα) gave d=126 Å. The absence of superlattice peaks in Figure 3.8(d) {Si_xN_y post-anneal) was attributed to annealing-induced disorder. The superlattice may have been unintentionally produced during MOVPE growth, possibly via a periodic fluctuation in the stoichiometry versus time.

The AES data in Figures 3.9 and 3.10 show the depth profiles for SiO_x and Si_xN_y capping layers before and after an 850°C, 12 h anneal. For SiO_x the composition and profile remain relatively constant. Using the sensitivity factors obtained from Auger data tables (Davis et al 1976), a rough estimate of the composition can be determined. For SiO_x the stoichiometry is $SiO_{2.0}$ (pre-anneal), $SiO_{2.1}$ (post-anneal); for Si_xN_y the average stoichiometry is $SiN_{4.8}O$ (pre-anneal), $SiN_{0.73}O_{6.7}$ (post-anneal). It seems that oxygen has entered into the nitride film, possibly due to the fact that the film had decomposed after annealing (the film lifted off the substrate). On the other hand, the SiO_2 films remained stoichiometric and undecomposed (well-adhered to the substrate). Therefore,

SiO_2 was selected as a capping layer to prevent $Al_xGa_{1-x}As$ decomposition.

4. Mössbauer Study of Sn in $Al_xGa_{1-x}As$

4.1 Introduction

Mössbauer spectroscopy has proven useful for probing the local environment of particular atoms which exhibit resonant transmission and absorption of gamma rays having extremely narrow energy widths such as $2.6x10^{-8}$, $4.7x10^{-9}$ and $2.7x10^{-8}$ eV for ^{119}Sn, ^{57}Fe and ^{129}I, respectively. The electronic, geometric and magnetic structure of solids can be deduced from the electric monopole (isomer shift, δ), electric quadrupole (having an energy splitting of Δ), and magnetic dipole hyperfine interactions. Mössbauer spectroscopy is also useful in probing the lattice dynamics of a sample from recoilless fraction. That is, given that the recoilless fraction, f, is defined as $\exp(-k_o^2\langle x^2\rangle)$, where k_o is the wavevector of the Mössbauer gamma ray and $\langle x^2\rangle$ is the mean square displacement of the Mössbauer atom along the photon direction. Using the Debye model for solids $\langle x^2\rangle$ can be rewritten as $3\hbar^2/Mk\Theta_D[0.25+(T/\Theta_D)^2\int x\, dx/(e^x-1)]$ where M is the mass of the atom, Θ_D is the Debye temperature of a given site defined by $\langle x^2\rangle$, T is the measurement temperature, k is Boltzmann's constant, $\hbar$ is Planck's constant and the integral limits are 0 to Θ_D/T. Note that $\langle x^2\rangle$ may not have the same value in all directions, hence resulting in different Debye temperatures depending on the direction of the gamma ray. Further information regarding the details of Mössbauer spectroscopy and its applications to semiconductors can be found elsewhere (Williamson et al 1992).

This work focuses on two of the above effects: the isomer shift and the quadrupole

hyperfine interaction. The isomer shift (δ) is proportional to the difference in the total electron density at the Mössbauer-active nucleus in the source, $\rho_s(0)$, and in the absorber, $\rho_a(0)$, by $\delta=\alpha_o[\rho_a(0)-\rho_s(0)]$, where the proportionality constant can be positive or negative and depends on nuclear parameters that can only be predicted by experimental measurement of δ coupled with theoretical values of $\rho(0)$ for two or more solids. A sign change is involved when a source experiment is conducted relative to an absorber experiment and vice versa. The quadrupole splitting occurs if the Mössbauer atom resides on a crystallographic site having a symmetry less than cubic, which causes an electric field gradient (EFG) at the nucleus. For the case of ^{119}Sn, where the nuclear excited spin states are $\pm 3/2$ and ground states are $\pm 1/2$, Δ, in velocity units, is given by $\Delta=[ceQV_{zz}/2E_o](1+\eta/3)^{1/2}$ where c is the speed of light, e is the electron charge, E_o is the Mössbauer γ-ray energy, Q is the nuclear quadrupole moment (= -0.064 barns for ^{119}Sn), and the asymmetry parameter $\eta=(V_{xx}-V_{yy})/V_{zz}$, where V_{ii} are the components of the diagonalized EFG tensor evaluated at the nucleus and $|V_{zz}|\geq|V_{xx}|\geq|V_{yy}|$. For axial symmetry, e.g. tetragonal or trigonal symmetry, $V_{xx}=V_{yy}$ and $\eta=0$. In general the intensities of the quadrupole split peaks may not be equal. This is due to an angular difference, θ, between the incident γ-ray direction and the quantization axis in the sample. The ratio of the peak intensities, R, for ^{119}Sn and $\eta=0$ is $R=[1+\cos^2\theta]/[2/3+\sin^2\theta]$. R varies from 3 to 3/5 as θ varies from 0 to $\pi/2$. R=1 at $\theta=54.73°$ and when averaged over the entire solid angle of the γ-rays (Williamson and Gibart 1989).

Useful information can be obtained from the calculated fractional areas (area of a particular spectral component / total area) of the Mössbauer spectrum: the fraction of Mössbauer atoms on a given lattice site (proportional to the fractional area) for a given temperature; the recoilless fraction ratio (and a Debye temperature) for a given site determined by the fractional area ratio ($A1(T_1)/A2(T_2)$) where A1 and A2 are the fractional areas and T_1 and T_2 are temperatures; in the case of the Sn DX center the change in the fractional area between the light and the dark (PPC) would relate to the fraction of the total Sn in the sample undergoing this effect. Table 4.1 below lists the Mössbauer parameters of the various Sn sites, that can exist in $Al_xGa_{1-x}As$ as found in the literature.

Table 4.1. A list of lattice sites and their associated Debye temperatures, recoilless fraction ratios (f_{76K}/f_{4K}), isomer shifts, and quadrupole splittings for Sn in GaAs measured by Mössbauer spectroscopy at 76 K relative to $CaSnO_3$ (SnO_2 for the amorphous sites) at 300 K from Williamson and Gibart (1989), Williamson et al (1987), Holm and Weyer (1980) and the references therein. See original papers for methods of defect identification and interpretation.

Defect	Θ_D(K)	f(76K)/f(4K)	δ (mm/s)	Δ (mm/s)
Sn_{Ga}	202(5)	0.84(2)	1.83(3)	0
Sn_{Ga}	175(20)	0.78(9)	1.83(2)	0
Sn_{Ga}	200(10)	0.84(4)	1.80(2)	-
Sn_{As}	200(7)	0.84(3)	1.90(4)	-
$Sn_{Ga}V_{As}$	170(10)	0.76(4)	2.84(15)	0.37(10)
$Sn_{Ga}V_{Ga}$	175(20)	0.77(9)	1.85(5)	~0
Sn-2V	167(1)	0.75(4)	1.34(15)	-
Sn_i	150(20)	0.69(9)	3.41(5)	0
Neutral Sn	180(10)	0.79(4)	2.66(3)	0.65(2)
Neutral Sn	155(15)	0.71(7)	2.7(1)	0.6(1)
α-Sn	161(3)	0.74(1)	2.06(2)	0
β-Sn	134(2)	0.62(2)	2.62(1)	0.3(1)
SnAs	183(5)	0.80(2)	2.58(1)	0
Sn_3As_2	165(5)	0.75(2)	2.79(1)	0.53(2)
Sn DX (0.3<x<0.43)	-	-	2.67(5)	0.6(1)*
Sn DX (x=0, 3.3-4.8 GPa)	-	-	2.60(5)	0.4(1)*
amorphous Sn2V	167(10)	0.76(5)	1.26(15)	0
amorphous Sn_{Ga}	158(10)	0.72(5)	1.76(6)	0
amorphous Sn-V	173(10)	0.78(5)	2.80(15)	0
amorphous Sn_i	141(15)	0.64(7)	3.50(30)	0

*Quadrupole splitting not definitely established since alternate fits of data are possible. Also, neither of these experiments involve PPC studies to confirm DX centers were present

4.2 Nuclear decay after-effects

For Mössbauer source experiments, nuclear decay after-effects, which may be present in the spectrum, should be considered. In a standard source experiment the sample contains parent atoms which decay with a relatively long half-life to the excited state. This decay can influence the spectrum in several ways: nuclear recoil displacing the decaying atom from its original lattice position; the decay can create a disturbance in the electronic shell of the daughter atom, which may give rise to measurable effects in the spectrum. The most violent disturbance occurs if the decay proceeds via electron capture or internal conversion. Both mechanisms cause an inner-shell hole to be created, which is filled by electrons from outer shells through x-ray emission and an Auger process which causes a cascade of events to be triggered, thus leading to the creation of a number of holes in the outer shell of the daughter atom. This mechanism leads to varying charge states of the Mössbauer atom, which, in turn lead to varying isomer shifts. The β-decay process in the parent atom is less violent, however, the sudden change of the nuclear charge from Ze to (Z+1)e can ionize the electronic shell of the daughter atom, creating several charge states. When considering semiconductors, holes in the outer shell of an impurity atom will fill rapidly (within 10^{-12} s) if the energy of this state lies in the valence or conduction band of the host. However, if this state lies within the band gap and has a lifetime longer or comparable to the Mössbauer level lifetime, the spectrum observed may represent the atom in this electronic state (Williamson et al 1992).

In this thesis ^{119m}Sn was used to dope $Al_xGa_{1-x}As$ as a source sample. The parent

atom is designated as ^{119m}Sn, the excited daughter as $^{119}Sn^*$ and the stable daughter ^{119}Sn. Figure 4.1 shows the decay scheme for $^{119}Sn_{50}$. This decay is classified as an isomeric transition (atomic number is conserved). It is important to consider the internal conversion processes that are exhibited in the $^{119m}Sn \rightarrow ^{119}Sn^* \rightarrow ^{119}Sn$. The internal conversion coefficient (ICC) for the $^{119}Sn^* \rightarrow ^{119}Sn$ transition is given as α=5.12. That is one out of 5.12 γ-rays exit the sample without exciting an inner shell electron and cause an Auger cascade with possibly one or more holes in the valence state. The ICC for the $^{119m}Sn \rightarrow ^{119}Sn^*$ transition (65.66 keV) is not given. However, given that the spin, I, of the two states are I($^{119}Sn^*$)=11/2- and I(^{119m}Sn)=3/2+ (where the + and - are the parities of the state) and that the multipolarity of the transition is given as $L=|I_f - I_i|$ $=|11/2-3/2|=4$ with a parity change between states gives a magnetic sixteenpole transition (M4) (Eisberg and Resnick 1985). From ICC data tables compiled by Rösel et al (1978), given the atomic number for Sn=50 and the energy of the transition (65.66 keV), α=5962±300 using linear interpolation between 56 and 68 keV as given in the tables. This is a highly internally converted transition and may lead to effects in the Mössbauer spectrum which may otherwise not exist in an absorber experiment. To calculate the portion of the Mössbauer spectrum which shows the Sn atoms possibly undergoing an Auger cascade, assuming that the two γ-rays emitted (23.9 and 66.65 keV) interact only with their own electronic environment (i.e. a dilute source in which surrounding ^{119}Sn and ^{119m}Sn atoms are not affected), four events can occur, as shown in Table 4.2.

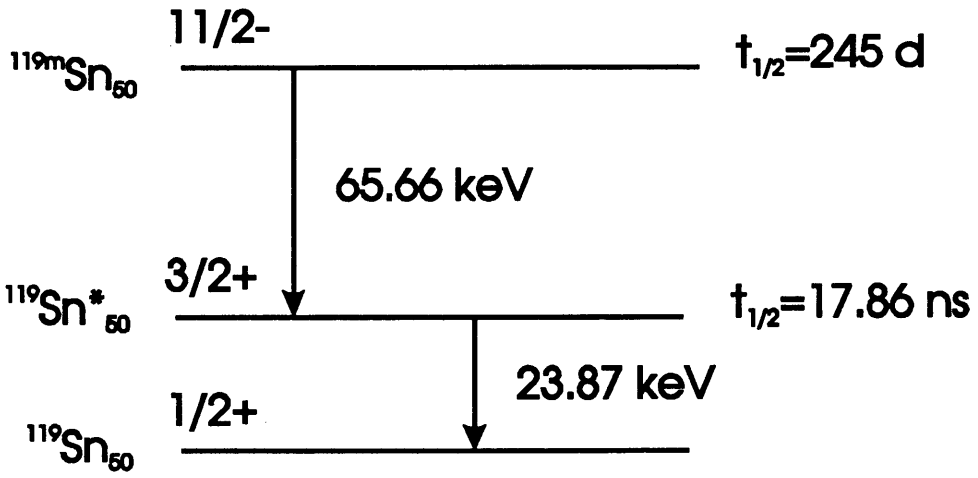

Figure 4.1 The decay scheme for $^{119}Sn_{50}$. From Mössbauer Effect Data Index by John G. Stevens and Virginia E. Stevens, Plenum Publishing Corp., NY, p. 130 (1978).

Two of these transitions are observed using transmission Mössbauer spectroscopy (γ-ray detection), that is $IC_{11/2-\rightarrow 3/2+}\rightarrow\gamma_{3/2+\rightarrow 1/2+}$ and $\gamma_{11/2-\rightarrow 3/2+}\rightarrow\gamma_{3/2+\rightarrow 1/2+}$ with probabilities of $(\alpha_{66}-1)/(\alpha_{66}\alpha_{24})$ and $1/(\alpha_{66}\alpha_{24})$, respectively. Normalizing these gives the fraction of the Sn in these states: 0.99985 and 0.00015, respectively. From this, 99.985 % of the spectrum will represent the first transition (IC→γ). What also needs to be considered is the lifetime of the Auger cascade with respect to the Mössbauer γ-ray. There is 17.86 ns of delay (the lifetime of the ^{119}Sn* state) between the emission of the 65.66 keV γ-ray and that of the 23.9 keV Mössbauer γ-ray. Assuming that the lifetime of the Auger cascade is on the order of 10^{-12} s (Williamson et al 1992) then the Mössbauer γ-ray will reflect the ground state electron shell of the atom.

Table 4.2 The four events that can occur in the ^{119m}Sn nucleus and their associated probabilities.

EVENT [α_{66}~6000, α_{24}~5]	Probability for 11/2- →3/2+ transition	Probability for 3/2+→1/2+ transition
Internal Conversion	$(\alpha_{66}-1)/\alpha_{66}$	$(\alpha_{24}-1)/\alpha_{24}$
Gamma Ray Emission	$1/\alpha_{66}$	$1/\alpha_{24}$

However, in the case of Sn in AlGaAs at low temperatures (e.g. 4.2 K), it is possible that the Auger cascade can contribute to the excitation of the Sn DX center by having one or more electrons remain in the conduction band (the PPC state without external

photoexcitation). Hence, the 99.985% of the spectrum observed could be that of the DX center's excited state. This may also be true at 76 K where the decay of the PPC effect is on the order of seconds. What could also occur is that any of the electrons ejected from the inner shells may have sufficient energy (hot electrons) to thermalize down to the lowest level in the conduction band and therefore lose energy in the form of heat to the lattice. If the DX center is initially excited due to the Auger cascade (or from the LED), the energy from the hot electrons can cause local heating. If this heating provides at least, in the case of Sn, >0.1 eV (the thermal capture barrier reported by Lang and Logan (1979)), the DX center can revert back to the ground state. If these events occur within a time less than the lifetime (17.86 ns) of the ^{119m}Sn state, the spectrum will represent the ground state of the DX center or the excited state if the events last longer. Therefore, it is argued that source experiments using ^{119m}Sn to study DX centers in a specific state may prove difficult.

A previous study utilizing Sn Mössbauer source experiments has shown differences between these and absorber experiments, in the form of additional charge states found in the source experiments. This study by Llabador and Friedt (1971) has found that source experiments on $^{119m}SnSO_4$ yielded an additional quadrupole split peak, attributed to Sn^{4+} (δ=0.3 mm/s, Δ=1.7 mm/s) along with the Sn^{2+} peak (δ=3.96 mm/s, Δ=0.98 mm/s) found in the absorber experiment at 100 K. The authors have explained this phenomenon as being due to the Auger cascade, triggered by the 65.66 keV γ-ray, leaving a Sn^{4+} charge state with a lifetime longer than the 23.9 keV Mössbauer one.

A related effect which can affect the resonance from source experiments involve non-isomeric transitions. Langouche et al (1988) have used ^{129}I Mössbauer spectroscopy to study the site occupation of implanted ^{129m}Te. Here ^{129m}Te decays to ^{129}I and this has to be taken into account when interpreting the data. That is, the implantation, annealing, and defect association processes are typical for Te, but during the 16.8 ns lifetime of the Mössbauer excited state the electronic configuration around the nucleus will rearrange and become characteristic of ^{129}I.

4.3 Experimental Procedure

Schematic diagrams of the Mössbauer spectroscopy apparatus are shown in Figures 4.2 and 4.3. Data were collected at either liquid nitrogen or liquid helium temperatures in the dark and under illumination via an IR LED operating in a wavelength range of 895 to 1005 nm. Sample heating and excessive He boil-off under the 4.2 K condition due to the LED radiation was minimized by illuminating the sample for 3 five second intervals, with LED currents less than 100 mA, which kept the temperature below 10 K after 5 seconds (@ 100mA). If the LED was to be kept on during the whole run, the LED current was set to 5 mA which kept the temperature down to a constant 5 K. The Ge solid state detector used was suitable for the very low radiation levels encountered in the source experiments due to its high efficiency. Its ability to resolve the K-shell ^{119}Sn x-ray (25.8 keV) due to internal conversion and the Mössbauer γ-ray (23.87 keV) eliminated the requirement of a Pd x-ray filter, which can attenuate the Mössbauer γ-ray

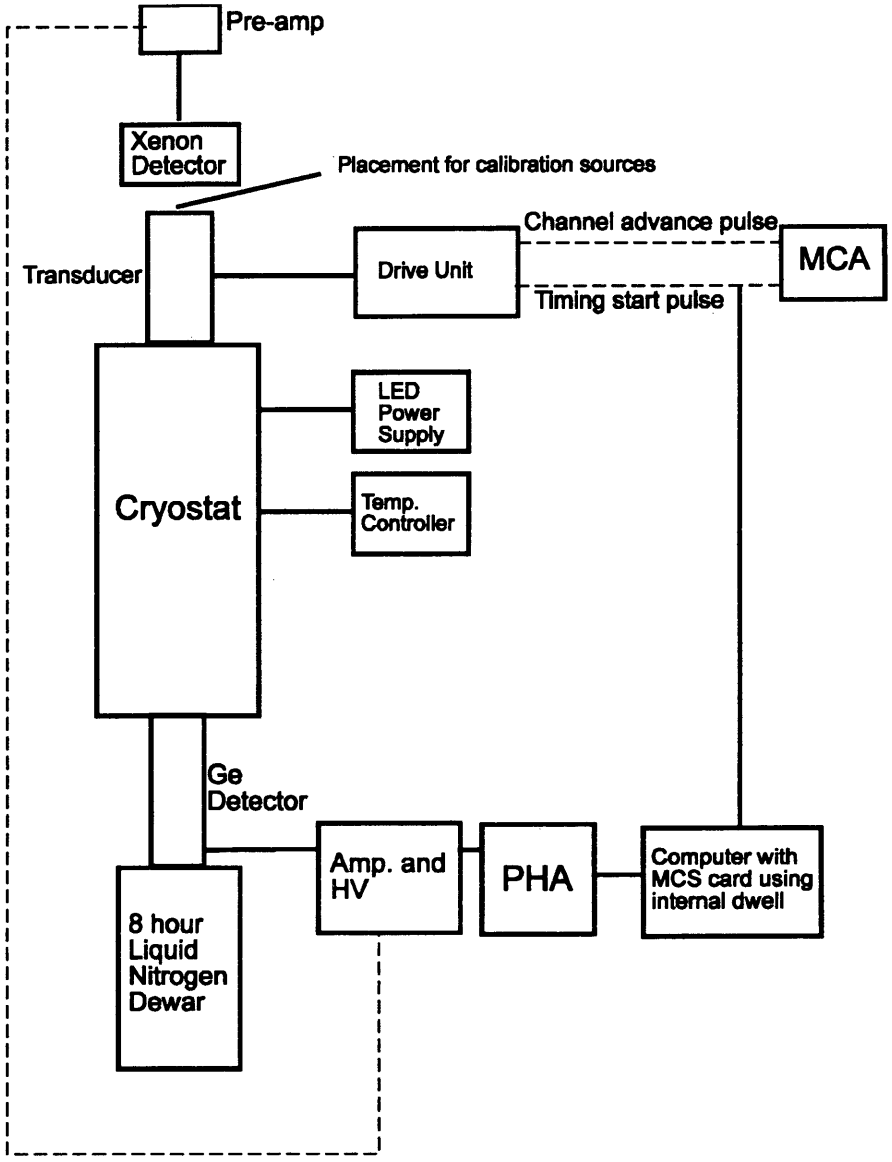

Figure 4.2. Schematic diagram of the Mössbauer apparatus at CSM. The dotted lines represent an alternate configuration for calibration spectra acquisition.

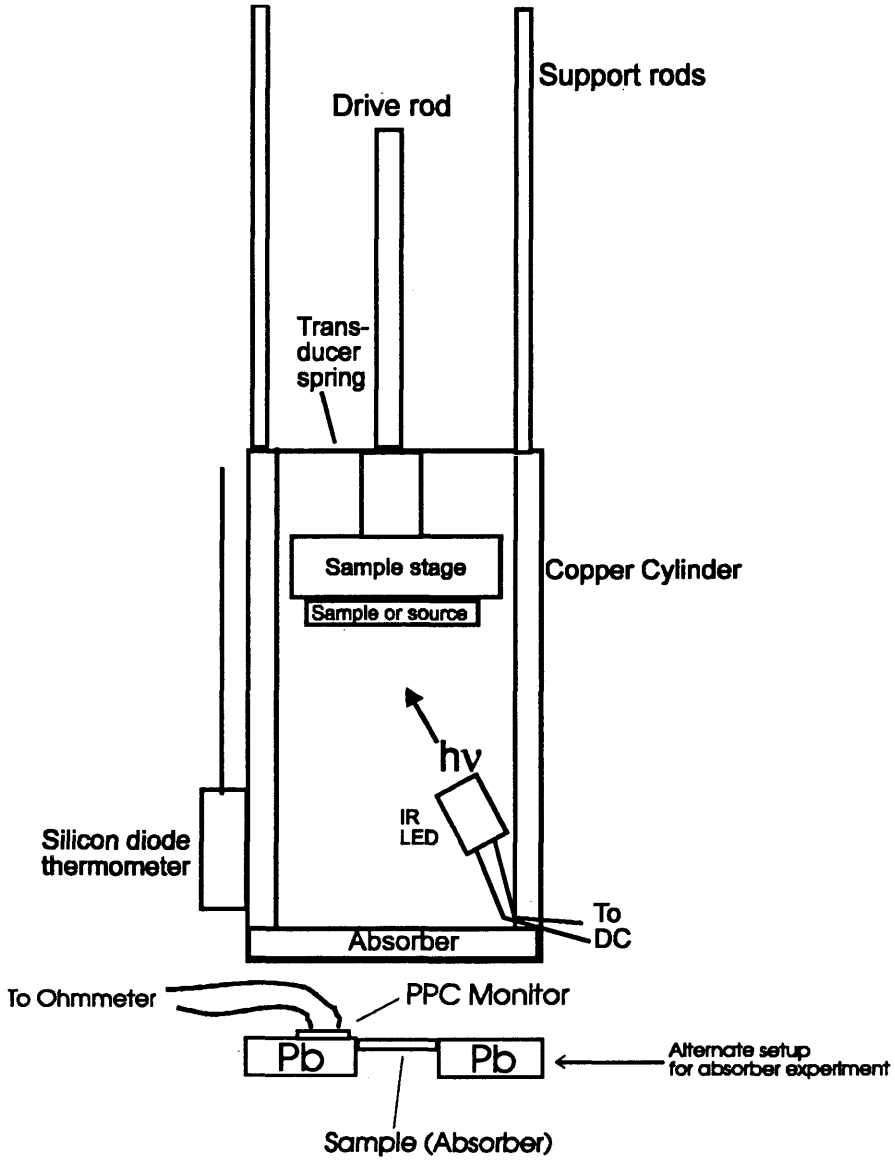

Figure 4.3. A diagram of the cold-finger used to mount the samples in the cryostat. The sample resides at the bottom of the cryostat. The IR LED faces downwards for the absorber experiments.

due to mass absorption. Velocity calibrations were done via a ^{57}Co (14.4 keV γ-ray) source and enriched Fe absorber mounted on the opposite end of the drive unit with a xenon gas-filled detector (as shown in Figure 4.1) or with a $CaSnO_3$ source and a $CaSnO_3$+SnTe absorber.

All the Mössbauer data parameters shown in this work have been obtained with a computer fitting program called NORMOS, which fits the acquired Mössbauer spectra with Lorentzian lineshapes and computes the relevant parameters.

4.3.1 Absorber experiment

The sample used in this study was a 40 μm thick $Al_{0.15}Ga_{0.85}As$:Sn (86 % ^{119}Sn) grown on semi-insulating (100) GaAs by Pierre Gibart at CNRS. The change in the carrier concentration (via Hall measurements at Grenoble, France) for this sample, due to PPC at 4.2 K, was from $2.1x10^{18}$ cm^{-3} (dark) to $2.3x10^{18}$ cm^{-3} (light); a 10 % increase.

In order to use this sample as an absorber, the GaAs substrate (~400 μm) must be removed. This is due to the fact that $2/\mu$ (μ=mass absorption coefficient) is approximately 162 μm for x=0.15 ($2/\mu$=152 μm for x=0.0) and corresponds to the maximum signal-to-noise ratio for a dilute sample in the transmission geometry (Williamson et al 1992). A method was devised by cleaving the sample into four 1cm x 1cm pieces, mounting each of them on mylar with clear wax, lapping and etching the GaAs, and stacking them in order to obtain a thickness close to the 162 μm thickness required. This is described

below.

The x=0.15 sample was cleaved using a razor blade and straight edge into approximately 1cm x 1cm pieces. Any raised regions on the AlGaAs side of the sample were lightly finger-lapped in 12 μm SiC powder/ H_2O slurry. The thickness of each piece was measured with respect to the lapping tool flat using a dial indicator with a resolution of ± 2.5 μm. Each piece was mounted separately on the lapping tool by melting beeswax (at 160°C) on the tool surface, applying a sheet of mylar, then increasing the temperature to approximately 200°C and applying clear wax on top of the mylar. The sample was placed AlGaAs-face down on the clear wax. Additional clear wax was applied along the edges of the sample for protection during lapping. The sample was then seated by applying slight pressure to the sample using two wooden dowels and using slight lateral motion to remove any air pockets between the sample and the mylar. It was found later that allowing this to cool under the pressure of the dial indicator afterwards provided the best seating and mechanical stability (i.e. no stress cracks were generated during lapping). The total thickness was then measured. The lapping medium was a 12 μm SiC powder + deionized water slurry by which most of the GaAs was removed. When a sample thickness of approximately 100 μm was reached, the sample + mylar mount was carefully removed from the lapping tool by heating to approximately 70°C and pushing it off the tool laterally with a razor blade.

The rest of the GaAs (60 μm) was removed by selective etching. The etch used was a H_2O_2 + dropwise addition of NH_4OH solution set to a pH between 7.15 and 7.20 at

25°C (which allows approximately 4-6 μm/hr etching rate for GaAs under agitation) (Logan and Reinhart 1973). The average time for etching the x=0.15 sample was between 37 and 56 hr, which roughly corresponds to etch rates between 1.6 μm/hr and 1.1 μm/hr, respectively. The reason for these comparatively low etch rates may be due to the age of the H_2O_2 used. The highest etch rates should be possible with fresh H_2O_2, which was not the case here. During etching, cracks in three of the four samples were becoming visible and at times small pieces came loose from the wax. After etching was completed, these pieces were re-attached to the mylar with a clear wax + acetone slurry applied with a small paint brush. The slurry was also brushed on the whole surface of the sample (after etching) which also allowed the samples to be held in place during cooling in the cryostat, since preliminary tests on 60 μm GaAs attached to mylar showed that upon cooling to 76 K, differences in thermal expansion caused the GaAs to crack and peel away from the mylar. Slow cooling should reduce this effect.

The average thickness of each sample was determined by mass absorption of the 23.9 keV γ-rays from a $CaSnO_3$ source. A stage was devised to monitor the count rate attenuation due to one or multiple samples using a xenon gas detector. The count rates due to the mylar and the individual samples were measured. From the intensity attenuation, $I=I_0\exp(-\mu t)$, where μ=0.0123 μm^{-1} for x=0.15, t is the thickness in μm, and I_0 is the average count rate for 4 blank mylar sheets, thicknesses ranging from 39 to 59 μm were obtained. Three of the samples were selected to give a total thickness of 142 μm ($2/\mu$=162 μm corresponds to the maximum signal-to-noise ratio). A Pb mask (2.5 cm

diameter) with a 1 cm^2 square aperture was fabricated on which the samples were stacked using pieces of masking tape along the mylar to hold them in place. A PPC monitor (a small piece of the unlapped sample having two ohmic contacts) was placed adjacent to the samples in the cryostat (Figure 4.3) to observe the effect of illumination during data collection (via resistance measurement).

To determine the amount of time required to ionize the DX centers present in these samples the infrared transmission of the stacked samples was tested by using two GaAs LEDs (one for emission and one for detection). These have a half-power beamwidth of 30° and were spaced approximately 2.5 cm apart. The LED used for detection achieved a maximum of 0.73 V bias ($\sim E(GaAs)_{gap}/2$) when irradiated and was suitable for use as a detector by measuring this voltage as a function of the thickness of the sample place in between. The detector voltage was reduced by a factor of 7 when the stacked samples were introduced between the two LEDs. In effect, the detector LED acts as a solar cell. From Streetman (1990) the open circuit voltage measured, V_{oc}, is assumed proportional to $\ln(g_{op})$ where g_{op} in the rate of electron-hole pair generation per unit volume which is proportional to the intensity of the incident radiation. V_{oc} does not rise indefinitely but approaches the limit of the contact potential (V_o) in a p-n junction ($kT/e \ln(N_a N_d/n_i^2)$, where k is Boltzmann's constant, T is in Kelvins, e=electron charge, N_a, N_d and n_i are the concentrations of acceptors on the p-side, donors on the n-side and the intrinsic carriers (for GaAs=$2x10^6$ cm^{-3}), respectively. Details of the LED doping were not given in its specification sheet. Estimating the intensity attenuation: $e^{0.11}/e^{0.73}=I/I_o=0.54$. The

incident beam was attenuated by a factor of 2 with three samples. The approximate time to excite the DX centers in this sample when mounted in the Mössbauer apparatus is = $N/\mu I_o[\exp(\mu t)-1]$, where $N=Sn/cm^2$ (concentration X layer thickness), I_o is the incident photon intensity (cm^{-2}-s^{-1}), μ is the absorption coefficient calculated from the IR absorption experiment, and t is the sample thickness. For $N=1.2x10^{16}$ cm^{-2} (3 layers, 142 μm thick), $\mu=43$ cm^{-1}, $I_o \sim 2x10^{16}$ cm^{-2}-s^{-1} (1.4 eV photons incident on the inside wall of the cold finger copper cylinder with 60 mA LED current) then the time is 0.01 s to excite all the DX centers in the sample.

4.3.2 Source experiment

Two samples were investigated in this study: $Al_xGa_{1-x}As$:Sn with x=0.22 (10x12 mm^2 with a 621 nm thick layer implanted with 10^{14} Sn/cm^2 at 160 keV and 300 K) and x=0.25 (10x16 mm^2 with a 600 nm layer implanted with $4.5x10^{13}$ Sn/cm^2, 160 keV and 300 K). According to TRIM calculations the average implantation depth was approximately 53 nm. The AlGaAs layers were grown by MBE on (100) GaAs by collaborators at K.U., Leuven, Belgium and the implantation was carried out by them at a special facility for radioactive ion implantation in Bonn, Germany. Figure 4.4 shows the concentration versus depth for both samples based on TRIM range calculations by taking the total dose (as given above) and multiplying by the normalized TRIM ion range data. The peak concentrations at 53 nm were approximately $1.8x10^{19}$ and $8x10^{18}$ cm^{-3} for the x=0.22 and 0.25 samples, respectively.

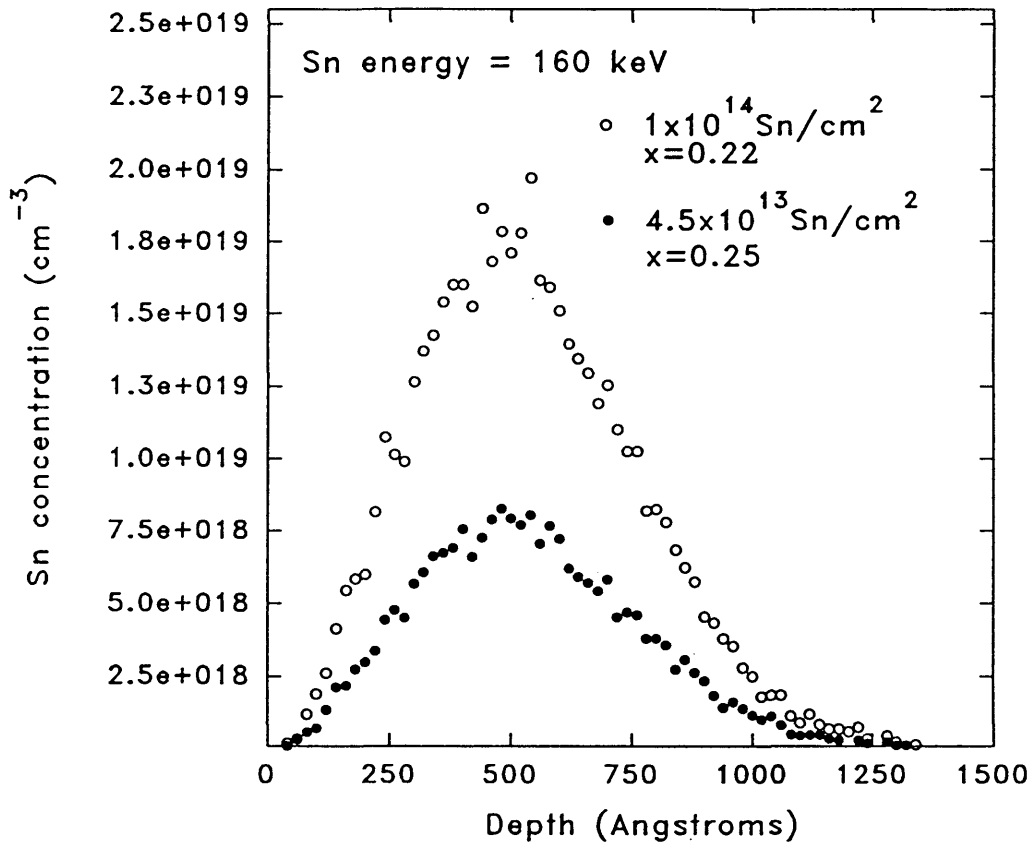

Figure 4.4. Concentration profile for the x=0.22 and 0.25 Sn-implanted samples based on TRIM calculations.

An estimate of the activity of each sample was made. Using the relation to calculate the activity of radioactive material, $A=[(\gamma/sec)4\pi r^2\alpha_{24kev}]/[(3.7x10^{10}Bq/Ci)\kappa A_{det}]$ where γ/sec are the number of counts per second detected in a detector area of A_{det}, r is the source-detector distance in the cryostat, $\alpha_{24\ keV}$ is the internal conversion coefficient for the 23.9 keV Mössbauer γ-ray and κ is the detector efficiency. The as-received x=0.22 and 0.25 samples had count rates of approximately 8 and 5 counts/s, respectively. Using r=9.5 cm, α=5.0, κ=1.0, A_{det}=5.1 cm^2, the activities were 0.24 and 0.15 μCi, respectively. The fraction of Sn in the samples as ^{119m}Sn when they were received (March 1993 at the above mentioned count rates) can be estimated by using the radiation decay law, $N=N_o\exp(-\lambda t)$, and differentiating it with respect to time to get the activity (Ci)=$-N_o\lambda\exp(-\lambda t)/3.7x10^{10}$ Bq/Ci. For ^{119m}Sn $t_{1/2}$=245 days and $\lambda=3.3x10^{-8}$ s^{-1}. At t=0 and using the activities 0.24 and 0.15 μCi for x=0.22 and 0.25, respectively, $N_o=2.7x10^{11}$ and $1.7x10^{11}$ ^{119m}Sn, respectively. The total Sn for each sample (Dose X area) is $1.2x10^{14}$ (x=0.22) and $5.4x10^{13}$ (x=0.25), assuming uniform implantation. Therefore, the fractions of ^{119m}Sn are $2.3x10^{-3}$ (x=0.22) and $3.2x10^{-3}$ (x=0.25). At these activities, a significant amount of time is required to obtain spectra with approximately 1% statistical noise. That is, the number of counts required per channel, N, would be 10,000 ($100/(\sqrt{N})$=1%). With 256 channels in the MCA data acquisition electronics, $256x10{,}000=2.56x10^6$ counts are needed. This would require $2.56x10^6$/(5 or 8/s)=$5.1x10^5$ s (or $3.7x10^5$ s) of data collection time. As will be discussed later, the count rate decreased due to the loss of Sn during the heat treatments used.

For the Mössbauer measurements the samples were mounted to the oscillating aluminum stage (Figure 4.2) with Apiezon grease and a small amount of masking tape with the AlGaAs:Sn side facing a $CaSnO_3$ standard absorber. A small piece of Pb tape was used to cover the corner region (~2 mm^2) of the sample not capped with SiO_2 (this is where the sample was clamped during deposition), since during subsequent heat treatments this region decomposed and extraneous forms of Sn were therefore prevented from contaminating the Mössbauer spectrum. The LED was mounted as shown in Figure 4.3.

4.4 Results and discussion

4.4.1 Source experiment (x=0.22)

Table 4.3 lists the Mössbauer fit parameters from the acquired spectra for all the heat treatments performed. The quality of the fits is also listed in terms of the χ^2 (best statistical fit approaches χ^2=1.0). The fractional areas (A1 and A2) are given in terms of mm/s and a percent of the total area [A(TOT)]. Numbers in parentheses are the errors in the last significant figure in the measurement. The 4 K light measurements used an IR LED illuminating the sample for 15 s at 100 mA LED current except for one measurement under constant illumination using 5 mA (700°C x 20 min anneal case).

From Table 4.3 the percent change in fractional area between the dark (D) and the light (L) for each component, i, written as A_i(4KD)-A_i(4KL), is listed in Table 4.4.

Table 4.3. Mössbauer parameters for the x=0.22 sample under 76 K dark (D) and 4 K dark and light (L) conditions. The isomer shifts are relative to $CaSnO_3$ at 300 K. The line intensities D1 and D2 are shown as percent absorption for the singlet and doublet, respectively. W1 is fixed at 1.0 mm/s. W2 is the linewidth of the second component in mm/s, freed for the as-implanted case and fixed at 1.0 mm/s for the annealed cases. D2R and W2R are the depth and width ratios for the doublet. The areas A1 and A2 are shown in mm/s and below this in percent of the total area, A(TOT). All measurements in the light used 15 s illumination at 100 mA for the LED (except for one, run P21L, made under a constant illumination at 5 mA). All measurements were made with a 50 mg $CaSnO_3$ absorber.

RUN	TREAT. COND.	D1	δ1 mm/s	D2 W2	D2R W2R	δ2 mm/s	Δ mm/s	χ^2	A1	A2	A(TOT)
P9A	AS-IMP 76K D	4(1)	-1.89(F)	12.9(2) 1.39(3)	0.89(8) 0.73(5)	-2.21(2)	1.50 (3)	1.02	0.06(2) 11(4)	0.47(2) 89(6)	0.53(3)
P12D	4K D	6(1)	-1.89(F)	15.9(4) 1.55(6)	0.73(8) 0.67(8)	-2.20(2)	1.66 (4)	1.11	0.10(2) 15(3)	0.57(4) 85(8)	0.67(4)
P12L	4K L	4(2)	-1.89(F)	16.5(4) 1.51(9)	0.84(9) 0.67(8)	-2.21(3)	1.55 (7)	0.87	0.07(4) 10(6)	0.61(4) 90(10)	0.68(6)
P18D3	400CX20M 76K D	30.7(6)	-1.875(7)	2.2(3)	1.0(F) 1.0(F)	-2.66(1)	0.6(F)	0.89	0.48(1) 87.6(24)	0.07(1) 12.4(18)	0.55(1)
P18L3	4K L	36.6(8)	-1.898(8)	3.1(4)	-	-2.62(8)	-	0.88	0.57(1) 85.7(29)	0.10(1) 14.3(16)	0.67(2)
P22D2	700CX20M 76K D	21.5(4)	-1.85(1)	5.1(2)	-	-2.78(3)	-	1.18	0.337(6) 67.8(17)	0.161(6) 32.2(13)	0.50(1)
P20L3	4K L	26.5(5)	-1.89(1)	6.7(3)	-	-2.89(3)	-	1.23	0.417(8) 66.6(15)	0.209(9) 33.4(15)	0.63(1)
P21L	4K L (5 mA)	28.5(8)	-1.92(2)	5.6(4)	-	-2.99(7)	-	1.12	0.45(1) 71.8(28)	0.18(1) 28.2(18)	0.63(2)
P25D2	850CX20M 76K D	18.5(2)	-1.863(6)	5.0(1)	-	-2.85(2)	-	1.02	0.291(3) 64.8(10)	0.158(4) 35.2(10)	0.45(1)
P24L5	4K L	21.3(6)	-1.90(1)	9.1(3)	-	-2.83(3)	-	0.84	0.34(1) 53.9(18)	0.29(1) 46.1(17)	0.63(1)
P27D	900CX20M 76K D	16.4(5)	-1.89(1)	5.6(2)	-	-2.80(3)	-	0.85	0.26(1) 59.4(26)	0.18(1) 40.6(25)	0.44(1)
P28D2	4K D	19.0(3)	-1.86(1)	9.7(2)	-	-2.81(2)	-	0.98	0.30(1) 49.5(18)	0.31(1) 50.5(18)	0.61(1)
P27L	4K L	19.2(9)	-1.78(2)	8.9(4)	-	-2.64(2)	-	0.92	0.30(1) 51.9(25)	0.28(1) 48.1(24)	0.58(2)
P33D16	950CX NO DWELL 76K D	15.4(3)	-1.92(1)	4.9(2)	-	-2.70(3)	-	1.03	0.24(1) 61.1(30)	0.15(1) 38.9(27)	0.39(1)
P35D5	4K D	22.6(7)	-1.92(1)	8.3(4)	-	-2.87(3)	-	0.86	0.35(1) 57.4(41)	0.26(3) 42.6(57)	0.61(4)
P35L7	4K L	19.5(5)	-1.91(2)	8.8(3)	-	-2.78(4)	-	0.99	0.31(1) 52.4(19)	0.28(1) 47.6(19)	0.59(1)

Table 4.4. The change in fractional area, in percent of total area, (from Table 4.3) for both components between the dark (D) and the light (L) in x=0.22.

Treatment	A1(4K D)-A1(4K L)	A2(4K D)-A2(4K L)
as-implanted	5(7)	-5(13)
400°C x 20 min	-	-
700°C x 20 min	-	-
850°C x 20 min	-	-
900°C x 20 min	-2(3)	2(3)
950°C x no dwell	5(5)	-5(6)

These data were used to determine the extent of PPC due to DX centers by observing the change in the site occupation between the dark and light. A_i(4KD)-A_i(4KL) is not listed for the 400, 700 and 850°C x 20 min anneals since only 4K light data was acquired but no obvious PPC behavior was observed for these anneals, i.e. a clear increase in the singlet relative to the doublet upon illumination. It is not recommended that A_i(76K)-A_i(4KL) be used due to the fact that each site has a different recoilless fraction and therefore the fractional areas will change by different amounts upon cooling the sample. Lower recoilless fraction sites (lower Debye temperature) undergo a larger change upon cooling than higher recoilless fraction ones.

Table 4.5. X=0.22 area ratios A(76K)/A(4K), source recoilless fraction ratio, and Debye temperature for each component, $f_s(76K)/f_s(4K)=[A(76K)K_{4K}]/[A(4K)K_{76K}]$ $=1.032[A(76K)/A(4K)]$, for a 50 mg absorber. D=dark and L=light.

Treatment	**Condition Ratio**	**A1(76K)/ A1(4K)**	**A2(76K)/ A2(4K)**	**f_{s1}(76K)/ f_{s1}(4K) Θ (K)**	**f_{s2}(76K)/ f_{s2}(4K) Θ (K)**
as-implanted	D/D	0.6(2)	0.82(7)	0.6(2) 128(43)	0.85(2) 203(5)
	D/L	0.9(3)	0.77(6)	0.9(3) 254(85)	0.79(6) 181(14)
400°C x 20 min	D/L	0.84(2)	0.7(1)	0.87(2) 223(5)	0.72(1) 152(22)
700°C x 20 min	D/L	0.81(2)	0.77(4)	0.84(2) 201(5)	0.79(4) 181(9)
	D/L (5ma LED)	0.75(2)	0.89(6)	0.77(3) 172(7)	0.92(6) 258(17)
850°C x 20 min	D/L	0.86(3)	0.54(2)	0.89(3) 239(8)	0.56(2) 125(4)
900°C x 20 min	D/D	0.87(4)	0.64(4)	0.90(5) 254(14)	0.66(4) 143(9)
	D/L	0.87(4)	0.58(4)	0.90(5) 254(14)	0.60(4) 128(9)
950°C x no dwell	D/D	0.69(3)	0.58(8)	0.71(4) 155(9)	0.60(8) 128(17)
	D/L	0.77(4)	0.54(4)	0.79(4) 181(9)	0.56(4) 125(9)

For each heat treatment and each component, i, the fractional area ratio $[A_i(76K)/A_i(4K)]$, source (x=0.22) recoilless fraction ratios $[f_{si}(76K)/f_{si}(4K)]$ and Debye temperatures (Θ_D) are listed in Table 4.5. Here, the recoilless fraction ratios were derived from the relation $A_i=(\pi/2)\Gamma_o f_{si}K(T)$ where A_i is the area of line i, Γ_o is the natural linewidth for ^{119}Sn (0.321 mm/s), f_{is} is the source recoilless fraction for line i and K(T) is the effective absorber thickness, given by $K(T)=Texp(-T/2)[I_o(T/2)+I_1(T/2)]$ where I_o and I_1 are modified Bessel functions of zero and first order, respectively (Bykov and Hien 1963). The absorber thickness $T=\sigma_o f_A a n_A$ where σ_o is the resonance cross-section for the ^{119}Sn nucleus ($1.403x10^{-18}$ cm^2), f_A is the absorber recoilless fraction, a is the natural ^{119}Sn abundance (0.0858) and n_A is the number of $^{119}Sn/cm^2$ in the absorber ($2.8x10^{19}$ Sn/cm^2 for 50 mg and $5.6x10^{19}$ Sn/cm^2 for 100 mg $CaSnO_3$). The value of f_A (at 300K) was obtained from Robinson (1981): $f_A=0.547(17)$. Using a program resident on the CSM VAX (PHL:DEBYE.EXE) the Debye temperature for Sn in $CaSnO_3$ was obtained: $\Theta_D=316(8)$ K. Also obtained were f_A at 76 and 4 K: 0.82(2) and 0.87(3), respectively. The Debye temperatures for each of the recoilless fraction ratios were obtained using DEBYE. EXE (based on the Debye theory briefly discussed in sec. 4.1) by entering separate values of the recoilless fractions at 76 K and 4 K such that their ratio remains constant. The output of the program gives the Debye temperature for each recoilless fraction entered. The actual Debye temperature corresponds to when the program output gives $\Theta_{D\ 76K}=\Theta_{D\ 4K}$.

Figure 4.5 shows the results of the as-implanted Mössbauer measurement. It was expected that the sample was amorphous (dose ~ 10^{14} Sn/cm^2) as was found by Holm and Weyer (1980) for 60 keV Sn-implanted GaAs. The 76 K and 4 K (dark and light) data were fitted with 2 components. The first component is a singlet at $\delta 1$=-1.8 mm/s (fixed), with a fixed linewidth (W1) set at 1.0 mm/s. The fixed isomer shift represents what would be expected for the $Sn_{Ga(Al)}$ and Sn_{As} substitutional sites, as shown in Table 4.1. The fixed linewidth was assumed to be 1.0 mm/s based on the thickness of the absorber used (50 mg $CaSnO_3$). The second component is a quadrupole doublet with all the parameters freed. These parameters were initially set to: $\delta 2$=2.0 mm/s, linewidth W2=1.0 mm/s, linewidth ratio W2R=1.0 mm/s, intensity ratio D2R=1.0, and quadrupole splitting Δ=1.0 mm/s. This fit represents an alternate method of fitting to that used by Holm and Weyer (1980). The broadened, asymmetric quadrupole doublet may be due to a distribution of amorphous Sn sites including Sn-vacancy complexes and interstitials. Table 4.4 shows that a 5% change in the fractional areas has occurred. With the relatively large uncertainties it was not possible to determine if this is a real effect. The behavior is also the reverse of what is expected for PPC, the area of component 1 (substitutional site) should increase upon illumination [A(4KD)-A(4KL)<0]. Since the sample was rendered amorphous due to the dose used, consistent with the nature of the Mössbauer resonance, no activation of DX centers is a reasonable result. Table 4.5 shows that the average Debye temperature for each site was 191(48) K for component 1 and

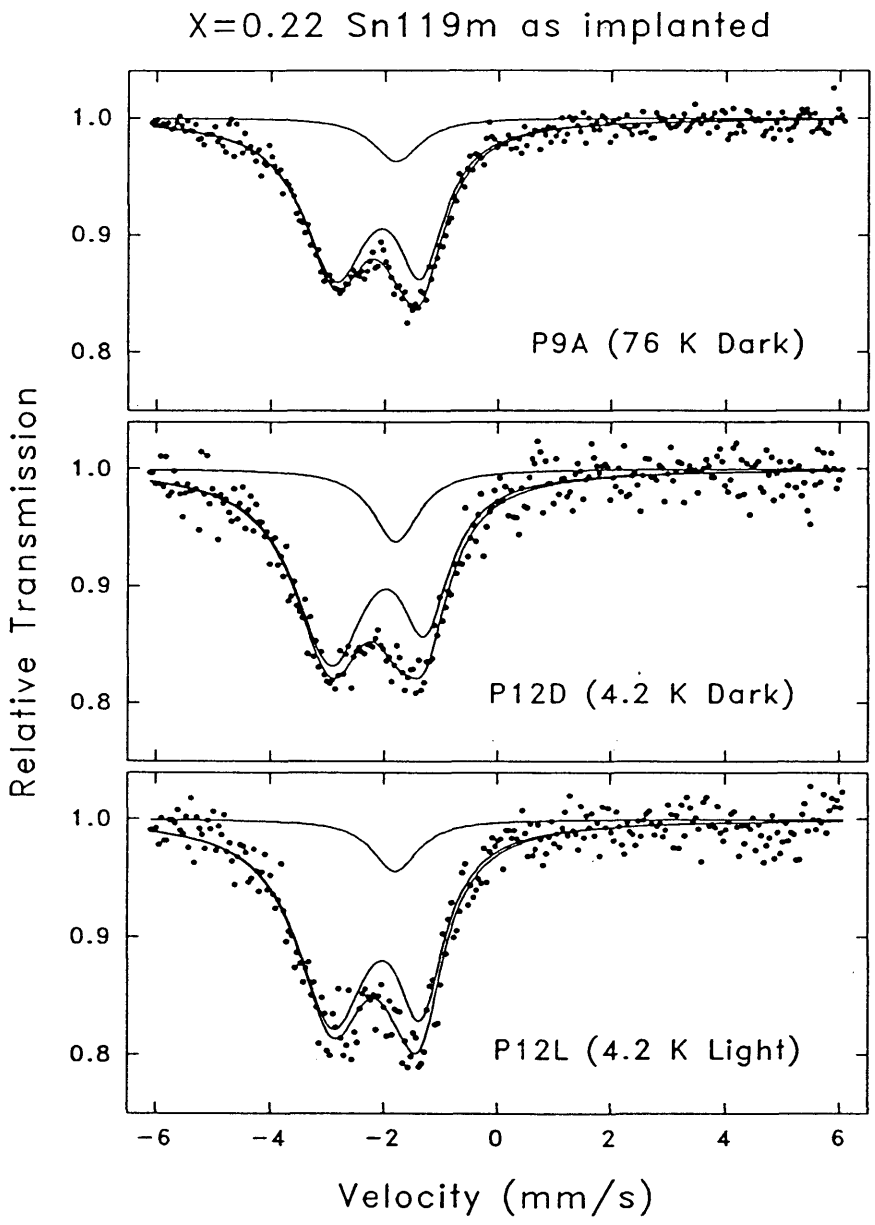

Figure 4.5 X=0.22 Mössbauer data for the as-implanted case.

192(7) K for component 2. From Table 4.1 it can be seen that component 1 can represent substitutional Sn ($Sn_{Ga(Al)}$ and Sn_{As}) for amorphous [158(10) K] and crystalline [~190 K] materials whereas that for component 2 seems to resemble Sn-vacancy type defects [173(10) K] and/or neutral Sn [180(10) K].

Figure 4.6 shows that upon annealing at 400°C for 20 min a large change in the spectra has occurred. The 76 K and 4 K were fitted similarly to that for the as-implanted sample, except that both isomer shifts were freed ($\delta 1$ and $\delta 2$ initially set at -1.8 and -2.6 mm/s, respectively), the quadrupole doublet's width and intensity ratios fixed to 1.0 since the sample was assumed to be recrystallized and the quadrupole splitting fixed at 0.6 mm/s. The weak doublet with $\delta 2$=-2.6 mm/s and Δ=0.6 mm/s may be attributed to a small concentration of DX centers according to the list in Table 4.1. A similar spectrum was also found by Holm and Weyer (1980) after a 400°C anneal. They have attributed this to annealing of implant damage (recrystallization) in GaAs and Sn residing mostly on substitutional sites. Table 4.5 show that the Debye temperature for component 1 is 223(5) K and that of component 2, 152(22) K. Table 4.1 shows that these temperatures may resemble the substitutional Sn site for component 1 and a small amount of $Sn_{Ga}V_{As}$, neutral Sn, β-Sn, SnAs, Sn_3As_2, and possibly Sn DX for component 2.

Figures 4.7-4.9, 4.10 and 4.11 show the 76 K and 4 K Mössbauer spectra for the 700-900°C x 20 min heat treatments, the 900°C x 20 min constant velocity measurement and the 950°C x no dwell time Mössbauer spectra, respectively. The no-dwell-time method consisted of immediate removal of the ampoule once the sample has reached the

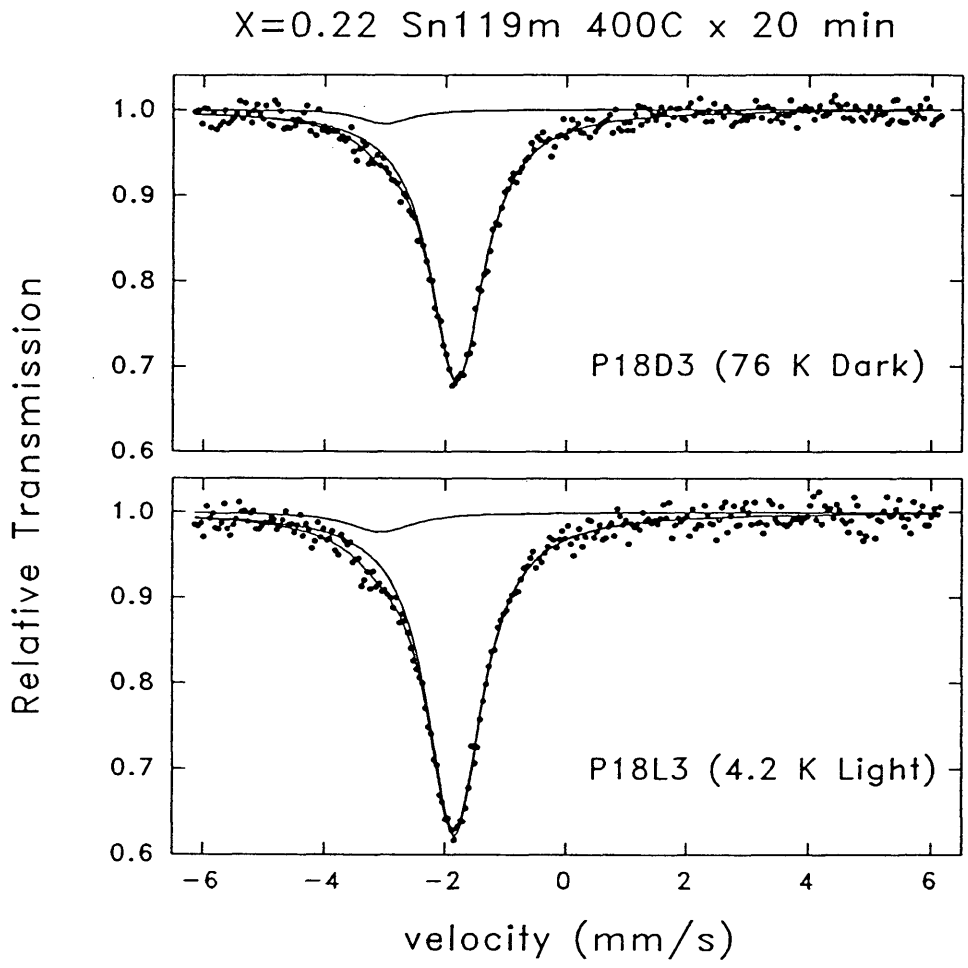

Figure 4.6. X=0.22 Mössbauer data for the 400°C x 20 min heat treatment.

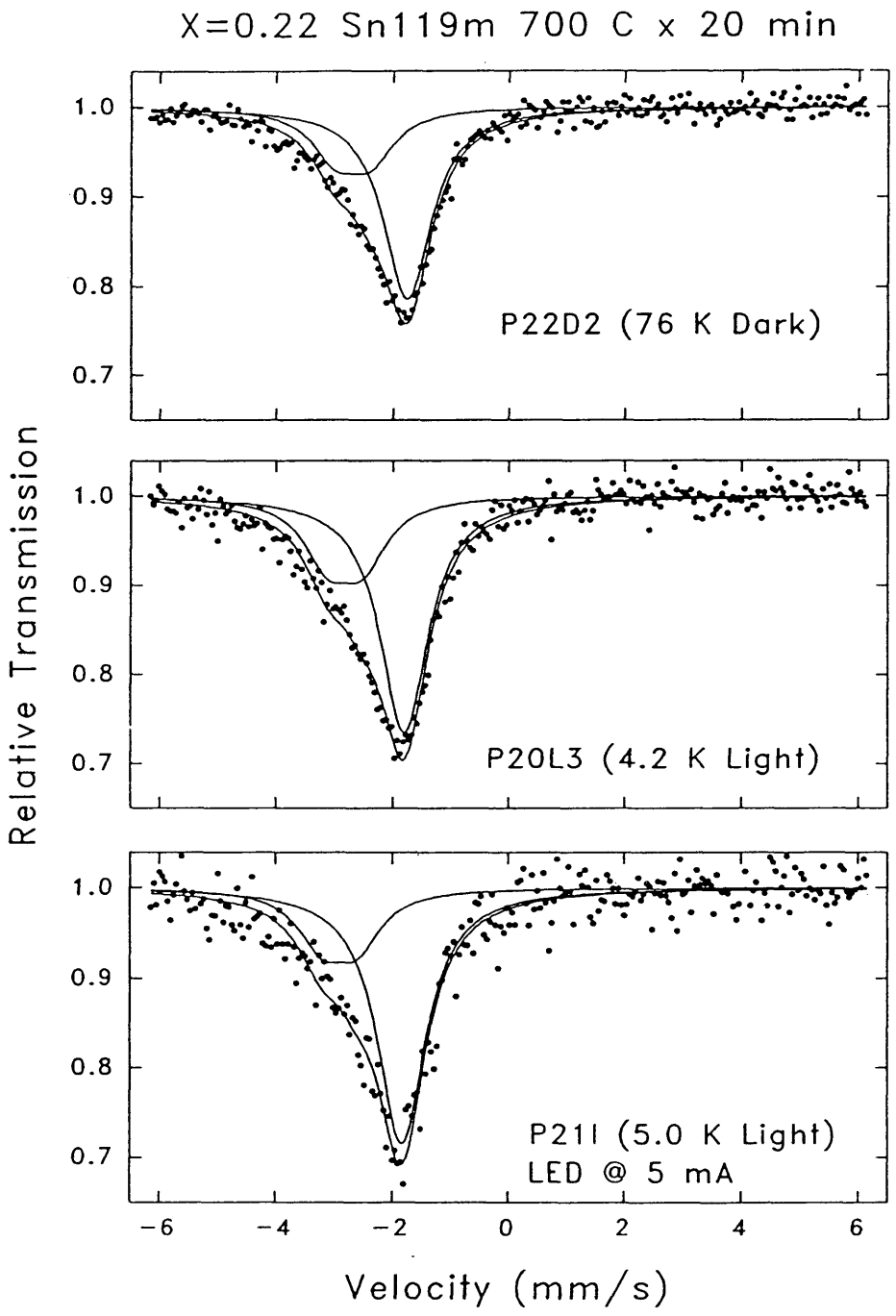

Figure 4.7 X=0.22 Mössbauer data for the 700°C x 20 min heat treatment.

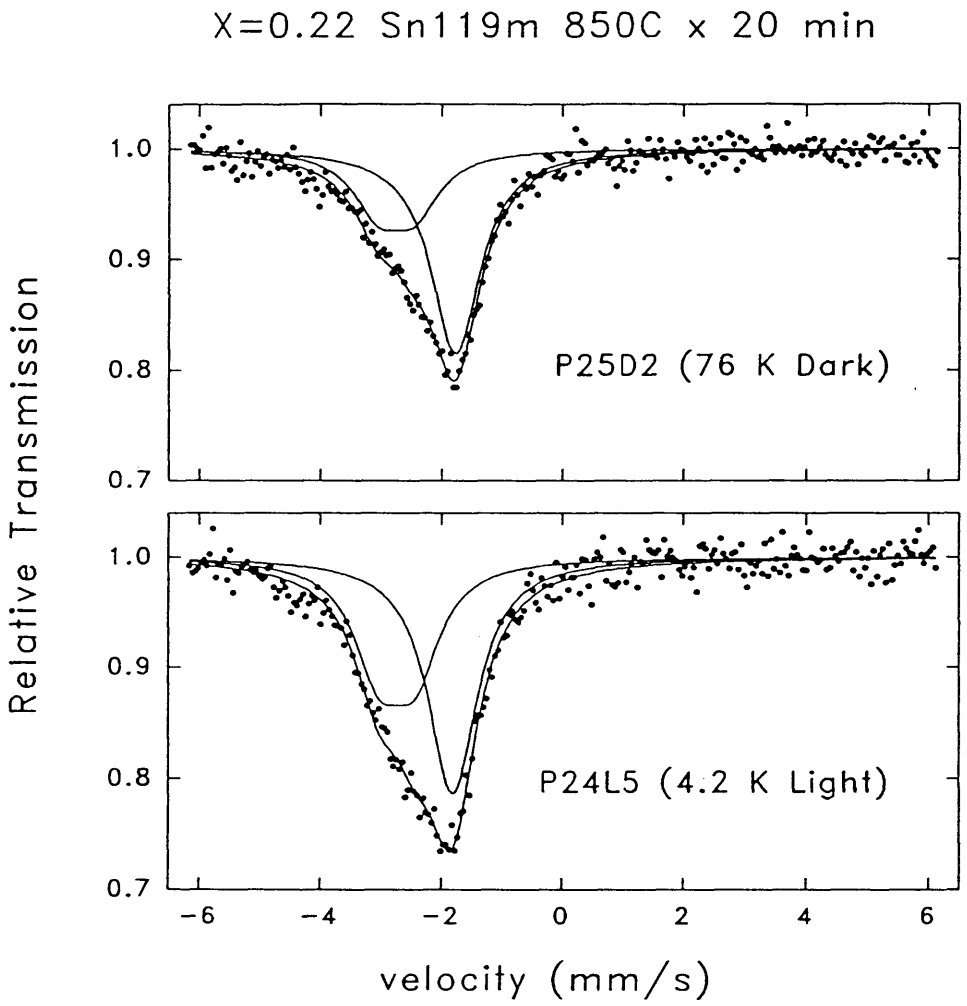

Figure 4.8 X=0.22 Mössbauer data for the 850°C x 20 min heat treatment.

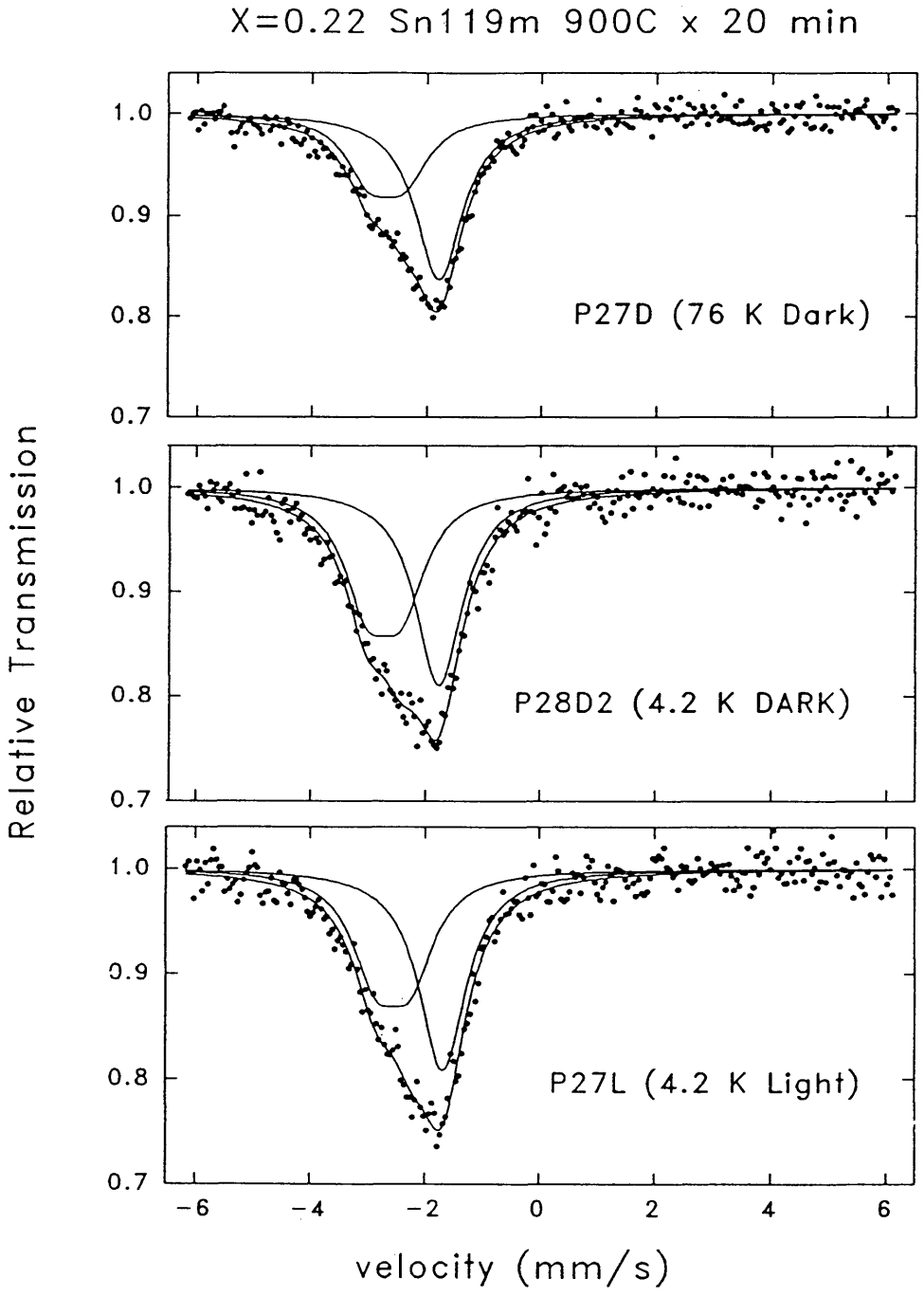

Figure 4.9 X=0.22 Mössbauer data for the 900°C x 20 min heat treatment.

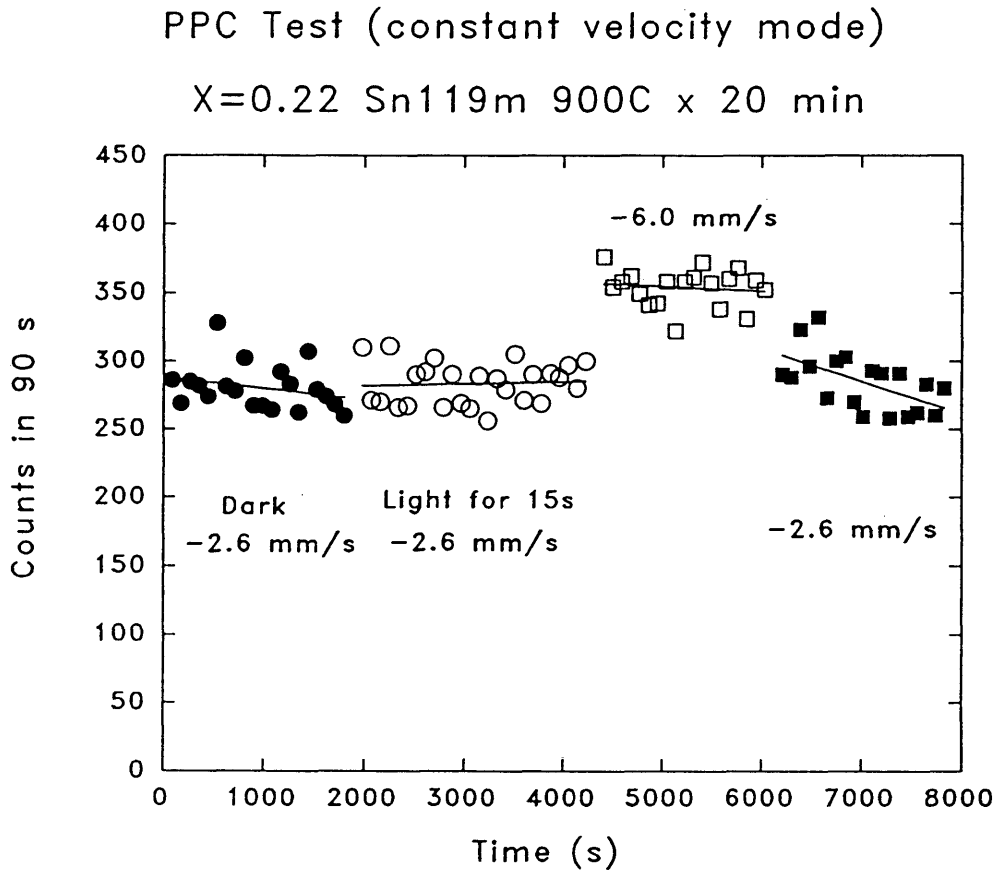

Figure 4.10 X=0.22 results of the constant velocity mode measurement for the 900°C x 20 min heat treatment.

Table 4.6 X=0.22 constant velocity mode data at 4K for 900°C x 20 min. The linear regression fit is defined as y=a1(t)+ao where t is time in s and y is in counts/90 s.

Velocity (mm/s)	Condition	Total Counts	Average Count (per 90 s)	Linear Regression
-2.6	DARK	5608(75)	280.4(37)	ao=288(8) a1=-0.008(7)
-2.6	LIGHT	7371(86)	283.5(33)	ao=279(15) a1=-0.002(5)
-6.0	LIGHT	6718(82)	353.6(43)	ao=371(34) a1=-0.003(7)
-2.6	LIGHT	5411(74)	284.8(39)	ao=451(59) a1=-0.024(8)

specified temperature. Table 4.6 shows the parameters from the constant velocity measurement. The fitting of the spectra is similar to that for the 400°C anneal. From the 76 K data in Table 4.3, the quadrupole doublet increased sharply in size from about 12% to 32% after the 700°C anneal and then it increased more gradually by another ~8% while that of the singlet has decreased by the same amount as the anneals progressed from 700°C to 950°C.

For the 900°C x 20 min heat treatment, Table 4.4 shows that the percent change in the fractional area [±2(3)%] was found to be consistent with PPC behavior (an increase in the fractional area upon illumination) although the uncertainties were relatively large. The behavior was not consistent with PPC after annealing at 950°C.

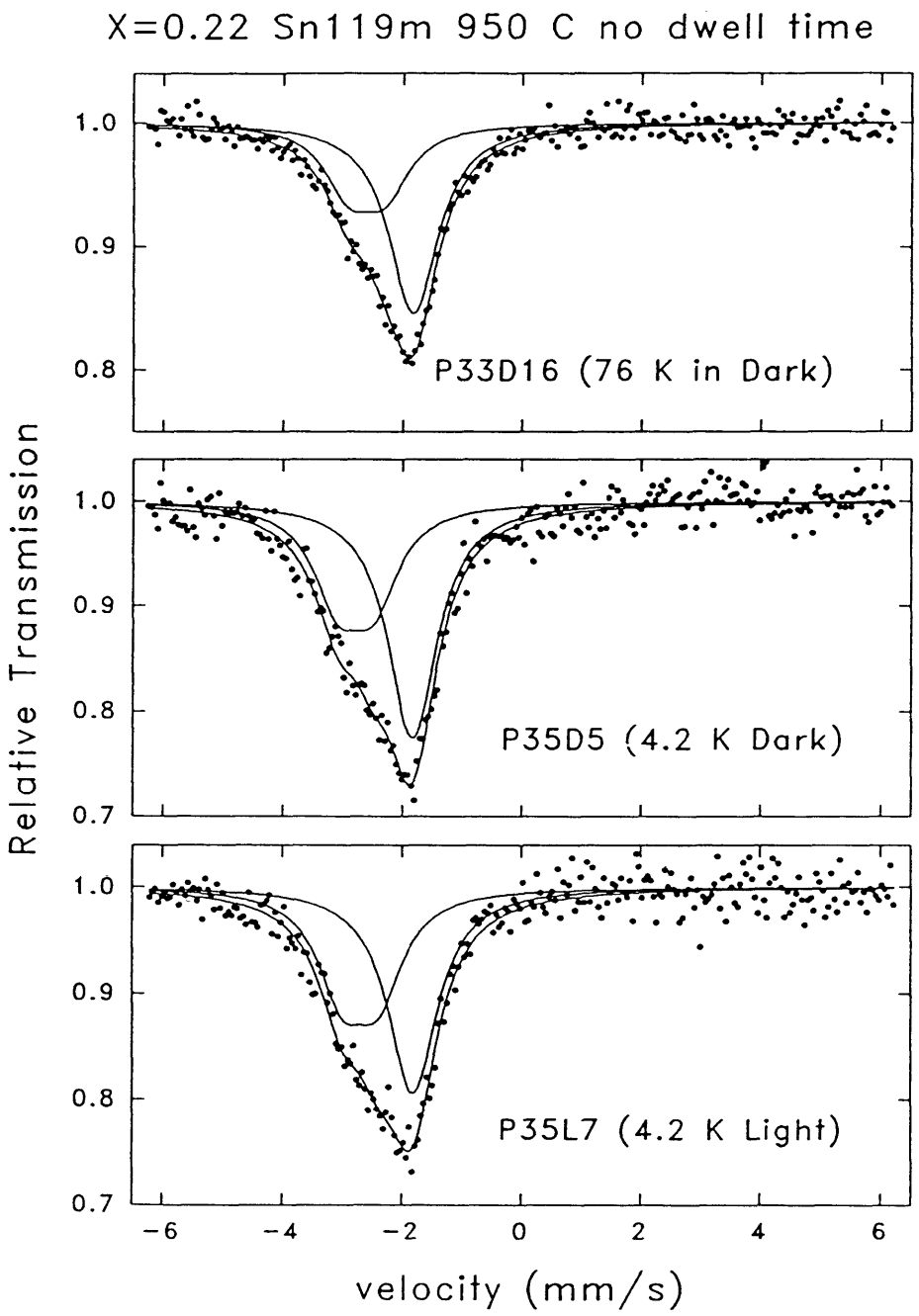

Figure 4.11 X=0.22 Mössbauer data for the 950°C x no dwell time heat treatment.

Since a possible PPC effect was observed after annealing at 900°C, a constant velocity mode measurement was performed. Here, the count rates at the -1.8 and -2.6 mm/s resonances as well as off-resonance (-6.0 mm/s) were measured over a period of time, to acquire good statistics. This measurement allowed for an accurate observation of the PPC effect since the γ-ray counts will fall on these velocities, rather than on a larger spectrum of velocities (± 6.0 mm/s) a significant fraction of which contain no resonances. The count rate in the dark and light was made for the -2.6 mm/s resonance for this sample, as shown in Figure 4.11 and Table 4.6. From this measurement evidence of a possible PPC effect from the -2.6 mm/s component is extremely weak or non-existent. That is, the count rate per 90 s at -2.6 mm/s changes by ~1.4(30) % from the dark to the light with a large measurement error. From the linear regression coefficients the count rate for the different conditions changes with time. With the large errors in the coefficients, it is difficult to determine whether or not there is any change in count rate as a function of time, since this effect could describe the change in the number of Sn sites for the -2.6 mm/s component. The error is not as large for the second measurement at -2.6 mm/s in the light (a1=-0.024(8)). This decrease in count rate as a function of time represents an increase in the Mössbauer effect for this particular component with time (decreased relative transmission). This is consistent with DX centers entering the ground state (assumed to be part of the -2.6 mm/s doublet). Since the illumination was not constant, excited DX centers could possibly have entered the ground state via radiation induced electron-capture.

The average Debye temperature, for the 700 to 950°C cases, from Table 4.5, shows component 1 to have Θ_D=210(4) K and Θ_D=155(4) K for component 2. These can be attributed to the substitutional Sn and various Sn complexes, respectively, as discussed for the 400°C anneal and as shown in Table 4.1. The increase in component 2 with annealing may be an indication that these Sn complexes are increasing in concentration.

As the heat treatments progressed, it was observed that the count rate (or activity) of the sample was decreasing. This is shown in Table 4.7. The decrease in count rate has been attributed to the loss of Sn through the SiO_2 capping layer during annealing.

Table 4.7 Sample count rate as a function of annealing temperature for the x=0.22 sample.

Heat treatment	Count rate (counts/s)
as-implanted	8.0
400°C x 20 min	7.3
700°C x 20 min	7.3
850°C x 20 min	5.2
900°C x 20 min	4.0
950°C x no dwell time	3.3

Measurements of the level of radioactivity on the inner wall of the fused silica ampoules confirmed this. The absence of any Sn-O (Sn^{2+}) complexes in the Mössbauer spectra at ~0 mm/s (Glick 1992) shows that the Sn did not react with and remain the capping layer.

A final test for PPC after the 950°C heat treatment was made by etching off the SiO_2 capping layer with 24%, by volume, HF [(48%)HF: H_2O] and forming two ohmic contacts to measure the resistance at 4 K between the dark and light. In the dark R_{DARK}=3184(16) Ω and upon 15 sec illumination R_{LIGHT}=3156(16) Ω (persistent). This corresponds to a -0.9(7) % change from dark to light. Note that the change in resistance was mostly due to the effects from the stable ^{119}Sn (99.8 % of total Sn, as described in sec 4.3). The low value of the percent change in resistance confirms that the formation of DX was still quite low despite the fact that several anneals were performed to distribute the Sn in the sample and in attempts to lower compensation effects (increase electrical activation). Even if this is true, complex defects may have been formed during annealing arising in compensation and trapping effects, possibly due to vacancy complexes, antisites and Sn_{As} acceptors.

4.4.2 Source experiment (x=0.25)

Tables 4.8, 4.9 and 4.10 list the Mössbauer fit parameters, percent change in fractional area at 4 K dark and light, and the lattice dynamics results for all the heat treatments used, respectively.

Figure 4.12 shows the Mössbauer spectra for the as-implanted sample measured about two months apart. Here, the spectra at 76 K (using a 50 mg $CaSnO_3$ absorber) were fitted similarly to that for the x=0.22 as-implanted case. It was assumed that this sample also had some amorphicity with the Sn dose being about 45% of the x=0.22 sample.

Table 4.8 Mössbauer parameters for the x=0.25 sample under the 76 K dark and 4 K dark and light conditions. The fits are the same as that for the x=0.22 sample except that the linewidths for the 100 mg $CaSnO_3$ are fixed at 1.15 mm/s. For the 850 and 1000°C x 2 h heat treatments the linewidths are fixed at 1.3 mm/s (50 mg $CaSnO_3$ absorber), the second component's isomer shift and quadrupole splitting are fixed at -2.6 and 0.6 mm/s, respectively.

RUN	TREAT.	COND.	D1	δ1	D2R W2R	D2 W2	δ2	Δ mm/s	χ^2	A1	A2	A(TOT)
P26D2	AS-IMP	76K DARK 50mg	16(1)	-1.87(F)	0.79(8) 0.6(1)	8.3(2) 1.6(2)	-2.17(3)	1.65(8)	0.76	0.26(2) 45(5)	0.32(3) 55(5)	0.58(4)
P30D8	2 MOS. LATER	76K DARK 50mg	14(1)	-1.87(F)	0.81(4) 0.7(1)	8.6(2) 1.4(1)	-2.12(2)	1.44(5)	0.84	0.22(1) 43(3)	0.29(2) 57(3)	0.51(2)
P47D	950C NO DWELL	76K DARK 50mg	17.2(7)	-1.87(2)	1.0(F) 1.0(F)	3.5(3)	-2.72(5)	0.6(F)	0.86	0.27(1) 71.1(32)	0.11(1) 28.9(27)	0.38(1)
P48D		76K DARK 100mg	20(2)	-1.82(2)	-	6.4(7)	-2.55(8)	-	0.86	0.35(4) 60.5(76)	0.23(3) 39.5(55)	0.58(3)
P37_8D		4K DARk 100mg	29(2)	-1.87(2)	-	8.1(8)	-2.60(6)	-	0.95	0.51(4) 64.2(55)	0.29(3) 35.9(40)	0.80(3)
P37_8L		4K LIGHT 100mg	28.8(3)	-1.91(1)	-	5.4(4)	-2.82(7)	-	0.91	0.52(1) 72.7(24)	0.20(1) 27.3(16)	0.72(2)
P41D		4K DARK 50 mg	28(2)	-1.92(3)	-	2(1)	-3.0(3)	-	0.98	0.44(3) 85.3(76)	0.08(4) 14.7(77)	0.52(3)
P66AF	850C x 2h	76K DARK 50 mg	18.4(3)	-1.83(1)	-	3.1(2)	-2.6(F)	-	1.10	0.375(6) 75(2)	0.126(8) 25(2)	0.50(1)
P67DAB		4K DARK 50 mg	23.8(5)	-1.83(1)	-	3.6(4)	-	-	1.16	0.49(1) 77(2)	0.15(1) 23(2)	0.64(1)
P67LAB		4K LIGHT 50 mg	24.6(6)	-1.85(2)	-	3.0(3)	-	-	1.21	0.50(1) 80(2)	0.12(1) 20(2)	0 .62(1)
P68AE	1000C x 2h	76K DARK 50 mg	18.0(4)	-1.83(2)	-	3.2(2)	-	-	0.89	0.368(8) 74(2)	0.13(1) 26(2)	0.50(1)
P69DAB		4K DARK 50 mg	20.2(6)	-1.84(2)	-	6.5(4)	-	-	1.09	0.41(1) 61(2)	0.26(1) 39(2)	0.67(1)
P69LAC		4K LIGHT 50 mg	19.9(4)	-1.83(1)	-	6.5(3)	-	-	1.00	0.41(1) 61(2)	0.26(1) 39(2)	0.67(1)

Table 4.9 The change in fractional area, in percent of total area, (from Table 4.8) for both components between the dark (D) and the light (L) for x=0.25.

Treatment	A1(4KD)-A1(4KL)	A2(4KD)-A2(4KL)
950° C x no dwell time (100mg abs)	-9(6)	9(4)
850° C x 2 h (50 mg abs)	-3(3)	3(3)
1000° C x 2 h (50 mg abs)	0(3)	0(3)

From Table 4.8 the fractional areas for component 1 (singlet) and component 2 (quadrupole doublet) were found to be similar between the two 76 K measurements (to within the uncertainties listed). However, the total area has decreased from 0.58(4) to 0.51(2) mm/s, which may be an indication of an overall lowering of the recoilless fraction of the sample after a two month period at room temperature. Note that the quadrupole splitting has also decreased. Thus, some room temperature annealing may be taking place. It was also found that the Sn sites present for this sample were similar to those for the x=0.22 sample (amorphous Sn sites are similar as shown in Table 4.1).

Based on the x=0.22 study, it was assumed that DX center formation should not occur until much higher annealing temperatures (>850° C), therefore the first heat treatment for this sample was at 950°C x no dwell time. The fit was similar to that for the annealed

Table 4.10 X=0.25 area, source recoilless fraction ratios and Debye temperatures. Here K_{4K}/K_{76K} =1.032 for the 50 mg absorber and 1.029 for the 100 mg one. For f_s ratio ≥1, an estimate of the Debye temperatures were arrived at by using the lower error limit in the f_s ratios.

Treatment	**Condition ratio**	**A1(76K)/ A1(4K)**	**A2(76K)/ A2(4K)**	**f_{s1}(76K)/ f_{s1}(4K) Θ (K)**	**f_{s2}(76K)/ f_{s2}(4K) Θ (K)**
950°C x no dwell	D/D (50 mg)	0.61(5)	1.38(70)	0.63(5) 134(11)	1.38(70) >153
	D/D (100 mg)	0.7(1)	0.8(1)	0.7(1) 151(22)	0.8(1) 181(52)
	D/L (100 mg)	0.67(8)	1.15(20)	0.69(8) 149(17)	1.15(20) >322
850°C x 2h	D/D (50 mg)	0.77(2)	0.84(8)	0.79(2) 181(5)	0.87(8) 223(75)
	D/L (50 mg)	0.75(2)	1.1(2)	0.77(2) 172(4)	1.1(2) >243
1000°C x 2h	D/D (50 mg)	0.90(3)	0.50(4)	0.93(3) 263(20)	0.52(4) 120(9)
	D/L (50 mg)	0.90(3)	0.50(4)	0.93(3) 263(20)	0.52(4) 120(9)

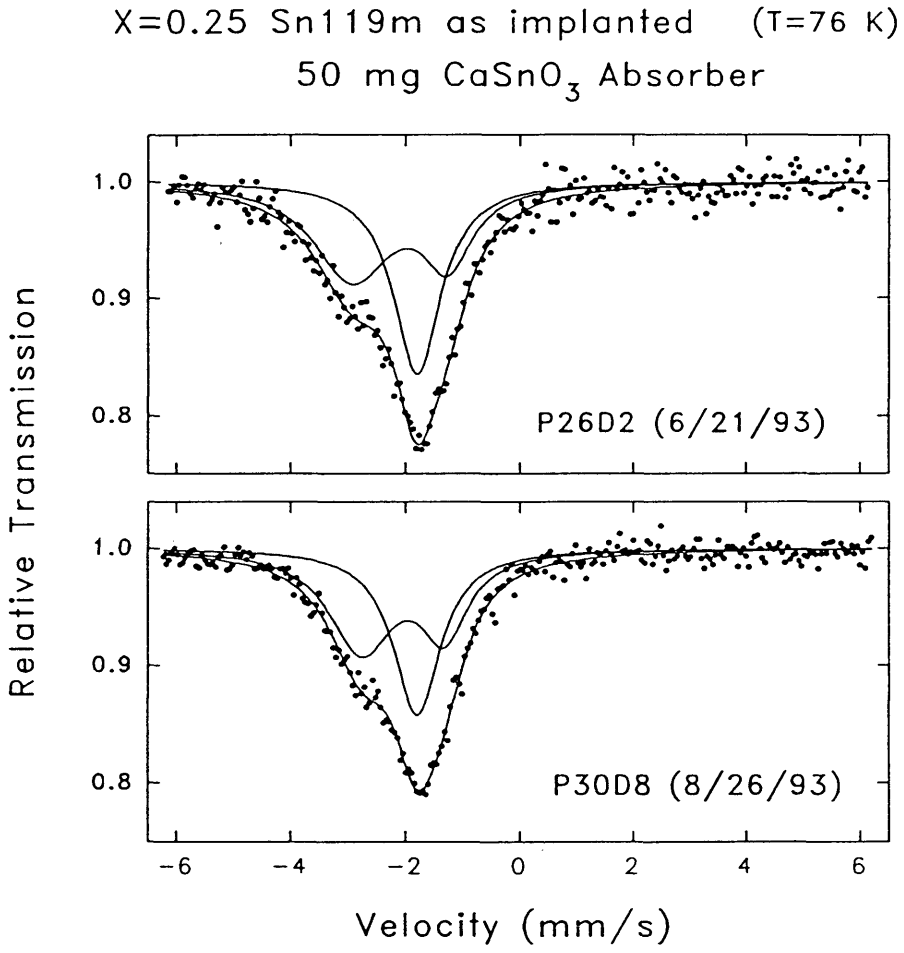

Figure 4.12 X=0.25 Mössbauer data for the as-implanted case measured two months apart.

cases for x=0.22. Figures 4.13 and 4.14 show the Mössbauer spectra for this heat treatment, using 50 mg and 100 mg absorbers, respectively. The use of a 100 mg absorber allowed better signal to noise in the data to compensate for loss of Sn (as documented later), however, the fits required a slightly larger linewidth (1.15 mm/s, fixed) which causes the 2 components to be less resolved. From Table 4.9 the dark-light change in fractional areas (100 mg absorber) was found to be -9(6)% for component 1 and 9(4)% for component 2 which is consistent with PPC behavior. The average Debye temperatures for components 1 and 2 (from Table 4.10) were 145(10) K and ≥218(23) K. The Debye temperature for component 1 is anomolously low (compared to a Sn_{Ga} site). It is unknown what other factors may have caused this. Component 2 was attributed to neutral Sn and DX centers, to within the uncertainty of the measurement.

Because evidence of PPC was found for the 950°C x no dwell time heat treatment in Table 4.9, a constant velocity measurement was performed. These results are presented in Figure 4.15 and Table 4.11. The change in count rate from the dark to light at -1.8 and -2.6 mm/s were 1.5(1.0) % and -1.4(1.0) %, respectively. The change in the count rate for the δ=-1.8 mm/s component is opposite of what is expected for PPC behavior. That is, the amount of Sn in the assumed δ=-1.8 mm/s substitutional site seems to increase in relative transmission while that of the δ=-2.6 mm/s component is consistent with PPC behavior (the increase in the count rate corresponds to a decrease in the effect) where the DX centers are emptied from the δ=-2.6 mm/s site to a site other than the δ= -1.8 mm/s site, possibly unresolved from the -2.6 mm/s component.

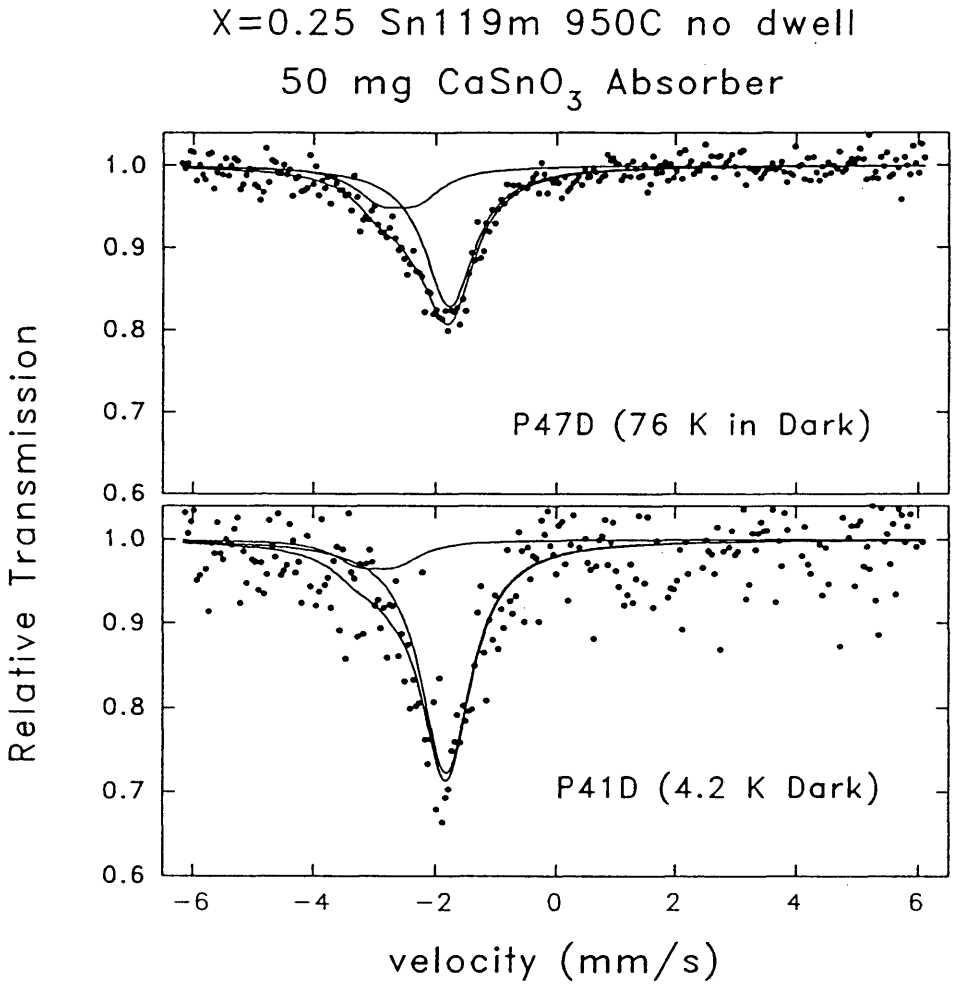

Figure 4.13 X=0.25 Mössbauer data for the 950°C x no dwell time heat treatment (50 mg absorber).

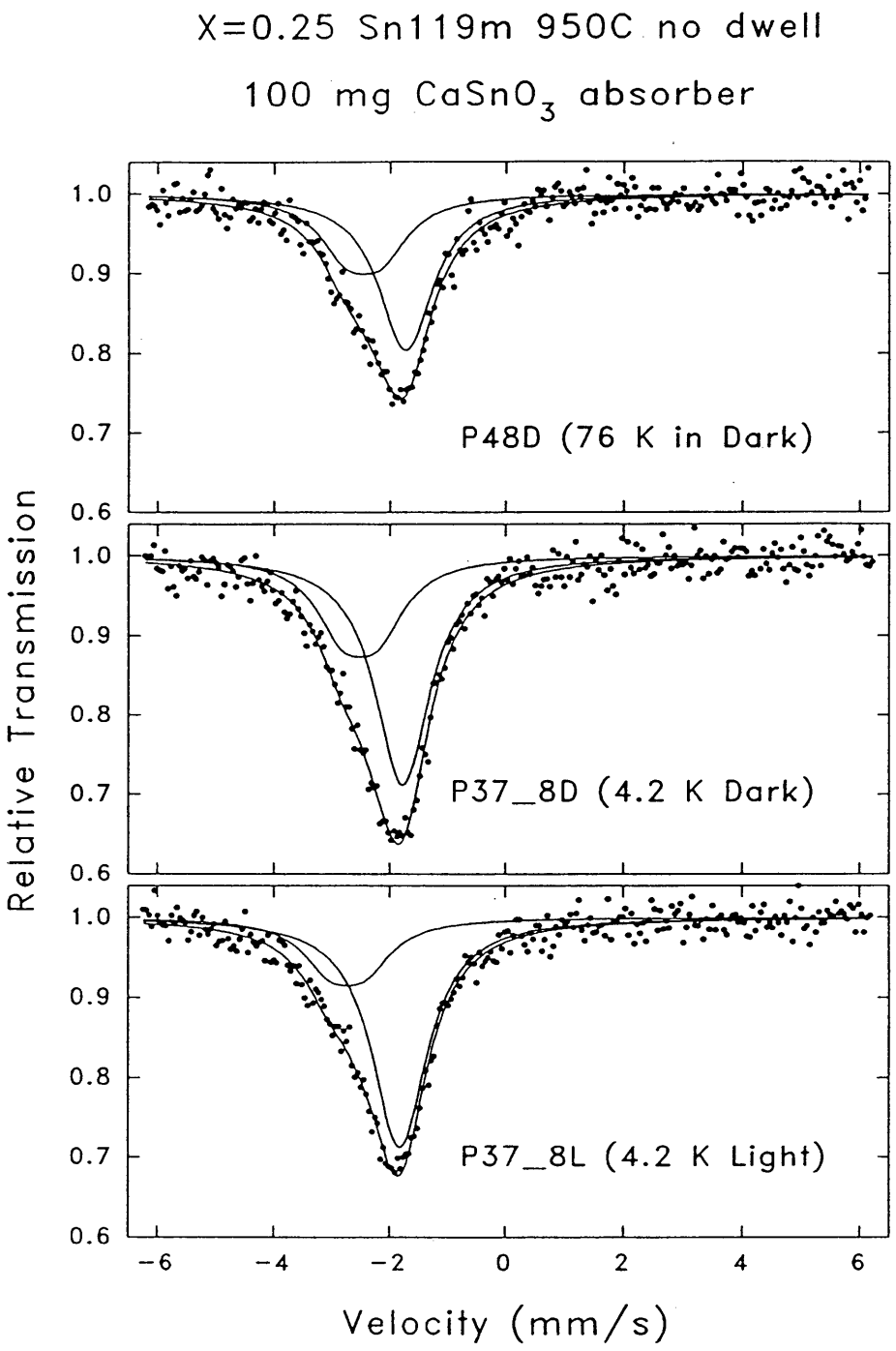

Figure 4.14 X=0.25 Mössbauer data for the 950°C x no dwell time heat treatment (100 mg absorber).

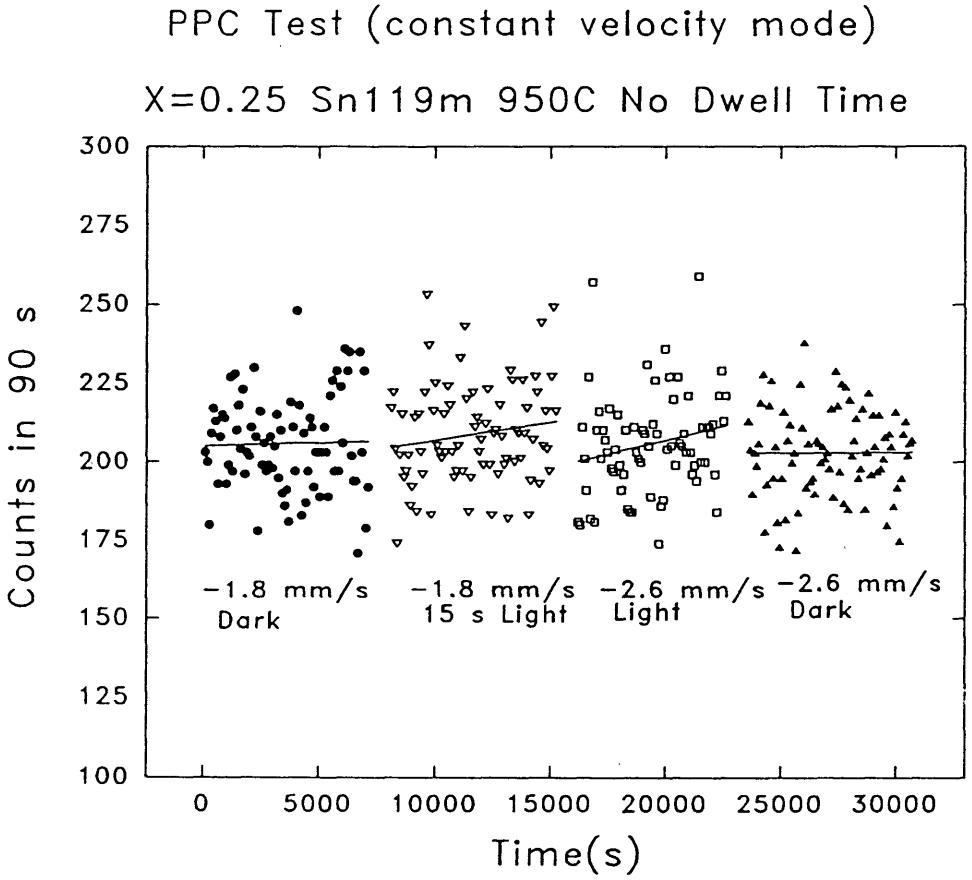

Figure 4.15 X=0.25 results of the constant velocity mode measurement for the 950°C x no dwell time heat treatment.

Table 4.11 X=0.25 constant velocity mode data at 4K for the 950°C x no dwell time heat treatment.

Velocity (mm/s)	Condition	Total Count	Average Count (per 90 s)	Linear Regression
-1.8	DARK	16261(128)	205.8(16)	ao=205(4) a1=0.0002(8)
-1.8	LIGHT	16702(129)	208.8(16)	ao=195(10) a1=0.0012(9)
-2.6	LIGHT	14823(122)	205.9(17)	ao=172(20) a1=0.002(1)
-2.6	DARK	16237(127)	203.0(16)	ao=202(21) a1=0.00003(75)

Figures 4.16 and 4.17 show the effects of annealing at 850 and 1000°C x 2 h (furnace cooled) with overpressures of Ga and Al from high purity metals. The fit of the Mössbauer spectra was different for this case: the quadrupole doublet was fixed to $\delta 2$=-2.6 mm/s and Δ=0.6 mm/s and $\delta 1$=-1.8 mm/s remained freed. The linewidths of both components were fixed to 1.3 mm/s. This was required to produced a reasonable χ^2 value. The equilibrium vapor pressures (from specification sheets published by RCA, 1962) of Ga at 850 and 1000°C are $3x10^{-5}$ and 10^{-3} Torr, respectively. For Al, the vapor pressures are $5x10^{-6}$ and $2x10^{-4}$ Torr, respectively. These allowed for Al mole fraction ratios of 0.14 and 0.17 at 850 and 1000°C, respectively. This heat treatment was performed to determine if any Ga and/or Al vacancies created by the previous treatment

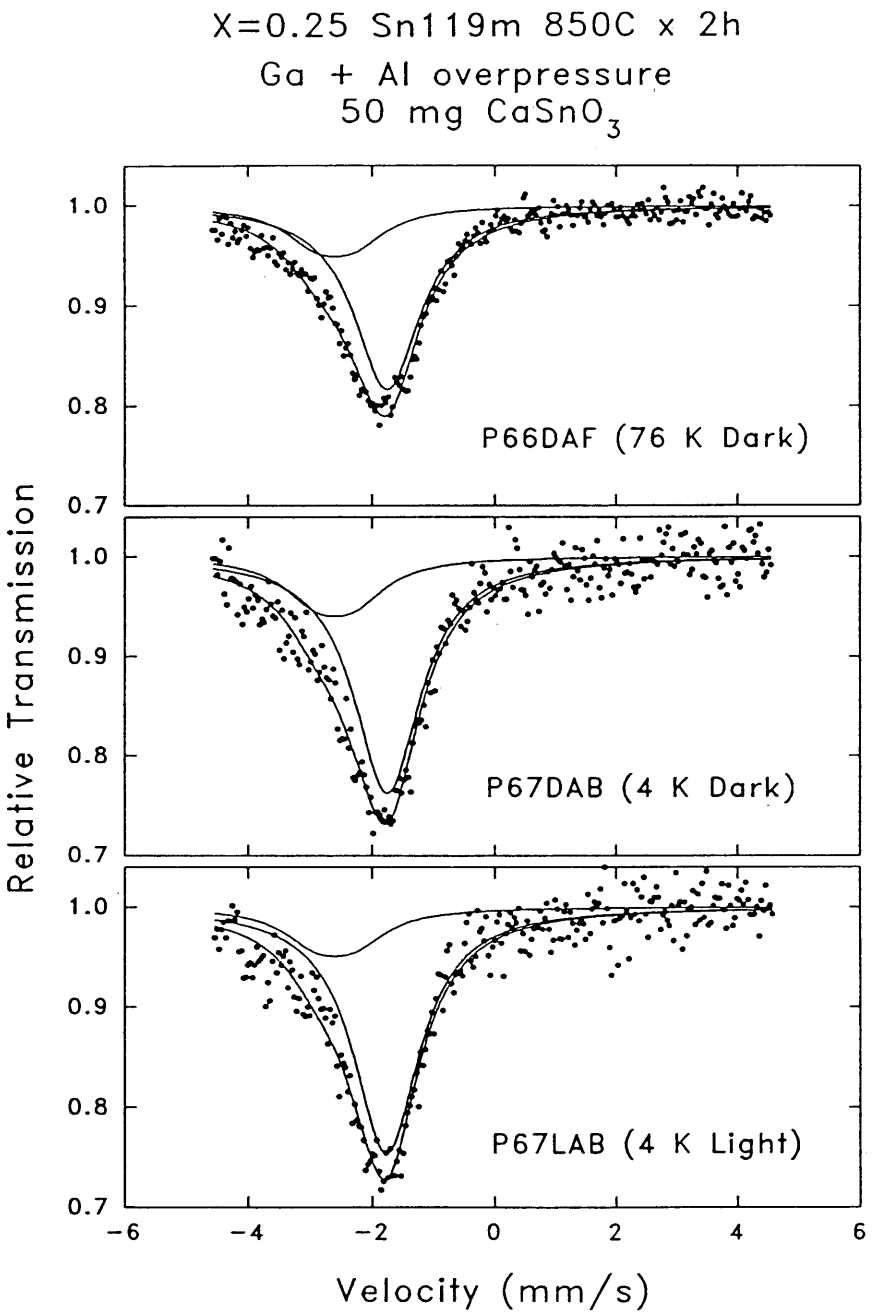

Figure 4.16 X=0.25 Mössbauer data for the 850°C x 2 h with Ga+Al overpressure case (50 mg $CaSnO_3$ absorber)

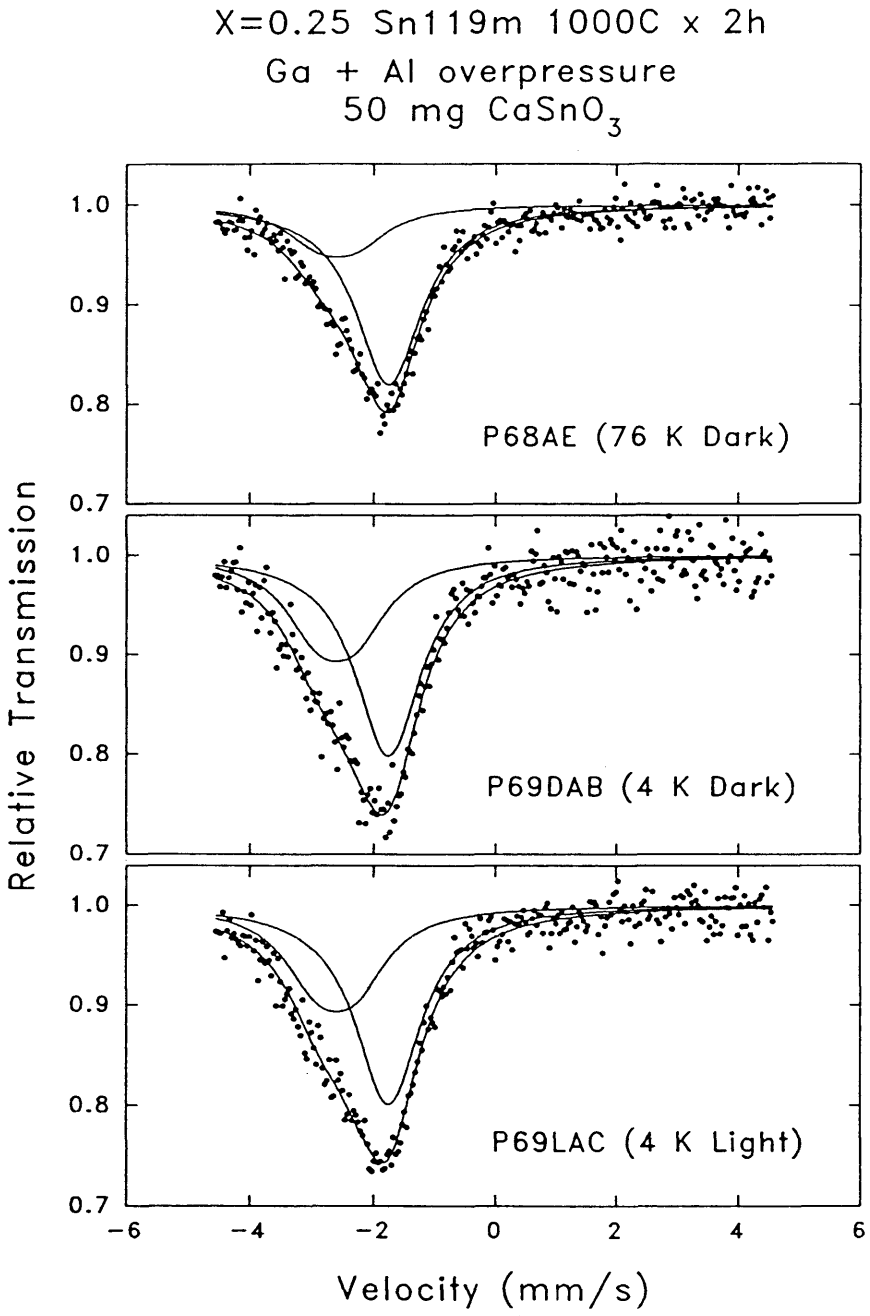

Figure 4.17 X=0.25 Mössbauer data for the 1000°C x 2 h with Ga+Al overpressure case (50 mg $CaSnO_3$ absorber).

could be removed by the diffusion of these species from the vapor state, through the SiO_2 capping layer, into the sample and possibly lower the diffusivity of Sn by removing these vacancies. Note also that the velocity scale has changed from ±6.0 mm/s to ±4.5 mm/s. This allowed for improved resolution in the spectra (in that more channels will define the resonance) as well as a higher count rate per channel. Hence, the use of the 50 mg absorber is sufficient for good signal-to-noise.

From the Mössbauer data (Table 4.8) it is observed that the relative fractional areas at 76 K (50 mg absorber) did not change significantly for the 950°C x no dwell time, 850°C and 1000°C x 2 h heat treatments. However, at 4 K (dark) the area of component 1 decreased while that of component 2 increased as annealing progressed from 950°C x no dwell time to 1000°C x 2h. This was correlated to an increase in the Debye temperature as a function of annealing temperature, as seen in Table 4.10. The average Debye temperature for component 1 has increased from 144(10) K to 263(20) K while that of component 2 decreased from ≥218(10) K to 120(9) K, however, a large error in the Debye temperature was found for the 850°C x 2 h min anneal [223(75) K].

Fitting the data with a larger linewidth (1.3 mm/s) for the 850 and 1000°C heat treatments may also indicate a larger distribution of isomer shifts, possibly due to Al(Ga) alloy disorder accompanied by the Ga+Al overpressure.

Table 4.12 shows the count rate of the sample as a function of heat treatment. Comparing the decrease in count rate from the as-implanted case to the 950°C x no dwell time case (2.1 c/s) to that between this and the count rate after annealing at 1000°C x 2h

Table 4.12 Sample count rate (activity) as a function of anneal temperature for x=0.25.

Heat treatment	Count rate (counts/s)
as-implanted	5.0
950°C x no dwell time	2.9
850°C x 2 h under Ga+Al overpressure	2.4
1000°C x 2 h under Ga+Al overpressure	2.1

(0.8 c/s), it is clear that the combination of Ga+Al overpressure and furnace cooling reduces the loss of Sn through the SiO_2 significantly. This suggests that the addition of Ga+Al metal can reduce the $V_{Ga(Al)}$ concentration in the sample, hence lowering the Sn diffusivity. As with the x=0.22 sample, no signal due to a Sn^{2+} site (Sn-oxygen complex in the capping layer) was observed in the Mössbauer spectra.

A resistance test similar to that for x=0.22 was made on the x=0.25 sample after annealing at 1000°C x 2 h. At 4 K R_{DARK}=1192(6) Ω and R_{LIGHT}=277(1) Ω (a 77% change) where the illumination was 15 s @ 60 mA LED current. After illumination the resistance remained at ~277 Ω for 3 h, clear proof that PPC was found in this sample. Hall measurements (van der Pauw geometry) performed at NREL were utilized to obtain values of the mobility (μ), the sheet carrier concentration (n_{sheet}) and the sheet resistivity (ρ_{sheet}) in the dark and light. Table 4.13 lists these values in the dark (D) and light (L), 15s 60 mA LED at 20 and 76K.

Table 4.13 Data from Hall measurement on x=0.25 after 1000°C x 2 h. The difference between the dark and light carrier concentrations is assumed to be due to DX centers. (a) average sheet values at 20 K (b) sheet values at 76 K.

(a)

Parameter	Dark	Light
μ (cm^2/V-s)	113	75
n_{sheet} (cm^{-2})	$3.3x10^{14}$	$4.5x10^{14}$
ρ_{sheet} (ohm/□)	169	185
$^{DX}n_{sheet}$ (cm^{-2})	$1.2x10^{14}$	

(b)

Parameter	Dark	Light
μ (cm^2/V-s)	113	94
n_{sheet} (cm^{-2})	$3.3x10^{14}$	$4.3x10^{14}$
ρ_{sheet} (ohm/□)	169	155
$^{DX}n_{sheet}$ (cm^{-2})	$1.0x10^{14}$	

From the 20 K data in Table 4.13(a) the mobility changed by -34% going from dark to light, the sheet carrier concentration by +36% and the sheet resistivity by +9.5%. The discrepancy between the 77% change in the resistance and the 36% change in the sheet carrier concentration is probably contact related, since the contact material was In-2% Sn, i.e., the Sn from the contacts may have produced locally high concentrations of DX

centers during contact formation (450°C x 5 min). That is, when probing the PPC behavior via two-probe resistance measurements, contact resistance is also included. Since this contact resistance is attributed to the In and Sn from the ohmic contact alloying with the AlGaAs, it is possible that any illumination in this contact region can affect its resistance. In this case the resistance tended to decrease due to possible Sn DX centers being photo-excited in the contact region. The 76 K data in Table 4.13(b) shows the changes, from dark to light, in mobility, sheet carrier concentration and sheet resistivity to be -17%, +30% and -8%, respectively.

Notice that the DX sheet concentration ($^{DX}n_{sheet}$) at 20 K was $1.2x10^{14}$ cm^{-2}, a factor of 3.5 larger than the Sn implantation dose ($4.5x10^{13}$ cm^{-2}). This suggests that other n-type donors were present which exhibit DX behavior, i.e. Si from the SiO_2 capping layer diffusing into the sample due to annealing. At 76 K the $^{DX}n_{sheet}$ was $1.0x10^{14}$ cm^{-2}, which is $2x10^{13}$ cm^{-2} less than the 20 K value. Since the capture energy for Si DX is 0.33 eV while that of Sn DX is <0.1 eV (Lang and Logan 1979), the PPC effect observed at 76 K should be mostly due to Si DX centers. At 20 K both Sn and Si should contribute to the PPC effect. The difference between the 20 K and 76 K DX sheet electron concentrations being $2x10^{13}$ cm^{-2} may be due to electrons localized at Sn DX centers. The dark sheet carrier concentration being $3.3x10^{14}$ cm^{-2} for both 20 and 76 K may suggest that not all of the Si and Sn in the sample had their electrons localized at DX centers, but rather contributed electrons to the conduction band. Native defects such as V_{As} and As_{Ga} are deep donors and should not contribute to the n conductivity at low

temperatures.

Assuming that the Sn sheet concentration is approximately $4.5x10^{13}$ Sn/cm^2 and that $2x10^{13}$ electrons/cm^2 (assumed from Sn) are localized at Sn DX centers, then the fraction of Sn as DX centers is about 44, 22 and 15% for 1, 2 and 3 electron DX centers. A corresponding change would have been easily seen in the A1(4KD)-A1(4KL) Mössbauer data in Table 4.9. This may suggest that a lattice relaxation occurred on a non-nearest-neighbor site. However, since the Mössbauer data represents only ^{119m}Sn (0.23% of the total Sn, from section 4.3), radiation-induced capture, as discussed in sec. 4.2, may have prevented the change from being seen.

4.4.3 Absorber experiment (x=0.15)

During the absorber measurement a small piece of the same material (un-lapped and un-etched) with two ohmic contacts was placed adjacent to the absorber on the Pb mask such that it was exposed to both the γ-ray source and the LED. This was used as a PPC monitor by measuring the resistance at 76 K in the dark and at 4 K in the dark and light. During the acquisition of the x=0.15 Mössbauer data (>40 days) the PPC monitor's resistance (measured at 4K) increased somewhat linearly: $R_{4K(DARK)}$=2.142t+184.5 Ω and $R_{4K(LIGHT)}$=1.923t-151.2 Ω, where t is the time in days. The percent change in resistance from the dark to light remained between 18% (start of data acquisition) and 15% (after 50 days) and was persistent for at least 24 h. Since the PPC monitor was also exposed to the γ-ray source ($CaSnO_3$) the increase in resistance over time may be due to

radiation-induced defects from 24 keV γ-rays. These defects may have changed the electron mobility (μ), since the resistance is proportional to $(\mu ne)^{-1}$. No photo-excitation of the DX centers due to the 24 keV γ-rays was observed (over a 24 h period the dark resistance did not change by more than 1%).

Hall data obtained on a similarly doped sample (x=0.23) showed the carrier mobility to be constant (~1000 cm^2/V-s) with respect to temperature and did not change upon illumination at 10 K. It was assumed that the same held true for the x=0.15 sample since the change in resistance (~ 17%) is close to the change in the carrier concentration (~10%) and that the 7% discrepancy may by contact related. Conflicting results were found in the literature pertaining to the change in mobility with respect to illumination in III-V compounds, most likely due to dependence on the value of x, doping levels, and growth method (Skierbiszewski et al 1993, Oh et al 1993, Ghezzi and Parisini 1993, Subramanian et al 1993, Baraldi et al 1991, Kim et al 1991). Normally the DX center is resonant with the conduction band for x<0.22, however, under heavy doping conditions ($\geq 10^{18}$ cm^{-3}) the DX center is stabilized and PPC can be observed. That is, the Fermi level approaches the DX level (Theis et al 1988). This is clearly observed here for x=0.15.

Tables 4.14 and 4.15 show the Mössbauer fit parameters and percent change in fractional area at 4 K in the dark and light, respectively.

Table 4.16 shows the fractional area, recoilless fraction ratios for the 3 components and the Debye temperatures for component 1. The other two components were too weak to determine their Debye temperatures Here, the same concept was used to determine the

recoilless fraction ratio for the absorber using the relation $A=0.5\pi f_s\Gamma_o K(T)$ and assuming a thin absorber, such that $K(T)=n_a f_a \sigma_o at$, then $A=0.5\pi f_s\Gamma_o n_a f_a \sigma_o at$, where A is the experimental area of the component measured, f_s is the source recoilless fraction, Γ_o is the natural ^{119}Sn linewidth (0.321 mm/s), n_a is the Sn/cm^3 in the sample, f_a is the absorber recoilless fraction, σ_o is the cross-section for resonant absorption, a is the fractional ^{119}Sn abundance (=0.86 for the x=0.15 absorber) and t is the thickness of the sample. Taking the ratio between 76 K and 4 K and solving for the absorber recoilless fraction reduces to $f_a(76K)/f_a(4K)=[A(76K)/A(4K)][f_s(4K)/f_s(76K)]$. The source recoilless fraction ratio (4K/76K) is 0.868(26)/0.824(24) =1.053(44) which was derived from the room temperature recoilless fraction for $CaSnO_3$ (Robinson 1981) using DEBYE.EXE.

Figure 4.18 show the Mössbauer data for the x=0.15 absorber at T=76 K and at T=4K in the dark and light (>35 s @60 mA LED). Note that in the absorber experiments the isomer shifts change sign relative to the source experiments. The spectra were consistently fitted with 3 components: a singlet at δ=1.8 mm/s (freed) with fixed linewidth W1=0.85 mm/s, which was the expected linewidth for the substitutional site in a thin absorber (Gibart et al 1989 and 1990); a doublet fixed at δ=2.6 mm/s with fixed linewidth W2=1 mm/s, fixed width and intensity ratios (set to 1) and fixed quadrupole splitting Δ=0.6 mm/s (assumed to be due to the Sn DX center); a singlet at δ=0.0 mm/s (fixed) with fixed linewidth W3=1 mm/s. The linewidths of components 2 and 3 were fixed at 1.0 mm/s since they were weak and that the NORMOS fitting program may try to fit these with larger linewidths (or different isomer shifts) which could interfere with

Table 4.14 Mössbauer parameters for the x=0.15 absorber. The widths were fixed at W1=0.85 mm/s, W2=W3=1.0 and the W and D ratios fixed to 1. The isomer shifts δ2 and δ3 were fixed to 2.6 and 0 mm/s, respectively.

RUN	COND.	D1	δ1	D2	D3	χ^2	A1	A2	A3	ATOT
P63AD	76K D	0.48(1)	1.77(1)	0.008(8)	0.04(1)	0.85	0.0064(2) 88(3)	0.0003(3) 4(4)	0.0006(2) 8(3)	0.0073(2)
P64DAF	4K D	0.57(1)	1.80(1)	0.014(8)	0.06(1)	1.11	0.0076(2) 85(2)	0.0005(2) 5(2)	0.0009(2) 10(2)	0.0090(2)
P64LAE	4K L	0.60(1)	1.82(2)	0.024(8)	0.06(1)	0.83	0.0080(2) 83(2)	0.0008(2) 8(2)	0.0009(2) 9(2)	0.0097(2)
P51AE	76 K D	0.45(2)	1.84(2)	0.004(7)	0(6x10^{-2})	1.28	0.0061(3) 98(6)	0.0001(2) 2(3)	0(9x10^{-4}) 0(15)	0.0062(3)
P52DAK	4K D	0.53(2)	1.83(2)	0.03(1)	0.005(9)	1.04	0.0071(2) 87(4)	0.0009(3) 12(4)	7x10^{-5} (1x10^{-4}) 1(1)	0.0081(2)
P52LAK	4K L	0.55(2)	1.80(2)	0.01(1)	0.002(11)	1.13	0.0073(2) 95(4)	0.0004(3) 5(4)	0(2x10^{-4}) 0(3)	0.0077(2)

Table 4.15 The percent change in the fractional areas between the light (L) and the dark (D) at 4 K for the x=0.15 absorber for the 3 components fitted.

RUN	A1(4KD)-A1(4KL)	A2(4KD)-A2(4KL)	A3(4KD)-A3(4KL)
P64	2(3)	-3(3)	1(3)
P52	-8(6)	7(6)	1(3)
Average of P64 and P52	-3(3)	2(3)	1(2)

Table 4.16 Fractional area, recoilless fraction ratios for the 3 components and the Debye temperatures for the substitutional Sn component where A(76K)/A(4K)=1.053(44)[f_s(4K)/f_s(76K)].

RUN RATIO	A1(76K)/ A1(4K)	A2(76K)/ A2(4K)	A3(76K)/ A3(4K)	f_{a1}(76K)/ f_{a1}(4K) Θ_D (K)
P63AD/P64DAF	0.84(3)	0.6(6)	0.7(3)	0.88(5) 230(13)
P63AD/P64LAE	0.80(3)	0.4(4)	0.7(3)	0.84(5) 200(12)
P51AE/P52DAK	0.86(5)	0.1(2)	-	0.91(5) 256(14)
P51AE/P52LAK	0.84(5)	0.3(5)	-	0.88(6) 230(16)

the substitutional site at δ=1.8 mm/s.

Two sets of data were acquired: the P63-64 data set is folded data (256 channels) for the velocity range of ±4.5 mm/s while that of the P51-52 data set represents a velocity range of ±6.0 mm/s and is the first half of the 512 channel unfolded data. It was found that the second half of this data set was distorted, due to a mechanical instability in the drive unit.

The average Debye temperature for component 1 in Table 4.16 closely represents the substitutional Sn site; component 2 is extremely weak, showing that the Sn-doped layer has little in the way of Sn DX centers, Sn precipitates and compensating Sn complexes;

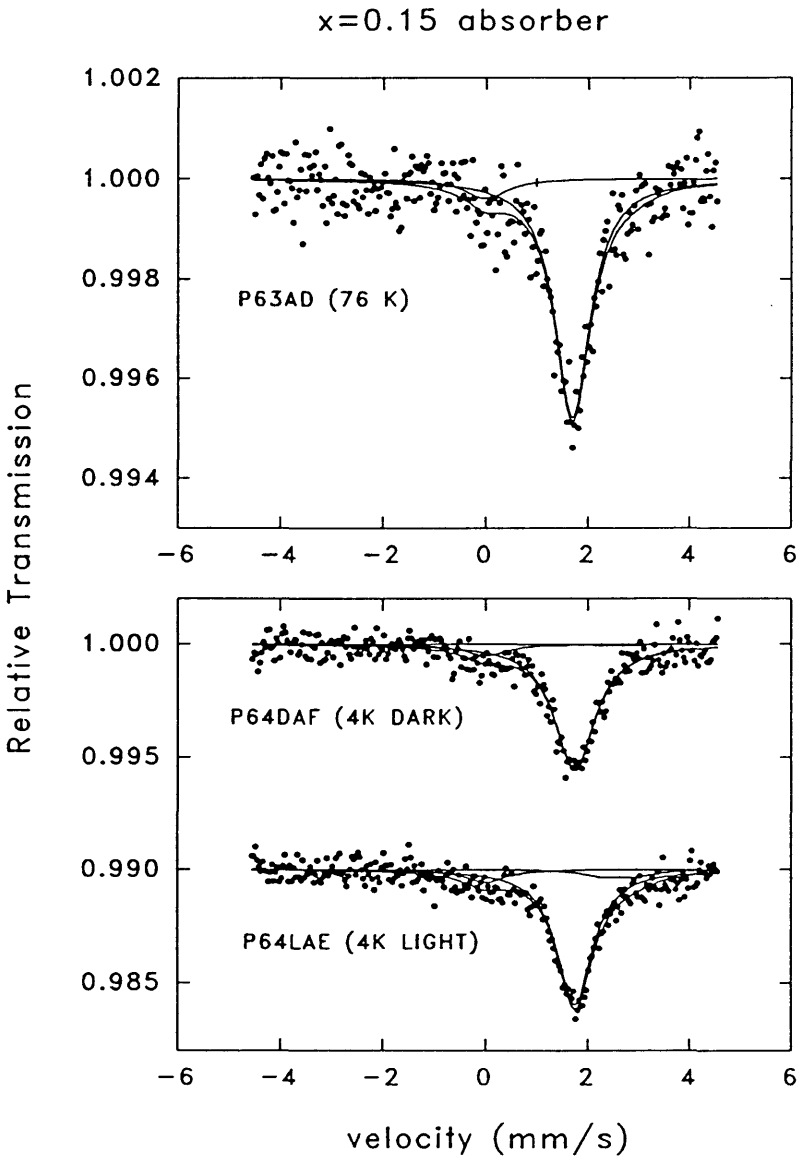

Figure 4.18 X=0.15 Mössbauer data taken at 76 K (top) and 4 K dark and under >35 s (I_{LED}= 60 mA) illumination (bottom).

component 3 could be a Sn^{2+} (Sn-oxygen complex) site (δ~0.0 mm/s) such as that found in a powdered absorber studied by Glick (1992) with a Debye temperature of 75 K. This complex was possibly formed during the sample etching or may have been incorporated into the sample during growth. Pant et al (1993) have found evidence of a short nearest neighbor distance which may be related to the Sn-O complex in x=0.23 AlGaAs using EXAFS.

The total Sn concentration can be estimated by using the calculated area for component 1 at 76 K (A1=.0064(2) mm/s for run P63AD). Using a relation from Williamson (1986) where the concentration (in cm^{-3}) for component i is $n_i=2.54x10^{18}(A_i/tf_i)$, where A_i, f_i, and t are the area fraction, recoilless fraction and sample thickness, for component i, respectively. In this case, A_i=0.0064 mm/s, t= $142x10^{-4}$ cm and f_i is ~0.73 (derived from the 230 K Debye temperature in Table 4.16 using DEBYE.EXE) resulting in $n=1.6x10^{18}$ cm^{-3} on the substitutional site. Since this site represents ~88% of the total spectrum, the total Sn concentration is $\sim 1.6x10^{18}/(0.88)=1.8x10^{18}$ Sn/cm^3. This agrees well with the designed doping level of $2x10^{18}$ and the total carrier concentration determined by Hall measurements in the dark and light: $2.0x10^{18}$ and $2.2x10^{18}$ cm^{-3}, respectively. The change in the carrier concentration for this sample was therefore $2x10^{17}$ cm^{-3} from dark to light (i.e. 10%), and the expected fraction of Sn as *one*-electron DX centers is also ~10% $[100*(2x10^{17}/1.8x10^{18})]$. For 2 and 3 electron DX centers, the expected fractions are ~5% and ~3.3%, respectively. These would also correspond to increases in the percent

fractional area (Table 4.15) of the substitutional site by the same amounts, upon illumination. Table 4.15 shows that the average value for the change in fractional area of component 1 to be -3(3)%, consistent only with the 3 electron model.

4.4.4 Comments on the source and absorber experiments

The average value of freed isomer shifts (initially set to $\delta 1$=-1.8 and $\delta 2$=-2.6 mm/s) in the annealed cases for the x=0.22 and x=0.25 samples (from Tables 4.3 and 4.8) were found to be: $\delta 1$=-1.883(3), $\delta 2$=-2.787(3) mm/s and $\delta 1$=-1.855(6) mm/s, $\delta 2$=-2.74(7) mm/s, respectively. Note that the isomer shifts were shifted to larger negative velocities in the x=0.22 sample. It is unknown if this was caused by an artifact in the method used to fit the two poorly resolved components in the spectra or if it is due to physical differences in the two samples such as the different x values or the different Sn doses.

The existence of DX centers, through the observation of PPC via Hall measurements, was found to exist in the x=0.25 source sample (1000°C x 2 h heat treatment) and in the x=0.15 absorber sample. However, conclusive evidence of the DX center (changes in the fractional areas attributed to the PPC effect) was lacking in the Mössbauer data analysis. The next section describes an atomic-scale model for the DX center based on these findings.

4.5 Proposed atomic-scale model

The fact that PPC was found for the x=0.25 sample from the Hall measurement and that there was no evidence of any PPC-induced change in the x=0.25 and 0.15 samples (by Mössbauer spectroscopy), suggests that the atomic-scale structure of the DX centers present in the samples may be different than that of the broken-bond configuration proposed by Chadi and Chang, which represents a drastic change in nearest neighbor configuration.

The Mössbauer observation for x=0.15 is also consistent with what was found for Sn-doped x=0.23 (similar to x=0.15 in doping) and prepared by the same group in France studied by EXAFS (Lurio et al 1994), that is, no nearest neighbor lattice relaxation was observed. This also suggests that a *next* nearest neighbor of the Sn atom may undergo a lattice relaxation, which cannot be observed by Mössbauer spectroscopy or EXAFS.

A model such as that given by Van Vechten (1985), where the DX center is represented by the defect $Sn_{Ga(Al)}^{+}\ V_{III}^{-}\ Al_{As}^{-2}$, seems to reconcile the data since it predicts that the vacancy (which may undergo a lattice relaxation) lies on a non-nearest-neighbor site to the Sn *and* it can localize 3 electrons. In this model the $Sn_{Ga(Al)}^{+}$ is the substitutional donor on a group III site, V_{III}^{-} is a negatively charged vacancy on a non-nearest-neighbor group III site to the donor and Al_{As}^{-2} is a near-neighbor antisite to the V_{III}^{-}.

The recent positron-annihilation study by Mäkinen et al (1993) also confirms the existence of a vacancy related to the DX center. They found that the vacancy

concentration decreased to a level similar to that for undoped AlGaAs upon illumination in Si- and Sn-doped $Al_xGa_{1-x}As$ ($x \geq 0.18$). They have also interpreted this vacancy in terms of the broken-bond configuration of the DX center's ground state (Chadi-Chang model) where the Sn is in an off-substitutional site. However, the possibility exists that this vacancy, created by doping, can lie on a non-nearest-neighbor site to the substitutional dopant atom and undergo a lattice relaxation such that it cannot be detected by Mössbauer spectroscopy or EXAFS upon illumination.

Earlier ^{119}Sn Mössbauer absorber studies on GaAs:Sn under hydrostatic pressure and on $Al_xGa_{1-x}As$ with $0 \leq x \leq 1$ (Williamson and Gibart 1991, Gibart et al 1990 and Gibart et al 1988) showed strong evidence that the DX center localizes 2 or 3 electrons (negative-U type behavior) and that the quadrupole splitting ($\Delta \sim 0.4$-0.6 mm/s at $\delta = 2.6$ mm/s) represents an upper limit of the local distortion of cubic symmetry consistent with a lattice relaxation and possibly attributed to the Sn DX center. Another possible interpretation given was that the quadrupole split component in the alloys may be that of a range of isomer shifts representing a distribution of DX centers due to different (Al, Ga) environments. However, these studies were made in the dark and therefore no illumination results were reported whereas the results presented here show little evidence of a nearest neighbor lattice relaxation between the light and the dark.

A very recent Mössbauer source study on ^{129m}Te implanted $Al_{0.3}Ga_{0.7}As$ (Bemelmans et al 1994) showed that a portion of a quadrupole split component was transformed into a single line upon illumination at 4 K, which gradually relaxed back to the quadrupole

split state. The authors claim that this effect is an indication of DX centers which become substitutional donors upon illumination and in agreement with the Chadi and Chang broken-bond model.

The fact that ^{129m}Te (which decays to ^{129}I) resides on a group V site for n-type doping and that the Van Vechten model for the DX center contains a V_{III} (*nearest* neighbor to $Te(I)_{As}$) also reconciles the study by Bemelmans et al (1994) since $Te(I)_{As}^{+}$-V_{III}^{-} can introduce a quadrupole split component. Upon illumination a near neighbor lattice relaxation may be involved which allows the $Te(I)_{As}$ to reside in a cubic environment (single line), possibly due to V_{III} motion.

5. Conclusions

5.1 Summary

The thermal diffusion of Sn in $Al_xGa_{1-x}As$ was studied for x=0 and x=0.32 by SIMS and XRD under different arsenic overpressures, temperatures and sample geometries in evacuated and sealed quartz ampoules. Thin film capping layers of SiO_x and Si_xN_y were studied by XRD and AES to determine their usefulness in preserving the AlGaAs surface during thermal processing. Mössbauer studies on ^{119m}Sn-implanted, MBE-grown $Al_xGa_{1-x}As$ (x=0.22,0.25) sources and an MOVPE-grown $Al_{0.15}Ga_{0.85}As$ absorber were used to investigate the site occupation, electrical activation and any lattice relaxation associated with the DX center. From the data an atomic-scale model, based on a proposed model by Van Vechten (1985), was chosen.

Results from the Sn thermal diffusion study for x=0.32 shows enhanced Sn diffusion (by SIMS) when an As overpressure (~0.5 atm) was used as opposed to solely using the ambient vapor produced from the sample. The As_4 overpressure presumably created Ga (or Al) vacancies, by which the Sn diffuses. However, the addition of an As_4 overpressure created decomposition of the AlGaAs surface (as shown by XRD), independent of the cooling rate, whereas those which were slowly cooled under the ambient As_4 vapor remained undecomposed.

The use of 120 nm SiO_2 capping layers further preserved the surface of the AlGaAs, independent of the cooling rate used. Si_xN_y capping layers decomposed and peeled away from the AlGaAs while the SiO_2 films remained undecomposed and well-adhered after

850°C x 12 h anneals. The SiO_2 capping layers also were selected for the attempts to activate the ^{119m}Sn-implanted AlGaAs (Mössbauer source experiments) by high temperature annealing.

Mössbauer measurements of the systematically annealed ^{119m}Sn-implanted source samples showed no evidence of a PPC effect. This observation was explained in terms of the formation of Sn-vacancy complexes above 400°C which may have caused electrical compensation, γ-radiation-induced electron-capture of any excited ^{119m}Sn DX centers present in the sample which would mask any PPC effect in the Mössbauer data and/or a non-nearest-neighbor lattice relaxation. Resistance measurements on the x=0.22 sample, after annealing at 950°C x no dwell time, also showed little evidence of PPC. However, in the x=0.25 sample, after annealing at 1000° C x 2 h, under a Ga+Al overpressure, Hall measurements showed evidence of PPC by an increase in the carrier concentration upon illumination. A related change in the Sn site occupation, by 44, 22 or 15% (1, 2 or 3 electron DX centers) was not detected by Mössbauer spectroscopy, leading to the conclusion that there may be radiation-induced electron capture at the photo-excited ^{119m}Sn and/or that a non-nearest-neighbor lattice relaxation is involved. The source of the radiation-induced electron-capture is from the ^{119m}Sn to ^{119}Sn* transition (66 keV), which is highly internally converted and contributes to an Auger cascade, prior to the 24 keV γ-ray emission possibly causing local heating. Despite the presence of the SiO_2 capping layer none of the Sn which had diffused out of the sample remained with the oxide (no Mössbauer signal due to a Sn^{2+} site). The 850 and 1000°C x 2 h heat

treatments (furnace cooled) with a Ga+Al overpressure was shown to be a useful method of retaining the radioactive Sn in the sample as found by similar count rates after each heat treatment. This may be due to the removal of Ga and Al vacancies in the sample which lowered the Sn diffusivity. Higher temperature annealing also led to clear activation of Sn and Si DX centers as detected by photo-Hall measurements. The Si DX centers was attributed to Si diffusion from the SiO_2 capping layer into the sample.

Mössbauer measurements of the ^{119}Sn-doped, x=0.15 absorber indicated no change between the dark and the light at 4K, even though the *in situ* PPC monitor showed a resistance change of 15-18 % (carrier concentration change of 10 %) between these two states and was persistent for at least 24 h. A corresponding change in Sn site population of 10 % or, in the case of negative-U behavior, half of this change was not detected in the Mössbauer data. This suggests that the PPC effect may involve the lattice relaxation of a non-nearest-neighbor of the Sn which cannot be easily detected by Mössbauer spectroscopy due to its primary sensitivity to near-neighbor effects. A model, based on the atomic-scale structure of the DX center proposed by Van Vechten (1985) was invoked: $Sn_{Ga(Al)}{}^{+}V_{III}{}^{-}Al_{As}{}^{-2}$ where the group III-$Al_{As}{}^{-2}$ complex resides and possibly experiences a lattice relaxation in a non-nearest-neighbor environment with respect to the Sn donor and localizes 3 electrons. The atomic-scale model is also consistent with what was found for x=0.23 and 0.30 studied by EXAFS (Lurio et al 1994 and Hayes et al 1989), where no nearest neighbor relaxation was observed. Earlier ^{119}Sn Mössbauer absorber studies showed that the quadrupole split component at δ=2.6 mm/s and Δ~0.6

mm/s may be that of the ground state of the Sn DX center in a symmetry less than cubic with the quadrupole splitting providing an upper limit to the size of the local distortion involved (lattice relaxation). However, no measurements under light conditions were made so these new results raise a question about the earlier assignment. A recent ^{129m}Te source Mössbauer study on x=0.3 material showed changes in the spectrum between the dark and the light. This study is consistent with the Van Vechten model since Te_{As} is a nearest neighbor to the group III vacancy.

5.2 Suggestions for future work

The x=0.15 absorber sample was not an ideal sample for the accurate determination of PPC induced changes in the Mössbauer data. An ideal sample for these measurements should have an aluminum mole fraction of x=0.23, where maximum DX formation and therefore maximum PPC effect is expected. The x=0.23 layer should also be grown as close as possible to the thickness corresponding to the maximum signal-to-noise in the Mössbauer data (~ 150 μm). A growth method, such that the formation of Sn-O complexes is minimized, should be used. The Mössbauer data from this sample can be compared to the x=0.22 and 0.25 sources, presented in this work, for differences due to the highly internally converted ^{119m}Sn$\rightarrow$^{119}Sn* transition, which may affect the DX state and thus conclude if radiation-induced effects should be of any concern in the source experiments.

To avoid implant-induced damage in the AlGaAs layer, it would be interesting to

investigate the possibility of implanting the SiO_2 capping layers with ^{119m}Sn and use thermal diffusion techniques established here and in the literature to observe the Sn site occupation and possible DX activation, via Mössbauer spectroscopy, as a function of annealing temperature and atmospheric conditions (i.e. ambient or Ga+Al overpressures). A sensitive depth profiling technique (e.g. SIMS) could be used to monitor the Si, Sn and O concentrations in the samples and determine the extent of unintentional doping by Si. One should be aware of the fact that a SIMS system can be contaminated with ^{119m}Sn in this type of study. Therefore, proper precautions should be exercised.

6. References

Adachi, S., J. Appl. Phys. **58**, R1 (1985)

Allen, E..L., Murray, J.J., Deal, M.D., Plummer, J.D., Jones, K.S., Rubart, W.S., J. Electrochem. Soc. **138**, 3440 (1991)

Allsop, D.W.E., Solid State Phenomena **1-2**, 211 (1988)

Arnold, N., Schmitt, R., Heime, K., J. Phys. D: Appl. Phys. **17**, 43 (1984)

Arthur, J.R., J. Phys. Chem. Solids, **28**, 2257 (1967)

Baba, T., Mizuta, M., Fujisawa, T., Yoshino, J., Kukimoto, H., Jpn, J. Appl. Phys. **28**, L891 (1989)

Baliga, B.J., Ghandhi, S.K., J. Electrochem. Soc. **126**, 135 (1979)

Baraldi, A., Ghezzi, C., Parisini, A., Bossachi, A., Franchi, S., Appl. Surf. Sci. **50**, 405 (1991a)

Baraldi, A., Ghezzi, C., Parisini, A., Bossachi, A. Franchi, S., Phys. Rev. B **44**, 8713 (1991b)

Bemelmans, H., Borghs, G., Langouche, G., Nuc. Inst. Meth. Phys. Res. **B63**, 151 (1992)

Bemelmans, H., Borghs, G., Langouche, G., Phys. Rev. Lett. **72**, 856 (1994)

Biernacki, S.W., Physics Letters A **172**, 81 (1992)

Blood, P., Semicond. Sci. Technol. **1**, 7 (1986)

Brunkov, P.N., Evtikhiev, V.P., Konnikov, S.G., Kotel'nikov, E.Y., Papentsev, M.G., Sobolev, N.M., Sov. Phys. Semicond. **24**, 1230 (1990)

Bykov, G.A., Hien, P.Z., Sov. Phys. JETP **16**, 646 (1963)

Campbell, A.C., Dodabalapur, A., Crook, G.E., Streetman, B.G., Appl. Phys. Lett. **54**, 27 (1989)

Cargill III, G.S., Segmüller, A., Kuech, T.F., Theis, T.N., Phys. Rev. B **46**, 10078 (1992)

Carriere, T., Agius, B., Vickridge, I., Siejka, J., Alnot, P., J. Electrochem. Soc. **137**, 1582 (1990)

Chadi, D.J., Chang, K.J., Phys. Rev. Lett. **61**, 873 (1988)

Chadi, D.J., Chang, K.J., Phys. Rev. B **39**, 10063 (1989)

Chang, K.J., Cheong, B.H., Park, C.H., Solid State Commun. **84**, 1005 (1992)

Chadi, D.J., Phil. Trans. Roy. Soc. Lond. A **341**, 247 (1992)

Cheong, B.H., Vhang, K.J., Phys. Rev. B **46**, 13131 (1992)

Cho, J., Pawlowicz, L.M., Saha, N.C., J. Appl. Phys. **72**, 4172 (1992)

Cohen, R.M., J. Elec. Mat. **20**, 425 (1991)

Craford, M.G., Stillman, G.E., Rossi, A., Holonyak, Jr., N., Phys. Rev. **168**, 867 (1968)

Creek, E., Masters Thesis (T-4116), Colorado School of Mines, Golden, Colo., p. 21 (1992)

Davis, L.E., MacDonald, N.C., Palmberg, P.W., Riach, G.E., Weber, R.E., *Handbook of Auger Electron Spectroscopy*, 2nd ed., Physical Electronics Industries, Inc., Minnesota (1976)

Daya, S., Maaref, H., Bourgoin, J.C., Appl. Phys. Lett. **55**, 1407 (1989)

Deppe, D.G., Holonyak, Jr., N., Hsieh, K.C., Gavrilovic, P., Stutius, W., Williams, J., Appl. Phys. Lett. **51**, 581 (1987)

Dmochowski, Janusz, E., Dobaczewski, Lezek, Langer, Jerzy, M., Jantsch, Wolfgang, Phys. Rev. B **40**, 9671 (1989)

Dobaczewski, L., Kaczor, P., Phys. Rev. B **44**, 8621 (1991a)

Dobaczewski, L., Kaczor, P., Semicond. Sci. Technol. **6**, B51 (1991b)

Dobaczewski, L., Kaczor, P., Phys. Rev. Lett. **66**, 68 (1991c)

Dobaczewski, L., Kaczor, P., Zytkiewicz, Z.R., Missous, M., Saleemi, F., Dawson, P., Peaker, A.R., J. Appl. Phys. **72**, 3198 (1992)

Eisberg, R., Resnick, R., 1985, in *Quantum Physics of Atoms, Molecules, Solids, Nuclei, and Particles*, (John Wiley and Sons), p.580

Eriksson, S., Carlsson, P., Halmström, B., Uosaki, K.J., J. Electroanal. Chem. **337**, 217 (1992)

Etienne, B., Thierry-mieg, V., Appl. Phys. Lett. **52**, 1237 (1988)

Fane, R.W., Gross, A.J., Solid State Electronics **6**, 383 (1963)

Fockele, M., Spaeth, J.M., Gibart, P., in *Proceddings of the 20th International Conference on the Physics of Semiconductors*, ed. E.M. Anastassakis and J.D. Joannopoulus (World Scientific, Singapore, 1990), p. 517

Fujii, S., Shikata, S., Wei, L., Tanigawa, S., J. Appl. Phys., **72**(4), 1405 (1992)

Fujisawa, T., Yoshino, J., Kukimoto, H., Jpn. J. Appl. Phys., **29**(3), L388 (1990)

Ghezzi, C., Parisini, A., Semicond. Sci. Technol., **8**, 472 (1993)

Ghosh, S., Kumar, V., Phys. Rev. B, **46**(12), 7533 (1992)

Gibart, P., Wiliiamson, D.L., El Jani, B., Basmaji, P., Phys. Rev. B. **38**, 1885 (1988)

Gibart, P., Williamson, D.L., Moser, J., Basmaji, P., Phys. Rev. Lett. **65**, 1144 (1990)

Gill, S.S., Solid State Phenomena **1-2**, 281 (1988)

Glick, S.H., Masters Thesis (T-4097), Colorado School of Mines, Golden, Colo, p. 84 (1992)

Goldstein, B., Phys. Rev. **118**, 1024 (1960)

Goldstein, B., Keller, H., J. Appl. Phys. **32**, 1180 (1961)

Guido, L.J., Plano, W.E., Nam, D.W., Holonyak, Jr., N., Baker, J.E., Burnham, R.D., Gavrilovic, P., J. Electronic Mat. **17**, 53 (1988)

Hall, R.N., Fenner, G.E., Kingsley, J.D., Soltys, T.J., Carlson, R.O., Phys. Rev. Lett **9**, 366 (1962)

Haynes, T.E., Holland, O.W., Nuc. Inst. Meth. Phys. Res. **B59/60**, 1028 (1991)

Hayes, T.M., Williamson, D.L., Outzourhit, A., Small, P., Rudra, A., Physica B **158**, 581 (1989)

Henning, J.C.M., Ansems, J.P.M., Appl. Phys. A **44**, 245 (1987)

Hjalmarson, H.P., Drummond, T.J., Appl. Phys. Lett. **48**, 657 (1986)

Ho, H.P., Harrison, I., Baba-Ali, N., Tuck, B., Henini, M., J. Mat. Sci.:Mat. in Electronics. **2**, 137 (1991)

Holm, N.E., Weyer, G., J. Phys. C: Solid St. Phys. **13**, p.1109 (1980)

Hurle, D.T.J., J. Phys. Chem. Solids **40**, 639 (1979)

Ishikawa, T., Maeda, T., Kondo, K., Appl. Phys. Lett. **53**, 1926 (1988)

Jantsch, W., Wilamowski, Z., Ostermayer, G., Semicond. Sci. Technol. **6**, B47 (1991)

Jones, R., Öberg, S., Phys. Rev. B **44**, 3407 (1991)

Kajikawa, Y., J. Appl. Phys. **69**, 1429 (1991)

Katsumoto, S., Matsunaga, N., Yoshida, Y., Sugiyama, K., Kobayashi, S., Jpn. J. Appl. Phys. **29**, L1572 (1990)

Katayama, M., Tokuda, Y., Inoue, Y., Usami, A., Wada, T., J. Appl. Phys. **69**, 3541 (1991)

Kim, M.H., Plano, M.A., Haase, M.A., Stillman, G.E., Wang, W.I., J. Appl. Phys. **70**, 7425 (1991)

Kressel, H., Hawrylo, F.Z., Almeleh, N., J. Appl. Phys. **40**, 2248 (1969)

Lang, D.V., Logan, R.A., Phys. Rev. Lett. **39**, 635 (1977)

Lang, D.V., Logan, R.A., Jaros, M., Phys. Rev. B **19**, 1015 (1979)

Lang, D.V., Logan, R.A., in *Physics of Semiconductors 1978* (Inst. Phys. Conf. Ser. No. 43, 1979), 433

Langouche, G., Schroyen, D., Bemelmans, H., van Rossum, M., Deraedt, W., de Potter, M., Mat. Res. Symp. Proc. **104**, 527 (1988)

Langouche, G., Hyperfine. Inter. **47-48**, 85 (1989)

Langouche, G., Bemelmans, H., Odeurs, J., Borghs, G., de Potter, M., Deraedt, W., van Rossum, M., Mater. Sci. Forum **38-41** 1245 (1989)

Lee, S.T., Chen, S., Braunstein, G., Ko, K., Tan, T.Y., Nucl. Inst. Meth. Phys. Res. **B59/60**, 999 (1991)

Leith, G.A., Zukotynski, S., SpringThorpe, A.J., Appl. Phys. Lett. **60**, 2517 (1992)

Leszczński, M., Suski, T., Kowalski, G., Semicond. Sci. Technol. **6**, 59 (1991)

Li, M., Yu, P.Y., Solid State Commun. **61**, 13 (1987)

Li, M.F., Yu, P.Y., Shan, W., Hansen, W., Weber, E.R., Appl. Phys. Lett. **54**, 1344 (1989)

Llabador, Y., Friedt, J.M., Chem. Phys. Lett. **8**, 592 (1971)

Logan, R.A., Reinhart, F.K., J. Appl. Phys. **44**, 4172 (1973)

Lurio, L.B., Pant, J., Hayes, T.M., Williamson, D.L., Gibart, P., Theis, T.N., American Physical Society Abstracts Bulletin, **39**, 148 (1994)

Mäkinen, J., Laine, T., Saarinen, K., Houtojärvi, P., Corbel, C., Airaksinen, V.M., Gibart, P., Phys. Rev. Lett. **71**, 3154 (1993)

Mizuta, M., Kitano, T., Jpn. J. Appl. Phys. **26**, L1806 (1987)

Mizuta, M., Kitano, T., Appl. Phys. Lett. **52**, 126 (1988)

Mizuta, M., Tachikawa, M., Kukimoto, H., Minomura, S., Jpn, J. Appl. Phys. **24**, L143 (1985)

Mooney, P.M., Northrop, G.A., Morgan, T.N., Grimmeiss, H.G., Phys. Rev. B **37**, 8298 (1988)

Mooney, P.M., Theis, T.N., Wright, S.L., Appl. Phys. Lett. **53**, 2546 (1988)

Mooney, P.M., Wilkening, W., Kaufmann, U., Kuech, T.F., Phys. Rev. B **39**, 5554 (1989)

Moore, F.G., Dietrich, H.B., Dobisz, E.A., Holland, O.W., Appl. Phys. Lett. **57**, 911 (1990)

Moore, F.G., Dietrich, H.B., Nucl. Inst. Meth. Phys. Res. **B59/60**, 978 (1991)

Morgan, T.N., J. Elec. Mat. **20**, 63 (1991)

Mori, Y., Yokata, T., Ohkura, H., Jpn. J. Appl. Phys. **31** (pt. 2, no. 8), L1005 (1992)

Moriya, N., Brener, I., Halish, R., Pfeiffer, W., Deicher, M., Keller, R., Magerle, R., Recknagel, E., Skudlik, N., Wichert, Th., Wolf, H., J. Appl. Phys. **73**, 4248 (1993)

Mosser, V., Contreras, S., Robert, J.L., Piotrzkowski, R., Zawadzski, W., Rochette, J.F., Phys. Rev. Lett. **66**, 1737 (1991)

Mostefaoui, R., Chevallier, J., Jalil, A., Pesant, J.C., Tu, C.W., Kopf, R.F., J. Appl. Phys. **64**, 207 (1988)

Nabity, J.C., Stavola, M., Lopata, J., Dautremont-Smith, W.C., Tu, C.W., Pearton, S.J., Appl. Phys. Lett. **50**, 921 (1987)

Narayanamurti, V., Logan, R.A., Chin, M.A., Phys. Rev. Lett. **43**, 1536 (1979)

Nelson, R.J., Appl. Phys. Lett. **31**, 351 (1977)

Nissim, Y.I., Gibbons, J.F., Evans, Jr., C.A., Deline, V.R., Noberg, J.C., Appl. Phys. Lett. **37**, 89 (1980)

Northrup, G.A., Mooney, P.M., J. Elec. Mat. **20**, 13 (1991)

Oh, E.G., Hanna, M.C., Lu, Z.H., Szmyd, D.M., Majerfeld, A., J. Appl. Phys. **74**, 1056 (1993)

Olmsted, B.L., Houde-Walter, S.N., Appl. Phys. Lett. **60**, 368 (1992)

O'Reilly, E.P., Appl. Phys. Lett. **55**, 1409 (1989)

Oshiyama, A., Ohnishi, S., Phys. Rev. B **33**, 4320 (1986)

Panish, M.B., J. Appl. Phys. **44**, 2659 (1973)

Palmetshofer, L., Kastner, J., Lübke, K., Nuc. Inst. Meth. Phys. Res. **B59/60**, 1081 (1991)

Pant, J., Pansewicz, K., Zhang, J., Hayes, T.M., Williamson, D.L., Theis, T.N., Keuch, T.F., Gibart, P., Jpn. J. Appl. Phys. **32** pt 2, 731 (1993)

Pavesi, L., Ky, N.H., Ganière, J.D., Reinhart, F.K., Baba-Ali, N., Harrison, I., Tuck, B., Henini, M.J., Appl. Phys. **71**, 2225 (1992)

Peale, R.E., Mochizuki, Y., Sun, H., Watkins, G.D., Phys. Rev. B **45**, 5933 (1992)

Pearton, S.J., Solid State Phenomena **1-2**, 247 (1988)

Pearton, S.J., Williams, J.S., Short, K.T., Johnson, S.T., Jacobsen, D.C., Poate, J.M., Gibson, J.M., Boerma, D.O., J. Appl. Phys. **65**, 1089 (1989)

Ramsteiner, M., Wagner, J., Ennen, H., Maier, M., Phys. Rev. B **38**, 10669 (1988)

Rehberg-Krause, R., Drost, Th., Polity, A., Roos, G., Pensl, G., Volm, D., Meyer, B.K., Bischopink, G., Benz, K.W., Phys. Rev. B **48**, 11723 (1993)

Roach, W.P., Chandrasekhar, M., Chandrasekhar, H.R., Chambers, F.A., Phys. Rev. B **44** 13404 (1991)

Robinson, J., *Handbook of Spectroscopy Vol III*, CRC Press, p. 417 (1981)

Rösel, F., Fries, H.M., Alder, K., Pauli, H.C., Atomic Data and Nuclear Data Tables **21**, p.91 (1978)

Rowe, J.E., Sette, F., Pearton, S.J., Poate, J.M., Solid State Phenomena **10**, 283 (1989)

Saito, M., Oshiyama, A., Sugino, O., Phys. Rev. B **45**, 13745 (1992)

Saito, M., Oshiyama, A., Sugino, O., Phys. Rev. B **47**, 13205 (1993)

Saito, M., Oshiyama, A., Phys. Rev. B **48**, 11804 (1993)

Sampaio, J.F., Chaves, A.S., Ribiero, G.M., Guimarães, P.S.S., de Carvalho, R.P., de Oliviera, A.G., Phys. Rev. B **44**, 10933 (1991)

Seaward, K.L., Appl. Phys. Lett. **61**, 3002 (1992)

Shibata, H., Mokita, Y., Ikeda, T., Hasegawa, M., Yamada, A., Niki, S., Iida, T., Uekusa, S., Nucl. Inst. Meth. Phys. Res. **B80/81**, 578 (1993)

Shim, T.E., Itoh, T., Yamamoto, Y., Suzuki, S., Appl. Phys. Lett. **48**, 641 (1986)

Shim, T.E., Itoh, T., Yamamoto, Y., J. Appl. Phys. **61**, 4635 (1987)

Shim, T.E., Itoh, T., J. Appl. Phys. **65**, 486 (1989)

Skierbiszewski, C., Suski, T., Wisniewski, P., Jantsch, W., Ostermayer, G., Wilamowski, Z., Walker, P.G., Mason, N.J., Singleton, J., Appl. Phys. Lett. **63**, 3208 (1993)

Steetman, B.G., 1990, in *Solid State Electronic Devices*, (Prentice Hall), pp. 212-215, p.142

Su, Z., Farmer, J.W., Appl. Phys. Lett. **59**, 1746 (1991)

Subramanian, S., Anand, S., Arora, B.M., Solid State Commun. **76**, 609 (1990)

Subramanian, S., Anand, S., Arora, B.M., Lu, Y.C., Bauser, E., Phys. Rev. B **48**, 8757 (1993)

Tan, T.Y., Gösele, U., Yu, S., Critical Reviews in Solid State and Materials Sciences **17**, 47 (1991)

Theis, T.N., Mooney, P.M., Wright, S.L., Phys. Rev. Lett. **60**, 361 (1988)

Theis, T.N., Morgan, T.N., Parker, B.D., Wright, Mater. Sci. Forum **38-41** pt. 3, 1073 (1989)

Thompson, J.H., Ritchie, D.A., Jones, G.A.C., Linfield, E.H., Frost, J.E.F., Churchill, A.C., Smith, G.W., Lee, D., Haulton, M., Whitehouse, C.R., Surface Science **267**, 69 (1992)

Thurmond, C.D., Schwartz, G.P., Kammlott, G.W., Schwartz, B.J., J. Electrochem. Soc. **127**, 1366 (1980)

Tuck, B., Badawi, M.H., J. Phys. D: Appl. Phys. **11**, 2541 (1978)

Vanasupa, L.S., Deal, M.D., Plummer, J.D., J. Electrochem. Soc. **138**, 2134 (1991)

Van Vechten, J.A., Mat. Res. Soc. Symp. Proc. **46**, 83 (1985)

Von Bardeleben, H.J., Buyanova, I., Belyaev, A., Sheinkman, M., Phys. Rev. B **45**, 11667 (1992)

Von Muench, W., Solid State Electronics **9**, 619 (1966)

Wang, Z., Chung, K., Miller, T., Williamson, F., Nathan, M.I., Appl. Phys. Lett. **58**, 2366 (1991)

Wang, Z., Chung, K., Miller, T., Williamson, F., Nathan, M.I., J. Appl. Phys. **71**, 1802 (1992)

Wei, L., Tanigawa, S., Uematsu, M., Maezawa, K., Jpn. J. Appl. Phys. **31**, 2056, (1992)

Williamson, D.L., Gibart, P., J. Phys. C: Solid State Phys. **14**, 2517 (1981)

Williamson, D.L., J. Appl. Phys. **60**, 3466 (1986)

Williamson, D.L., Gibart, P., El Jani, B., N'Guessan, K., J. Appl. Phys. **62**, 1739 (1987)

Williamson, D.L., Gibart, P., Solid State Phenomena **10**, 163 (1989)

Williamson, D.L., Gibart, P., Semicond. Sci. Technol. **6**, B70 (1991)

Williamson, D.L., Neisen, L., Weyer, G., Sielemann, R., Langouche, G., 1992, in: *Hyperfine Interactions of Defects in Semiconductors*, ed. G. Langouche (Elsevier) pp. 1-75

Wolk, J.A., Krugr, M.B., Heyman, J.N., Walukiewicz, W., Jeanloz, R., Haller, E.E., Phys. Rev. Lett. **66**, 774 (1991)

Wuyts, K., Langouche, G., van Rossum, M., Silverans, R.E., Phys. Rev. B **45**, 6297 (1992)

Yamaguchi, E., Jpn. J. Appl. Phys. **25**, L643 (1986)

Yamaguchi, E., Shiraishi, K., Ohno, T.J., Phys. Soc. Jpn. **60**, 3039 (1991)

Yamazaki, H., Kawasaki, Y., Fujimoto, M., Kudo, K., Jpn. J. Appl. Phys. **14**, 717 (1975)

Yu, K.M., Khachaturyan, K., Weber, E.R., Lee, H.P., Calas, E.G., Phys. Rev. B **43**, 2462 (1991)

Zhang, S.B., Phys. Rev. B **44**, 3417 (1991)